Developing Novel Molecular Contrast Agents For Imaging Vulnerable Plaques

Rhiannon Jane Evans

Supervised by Professor N. J. Long

Imperial College London

Department of Chemistry

Thesis submitted in partial fulfilment of the requirements for the degree of Doctor of Philosophy

November 2019

DECLARATION OF ORIGINALITY

I hereby declare that this work was carried out between October 2016 and August 2019 at Imperial College London and King's College London, in the departments of Chemistry, Bioengineering, and Biomedical Engineering. The work has not been previously submitted for a degree at this or any other university, and it is entirely my own except where stated otherwise, through acknowledgement or citation.

COPYRIGHT DECLARATION

ACKNOWLEDGEMENTS

Firstly I would like to thank my primary supervisor, Professor Nick Long, for his support and patience during the trials and tribulations of this project, his expertise and guidance. I would like to extend my thanks also to Professor René Botnar, whose expertise in cardiovascular MR imaging, and the design and execution of preclinical trials was invaluable. Thanks should also go to Professor Rob Krams whose hypothesis and prior research provided the basis for this work. This work would not have been possible without funding from the EPSRC through the King's and Imperial Centre for Doctoral Training in Medical Imaging.

I am immensely grateful for the support of a huge number of academics who were generous enough to share their knowledge, experience, and time with me: Dr Javier Hernández-Gil for his assistance with contrast agent design and synthesis, Dr Zahra Mohri and Dr Kok Yean Chooi for their assistance in quickly getting up to speed with hugely complex biology, designing the *in vivo* experiments, and performing surgeries, Dr Alkystis Phinikaridou and Dr Begoña Lavin-Plaza for their support with preclinical and imaging studies, histology, and data analysis, and Dr Joseph Boyle for his guidance and support in designing and carrying out *in vitro* studies, and for his insights into the complex biology of atherosclerosis.

I would like to thank Dr Mahmoud Ardakani and Dr Ecaterina Ware of the Harvey Flowers suite in the Department of Materials at Imperial College London, and Dr Patricia Carry of the Department of Chemical Engineering for their support with characterisation, and Dr Angela Richard-Loendt and the staff of the UCL-Neuropath facility for sectioning. I would also like to thank Eunice Wong for her support with *in vitro* experiments examining cell viability. I would further like to thank the members of the Long group for their good humour and support, but most particularly Megan Midson for her assistance with TEM measurements, and for her insights into nanoparticle chemistry, and Daohe Yuan.

None of this would have been possible without the unfailing support and patience of my family and friends, so it would be remiss not to thank them. I would like to thank my parents for the interest they have shown in my work, their patience, and the pictures from exotic locales to remind me of the world outside. I would like to thank Jenni Hunt, who is herself becoming acquainted with the joys of PhD life; Bella Grant for hours of incoherent phone calls, listening to me alternately sob, giggle and rant; Sini Aalto, for her sympathy towards the unpredictability of science; Cassandra Smith - for everything, words could never do justice to your contribution; Jae Fraser for her unshakeable faith, and the supply of cat pictures; Rob Robinson, for an invaluable outside perspective on my research and the PhD experience, and for his taste in gin; Kathryn George for her wisdom, patience, and endless supply of puns; and Dr Brittany Sutherland for being the voice of reason. I would also like to thank everyone at Swing Patrol Clapham Junction for providing an escape when the science got too much, particularly Hayley Watson, Adrian Cecil, and Emer Fahy. There's nothing like dancing to get you out of your own head. I really couldn't have done this without you. Thank you.

ABSTRACT

This thesis describes the design, synthesis, and testing of novel MRI contrast agents based on iron oxide nanoparticles for the specific detection and identification of vulnerable plaque. Cardiovascular disease remains the leading cause of death worldwide, primarily due to heart attacks and strokes resulting from vulnerable plaque rupture. Vulnerable plaque occurs in atherosclerosis, when plaque is deposited in the walls of blood vessels and can take on vulnerable or stable phenotypes. There is an urgent need for an imaging biomarker to enable the specific detection of vulnerable plaque to facilitate treatment and prevent future heart attacks and strokes. MRI is a non-ionising, non-invasive imaging modality with the potential for highly customisable contrast agents.

Chapter 2 discusses the design and synthesis of a library of superparamagnetic iron oxide nanoparticle-based contrast agents through thermal decomposition and coating with different surface ligands, including poly (maleic anhydride-alt-1-octadecene), alendronate, and poly (ethyleneimine). The agents were characterised through transmission electron microscopy, dynamic light scattering, zeta potential and relaxivity measurements.

Chapter 3 presents the results of biological tests performed using the lead candidate from the synthesis carried out in chapter 2, including the coupling of a targeting antibody to the contrast agent, *in vitro* testing, and MR imaging in a preclinical model with histological verification of the results.

Chapter 4 builds on the initial design and synthetic work of Chapter 2 with the introduction of a gold shell, moving towards multi-modality imaging. Several synthetic routes for the introduction of the gold shell and a selection of surface ligands including poly (maleic anhydride-alt-1-octadecene), homocysteine, and citrate were studied, and characterised through transmission electron microscopy, dynamic light scattering, and zeta potential measurements.

Chapter 5 summarises the conclusions of the project, presents potential areas for future work and concludes the thesis.

Contents

Table of Figures

Table of Tables

LIST OF ABBREVIATIONS

˚C	Degrees Celsius
µl	Microlitres
2D/3D	Two-dimensional/three-dimensional
Ab	Antibody
Ag	Antigen
ApoE	Apo lipoprotein E
ApoE-/-	ApoE dual knockout transgenic mouse model
B/ B_0	External magnetic field
BCA	bicinchoninic acid
BCA	Brachiocephalic artery
BSA	Bovine serum albumin
CCL5/RANTES	Chemokine (CC) ligand 5/Regulated on Activation, Normal T cell Expressed and Secreted
CCR1/2/5	Chemokine receptor type 1/2/5
CCR2/MCP-1	Chemokine (CC) ligand 2/Monocyte chemoattractant protein 1
CD14/16/68	Cluster of Differentiation 14/16/68
CT	Computed Tomography
CVD	Cardiovascular disease
CX3CL1/R1	Chemokine (CX3C) ligand/receptor 1 (Fractalkine)
DCC	N,N'-dicyclohexylcarbodiimide
DE	Delayed enhancement
DLS	Dynamic Light Scattering
DNA	Deoxyribonucleic acid
ECM	Extra-cellular matrix
EDC	1-Ethyl-3-(3-dimethylaminopropyl)carbodiimide
EPR	Enhanced permeability and retention effect
EtOH	Ethanol
Fc	Crystallisable fragment
FDA	Food and Drug Administration
FDG	[^{18}F]fluorodeoxyglucose
FOV	Field of view
Gd-DTPA	Gadolinium diethylenetriamine penta-acetic acid
$\hbar$	Planck's constant over 2π

hCRP	High-sensitivity C reactive protein
HFD	High fat diet
HRP	Horseradish peroxidase
ICP	Inductively-coupled plasma
IFN-γ	Interferon- γ
Ig	Immunoglobulin
IL-4	Interleukin 4
kDa	KiloDaltons
keV	Kilo electron volts
LCA	Left carotid artery
LDL/oxLDL	Low-density lipoprotein/oxidised low-density lipoprotein
LDLR	LDL receptor
LDLR-/-	LDL dual knockout
LPS	Lipopolysaccharide
Ly6	Lymophocyte antigen 6 complex
m	Metres
M1	“classically activated” macrophage
M2	“non-classically activated” macrophage
M_{Ha}	Haemorrhage-associated macrophages
M_{hem}	Macrophage phenotype differentiated by exposure to haem
MHz	Megahertz
MIP-1α/β	Macrophage inflammatory protein 1α/β
ml	Millilitres
mm	Millimetres
mM	Millimolar
mmol	Millimolar
MMP	Matrix metalloproteinase
M_{ox}	Macrophage phenotype associated with oxidative stress
MR	Magnetic Resonance
MRI	Magnetic Resonance Imaging
m_s	Spin number
ms	Milliseconds
mT	milliTesla
mW	Molecular weight

NHS	N-hydroxysuccinimide
NIR	Near Infra-red
nm	Nanometres
NMR	Nuclear magnetic resonance
OCT	Optical Coherence Tomography
PBS	Phosphate buffered saline
PEG	Poly ethyleneglycol
PEI	Poly ethyleneimine
PET	Positron Emission Tomography
PMAO	Poly (maleic anhydride-alt-1-octadecene)
r1/r2	T_1/T_2 relaxivity
RCA	Right carotid artery
RES	Reticuloendothelial system
RF	Radiofrequency
scFv	Single-chain variable fragment
SPECT	Single Photon Emission Computed Tomography
SPION	Superparamagnetic Iron Oxide Nanoparticle
T_1	Longitudinal relaxation time
$T_{2/}$ T_2*	Transverse relaxation time
TCFA	Thin-cap fibroatheroma
TEM	Transmission Electron Microscopy
THF	Tetrahydrofuran
THP-1	Human monocyte line derived from a leukemic patient
TLR	Toll-like receptor
TNF-α	Tumour necrosis factor α
UV-Vis	Ultraviolet-Visible light spectroscopy
VCAM-1	Vascular adhesion molecule 1
VEGF	Vascular endothelial growth factor
WHHL	Watanabe Heritable Hyperlipidemic
WHO	World Health Organisation
XTT	Tetrazolium salt used for cell viability assays
γ	Gyromagnetic ratio
ΔE	Difference between energy levels

Chapter 1

Introduction

This project features interdisciplinary research examining MRI (Magnetic Resonance Imaging) contrast agents and recent developments in iron oxide nanoparticle chemistry, and applying this to the area of atherosclerosis research. Atherosclerosis is the underlying cause of heart attacks and strokes, and is associated with high cardiovascular disease related mortality. Heart disease remains the leading cause of death worldwide according to World Health Organisation statistics, and although mortality rates are declining, it also represents a huge burden on healthcare systems due to high care costs associated with stroke and myocardial infarction survivors, and costs resulting from decreased productivity.

This thesis will first outline the background of the medical imaging field, discuss MRI in more detail, and then introduce the complex biology of atherosclerosis and the justification for biomarker selection in this project. It will then introduce the research questions and aims of the project. It will then go on to discuss the design and synthesis of probes, and the biological assessment of these probes both *in vitro* and *in vivo*. This will be followed by the second phase of contrast agent development, building on the results from phase one and moving towards multi-modal imaging. The thesis will end with a concluding section summing up the overall work and findings, and presenting potential avenues for future work.

1.1 MEDICAL IMAGING

Medical imaging is the imaging of the body for diagnostic and treatment purposes, which can be anatomical or physiological in nature, i.e. visualising structure or visualising processes.

Molecular imaging is a subset of medical imaging which is generally defined as the visualisation, characterisation and measurement of biological processes at the molecular and cellular level in humans and other living systems. Not all physiological imaging is classified as molecular imaging. For example, imaging myocardial function through measurement of ejection fraction is imaging blood flow rather than a molecular or cellular process.

This chapter will begin with an overview of medical imaging modalities, before focussing on MRI, and then discussing the biology of atherosclerosis.

1.1.1 OVERVIEW OF MEDICAL IMAGING MODALITIES

Medical imaging modalities cross a wide range of technologies and applications. Some are dependent on radiation, some are structural, some are physiological, some are expensive, and some are cheap and portable. All require some level of training to use.

1.1.1.1 X-RAY AND COMPUTED TOMOGRAPHY (CT)

X-ray is the original medical imaging modality discovered at the end of the 19th century by Wilhelm Roentgen. Named ‘X-radiation’ for ‘unknown radiation’, Roentgen discovered that Crookes tubes emitted radiation which passed through cardboard and generated a fluorescence in a nearby screen. Crookes tubes were early electrical discharge tubes used for generating cathode rays. X-rays fall on the electromagnetic spectrum between ultraviolet and gamma radiation, with a wavelength range from 0.01-10 nm[1].

X-rays are generated by the collision of high energy electrons emitted by a cathode with a target anode which is usually made of tungsten because of its high melting point. In the case of mammography where lower energy X-rays are required, the anode is usually molybdenum. Generators are shielded with lead. In all cases X-ray images are generated by the different attenuation of the radiation by varying tissue types: bone as the densest has the highest attenuation coefficient, resulting in excellent skeletal images but poorer contrast in soft tissue[1]. An example of an X-ray image can be seen in figure 1.1.

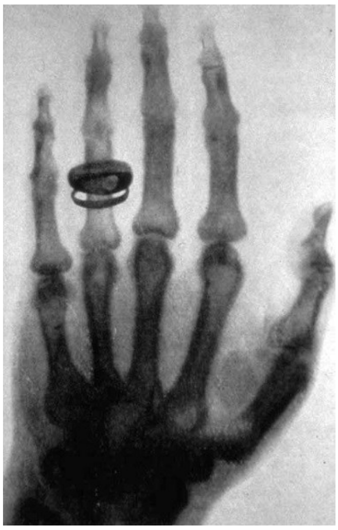

FIGURE 1.1: ONE OF THE FIRST X-RAY IMAGES OF ROENTGEN’S WIFE’S HAND ALSO SHOWING HER WEDDING RING (PUBLIC DOMAIN)

Computed tomography (CT) allows the application of traditionally 2D X-ray technology to 3D imaging, and is widely used in clinical settings worldwide[2]. CT is a more useful first-line scan particularly in emergency situations where patients may not be able to answer questions regarding implants which mean an MRI scan would be dangerous or potentially fatal. This is because CT does not have any intrinsic risk to patients with pacemakers, other medical devices, or histories which might involve reconstructive surgery or metal fragments still embedded in the body.

CT scans are used in all areas of the body, including identifying bleeds or tumours in the brain, diagnosing and monitoring lung cancers, angiography and cardiac scans. Some contrast agents are used in CT, particularly for angiography and gastrointestinal imaging[3]. Iodinated contrast is used for imaging vasculature, and the gastrointestinal tract is usually imaged with a barium meal[3]. Sometimes air is used in conjunction with barium to improve contrast in a gastrointestinal scan because it is less radio-opaque than surrounding tissue and can highlight the interior of the colon in a double-contrast scan. In order to enhance contrast in X-ray or CT images, contrast agents must be heavy atoms which is why these particular techniques have evolved. In terms of multi-modality imaging or alternatives, gold also shows up very well on CT and can be used in conjunction with iron oxide nanoparticles for imaging both with CT and MR. Radioactive iodine tracers can be used in both PET and CT[1]. An excellent discussion of CT and CT contrast agents can be found by Lusic and Grinstaff[3].

Although X-ray, and to a lesser extent CT, are workhorses of medical imaging, both modalities rely on the use of ionising radiation, and this limits their applicability in the clinic particularly for longitudinal studies. Where serial imaging is likely to be necessary, CT might be a great primary modality but the follow-up can be risky. Radiation dose is even higher with PET-CT scans.

1.1.1.2 POSITRON EMISSION TOMOGRAPHY AND SINGLE-PHOTON EMISSION COMPUTED TOMOGRAPHY (PET AND SPECT)

PET and SPECT are commonly discussed under the umbrella of nuclear medicine. Although some PET and SPECT tracers may have some therapeutic effect, and can be used for targeted radiotherapy, on the whole these techniques are primarily focused on imaging physiological processes *in vivo*.

Both PET and SPECT are based on the microdosing of tracers containing or labelled with radioactive isotopes. In the case of SPECT, tracers emit gamma radiation which can have a wide range of photon energies. In the case of PET however, isotopes emit positrons. The positrons only travel short distances before encountering electrons and annihilating, emitting two antiparallel gamma photons at 511 keV[1]. Figure 1.2 illustrates a nuclear imaging scan, more specifically a PET scan, demonstrating the lack of structural detail.

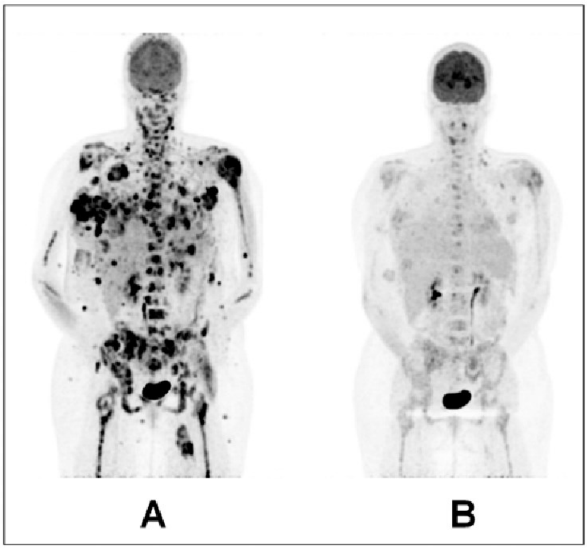

FIGURE 1.2: FIGURE ILLUSTRATING AN FDG PET SCAN TAKEN FROM CELL HIERARCHY, METABOLIC FLEXIBILITY AND SYSTEMS APPROACHES TO CANCER TREATMENT BY P. HIRST AND M. BERRIDGE[4], USED WITH PERMISSION FROM BENTHAM SCIENCE.

Gamma radiation passes through tissues without being absorbed or attenuated, and the gamma photons are detected on the outside of the body with a gamma camera. In the case of SPECT, single photons are emitted, but because with PET two colinear photons are generated it is possible for the detector to calculate the origin of the photons arriving at the same time and so better localise the source of the emission. This means that current PET tracers have a better resolution than SPECT, however it is possible to administer multiple SPECT tracers simultaneously because the different gamma energies mean it is possible to differentiate between different tracers. However, there is no way to differentiate PET tracers since all photons are emitted at 511 keV so it is not possible to combine tracers in a PET scan.

PET scanners have a circle of detectors in order to accurately back-project along photon trajectories in order to locate the decay in space, whereas SPECT scanners have a single gamma camera which rotates around the patient, due to the lack of requirement to record simultaneous decays.

Although PET resolution is better, it is still poor, and the advantages of nuclear medicine lie in the sensitivity of the imaging rather than the resolution[5]. It is also more commonly used for physiological imaging of processes such as metabolism. Nuclear imaging also gives fantastic depth penetration which is an advantage over other methods such as ultrasound or optical imaging, both of which can be restricted[5].

Most SPECT tracers in the clinic are based on technetium-99m which has a half-life of six hours, making it easy to manipulate without resulting in an unnecessarily high radiation dose to patients. It is also a generator produced isotope, which is advantageous for access and is why technetium-99m agents remain common in the clinic although PET agents which are superior may be available. As technetium-99m chemistry has been ubiquitous for decades, many kits are available which allow tracers to be synthesised easily and consistently to a clinical standard without requiring access to facilities much more complex than a technetium-99m generator.

PET tracers, on the other hand, usually rely on isotopes generated by a cyclotron, this is one reason why they have not caught on as widely, because a cyclotron is a significant barrier to access. The most common PET tracer used in the clinic is [^{18}F]fluorodeoxyglucose (FDG) modified with fluorine-18. This is used to image metabolism which is particularly applicable in cancer. The image in figure 1.2 is an FDG PET scan. Tumour cells often have a high metabolic rate, and this results in them taking up the glucose mimic rapidly. However, the modification of a fluorine means that although the tracer can undergo the beginning of metabolism, it cannot be processed entirely and becomes trapped in the cell. Fluorine-18 has a comparatively long half-life of around two hours, and this means that it is relatively accessible to hospitals even without a cyclotron as it can be transported, delivered, and used before it decays[1,6]. This is a significant advantage in comparison to other PET isotopes such as carbon-11 which has a half-life of twenty minutes and can require complex chemistry for incorporation into a tracer.

Gallium-68 is a generator-produced PET isotope which is of increasing interest to researchers and clinicians. Although no gallium-68 radiopharmaceuticals are yet in use in the clinic, the one hour half-life, potential for kit chemistry, and easily accessible production method make gallium-68 very appealing for nuclear imaging. It also could link to the development of radiotherapeutics based on gallium-67, a SPECT isotope with a much longer half-life which is a strong Auger electron emitter, making it very promising for radiotherapy targeted at a cellular level.

An excellent review of nuclear medicine discussing the range of available isotopes and their applications, encompassing both imaging modalities and molecular radiotherapy is entitled “A nuclear chocolate box: the periodic table of nuclear medicine” by Blower[6].

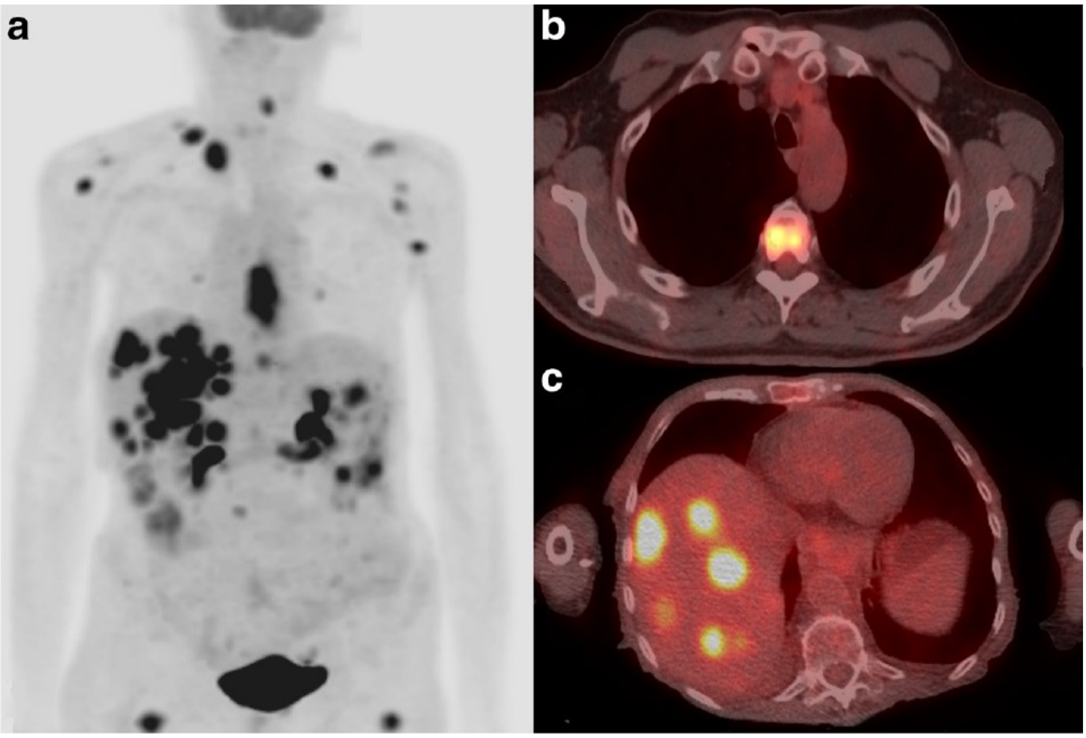

FIGURE 1.3: FIGURE SHOWING EXAMPLES OF METASTATIC CANCER LESIONS DETECTED BY PET-CT FROM WORK BY GOENSE ET. AL.[7] (COURTESY: EUR. J. NUCL. MED. MOL. IMAGING 45 1742/CC BY 4.0)

PET-CT scanners are used in clinical settings, and more recently PET-MR scanners have arrived on the market in an attempt to reduce the high radiation dose associated with a PET-CT scan. These scanners attempt to combine state-of-the-art imaging techniques in order to overcome their respective disadvantages: PET has poor resolution but excellent sensitivity, whereas both CT and MRI have excellent resolution. An example of the utility of a PET-CT scan is illustrated in figure 1.3. CT contrast agents exist but are very limited, and although there is a wide range of MRI contrast agents, MR is not a very sensitive technique. By combining excellent anatomical scans with the physiological information generated by PET, the hope is that diagnostics can be improved. This could also have ramifications for surgery, particularly cancer surgeries, to ensure that tumours can be removed with minimal damage to surrounding tissue.

Both PET and SPECT are very useful techniques, however they do involve a dose of ionising radiation to the patient and can be very expensive.

1.1.1.3 MAGNETIC RESONANCE IMAGING (MRI)

Magnetic Resonance Imaging (MRI) is a non-ionising, non-invasive imaging modality which uses the high levels of water in the body to generate contrast in images without the administration of an exogenous contrast agent. MRI has good resolution but low sensitivity and contrast agents are often used to enhance the images particularly for diagnostic purposes. As this imaging modality is the focus of this project, MRI is discussed in greater detail in section 1.2 of the introduction.

1.1.1.4 ULTRASOUND

Ultrasound has many advantages over other medical imaging modalities because it is cheap, portable, and robust. It is also non-invasive and non-ionising, and regarded as being safe. Ultrasound uses sound waves with frequencies in the range of 1-12 MHz, outside the range of human hearing, to generate real-time images by the reflection of soundwaves at tissue boundaries where there is a change in acoustic impedance[1]. It also has some therapeutic applications and can be used in drug delivery.

Ultrasound is most commonly encountered as a way of monitoring foetal development during pregnancy, however it has many other applications in medical imaging including echocardiography, angiology, musculoskeletal scanning as an alternative to X-ray for fracture detection, and the scanning of most major organs in the body. Despite this wide range of applications, ultrasound has limited depth penetration and poor resolution, it can be difficult to image structures protected by bone and has a limited field-of-view[1,5].

The real-time nature of ultrasound imaging leads to several techniques which cannot be easily replicated by other imaging modalities, including the ability to measure blood flow by creating Doppler maps which show the velocity of blood at a particular arbitrary point. This is particularly useful for echocardiograms to diagnose cardiomyopathies or issues with heart valves. Ultrasound does also have some application in cardiovascular imaging through the use of an intravascular catheter, and can be used to detect vulnerable plaque[8].

Although ultrasound is a very useful imaging modality without the introduction of external contrast, it is possible to enhance contrast in ultrasound via the use of microbubbles as seen in figure 1.4. These are bubbles of inert gas which are less than 1 mm in diameter and which remain inside the blood vessels rather than extravasating into interstitial fluid. When hit by ultrasound pulses the bubbles oscillate and enhance contrast by reflecting the sound waves more effectively than surrounding tissue[9,10]. The oscillation of the bubbles can also play a role in drug delivery, for example to the brain, where bubble oscillation can open the blood-brain barrier in a controlled fashion to allow targeted delivery to a certain area[11]. The bubbles can also deliver drug cargos in a more traditional and targeted manner by encapsulating the drug in the lipid or protein solid shell of the bubble and then focusing an ultrasound beam to allow the bursting of the bubble in a specific region[12]. This could be particularly useful for cytotoxic drugs such as those used in chemotherapy. Although bursting the bubbles artificially may raise safety concerns, on the whole microbubbles are a perfectly safe contrast agent for use in the clinic.

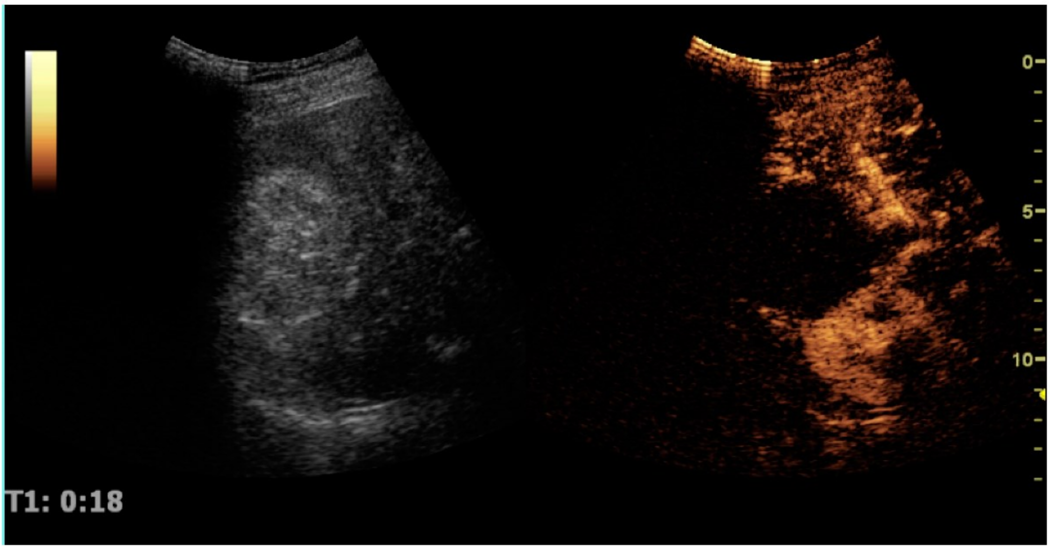

FIGURE 1.4: FIGURE SHOWING CONTRAST ENHANCEMENT OF A KIDNEY ULTRASOUND WITH MICROBUBBLES, TAKEN FROM HANSEN ET. AL.[13] (CC-BY 4.0)

1.1.1.5 Optical Coherence Tomography (OCT)

Optical Coherence Tomography is the current clinical gold standard for imaging atherosclerosis. It is occasionally described as optical ultrasound. Depth penetration is limited with OCT in a similar way to US, so for use in the coronary arteries or vasculature it is a semi-invasive technique involving the insertion of a fibre-optic catheter (figure 1.5). OCT resolution far surpasses intravascular ultrasound[14], and X-ray and MR angiography, it visualises vessel wall morphology and tissue microstructure particularly in plaque regions ten times better than other techniques. In some cases, OCT has been shown to have sub-micrometre resolution[15].

OCT uses coherent light to look beneath the surface of biological tissue, using the reflection of that light from within the tissue to build up images. Interferometry is used to remove scattered photons and background signal, and the high-resolution nature of OCT is due to the use of frequencies associated with light as opposed to sound or the radiofrequency pulses encountered in MRI[16]. Although it is slightly lower frequency than visible light, OCT is often used in conjunction with NIR light because of the enhanced tissue penetration associated with NIR frequencies.

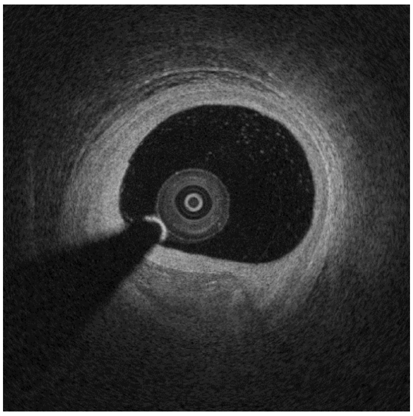

FIGURE 1.5: AN EXAMPLE OF INTRACORONARY OPTICAL COHERENCE TOMOGRAPHY (BY OCTRND , CC BY-SA 4.0)

It is possible to use contrast agents in conjunction with OCT, and these are often based on gold nanoparticles or nanorods which enhance the reflection of light back to the detector[17,18]. Much work has also been done using traditional fluorophores and dyes in conjunction with OCT.

1.1.1.6 MULTI-MODALITY IMAGING

Multi-modality imaging is the idea of combining several imaging modalities in order to maximise the information which can be generated. The best example of this is the use of PET-CT and PET-MR which were both discussed earlier, however it is possible not only to combine imaging modalities but to synthesise tracers which function across several platforms such as nanoparticles labelled with a fluorescent dye and a radionuclide. Naturally, multi-modality imaging is not without its issues, most notably problems with the co-registration of images from different modalities to ensure an accurate picture of the disease state. An excellent discussion of the advantages and disadvantages of multi-modal molecular imaging can be found in the review by Jennings and Long[19].

1.1.2 NANOPARTICLES IN IMAGING

The applications of nanotechnology in both imaging and treatment are unrivalled by more traditional approaches. Far from a narrow definition, the term nanoparticle encompasses multiple materials and morphologies across the inorganic spectrum, with dimensions falling between 10^{-7}-10^{-9} m. The uses of nanoplatforms in imaging runs the gamut from nuclear imaging through magnetic resonance imaging to ultrasound, meaning they have applications in imaging physiological processes and anatomical structures, as well as the potential to act as theranostics (compounds with both diagnostic and therapeutic potential), in combination with drugs already in use, and even on their own. Xie et. al. have produced a comprehensive review of theranostic nanoparticle technologies which is an excellent introduction to the area[20], and a recent review by Ali et. al. offers a comprehensive discussion of the value of targeted drug delivery systems, comparing different delivery vectors[21].

Superparamagnetic iron oxide nanoparticles (SPIONs) are widely used MRI contrast agents, with some potential theranostic applications. As they are the focus of this work, they are discussed in greater detail later in this introduction.

Liposomes and micelles are similar supramolecular assemblies, though they differ in certain fundamental aspects which are shown in figure 1.6. Liposomes have a lipid bilayer separating an aqueous internal core from the external aqueous phase. They have a long-standing application in drug delivery, most notably Doxil, the first nano-drug to receive FDA approval, a liposomal preparation of the anti-cancer drug Doxorubicin which demonstrates reduced side-effects and off-target toxicity. Micelles have a lipid monolayer, and thus usually have a hydrophobic core and a polar surface, though reverse-micelles can also be synthesised which demonstrate the alternative properties. Reverse-micelles have limited *in vivo* applications due to the body's aqueous nature, however the hydrophobic nature of the micelle vesicle allows for the solubilisation of more lipophilic drugs or imaging probes which might otherwise be difficult to administer or target. It is also possible to radiolabel micelles and liposomes, either directly or by labelling the contents of the nanoparticle. There are some examples in the literature of gadolinium chelates being encapsulated in order to perform MRI imaging with lipid nanoparticles[22,23].

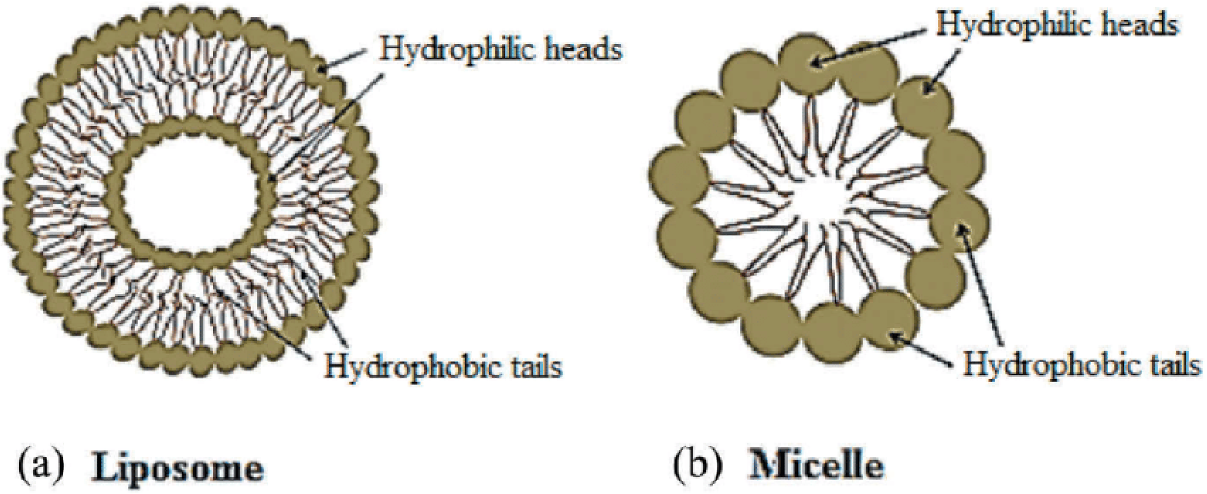

FIGURE 1.6: FIGURE ILLUSTRATING THE STRUCTURAL DIFFERENCES BETWEEN LIPOSOMES AND MICELLES, TAKEN FROM ALI ET. AL.[21] AND USED UNDER CC BY 4.0.

One notable advantage of liposomes and micelles is the flexibility of the cargo they are loaded with, which can be for imaging or therapeutic purposes. Labelling liposomes with radionuclides for PET or SPECT imaging can be very effective for tracking liposomes and micelles *in vivo*, and also for labelling the cargo to track drug delivery. There are multiple labelling strategies for liposomes varying from interior trapping to exterior modification, and even labelling of the drug molecule or other contents of the liposome directly. A comprehensive review of these strategies in radiolabelling specifically can be found by Dearling and Packard[24].

Quantum dots are semiconductor particles which are amongst the smallest nanoparticles. Their size and composition affect their optical properties, which differ from both bulk semiconductor and single atoms. The unique electronic properties of quantum dots mean they are occasionally referred to as “artificial atoms”, due to their bound, discrete electronic states as a single object. The size of quantum dot effectively results in the physical confinement of electrons or electron holes which gives them unique optical properties. Exposure to light or electricity results in quantum dots emitting light of a very specific tunable wavelength, with smaller quantum dots emitting at shorter wavelengths, and larger ones at longer wavelengths. Emission wavelength can also vary as a function of shape. Quantum dots are generally brighter than traditional organic or protein-based probes, with narrow emission spectra and improved photo- and chemical stability. Figure 1.7 demonstrates the wide range of colours it is possible to generate with quantum dots.

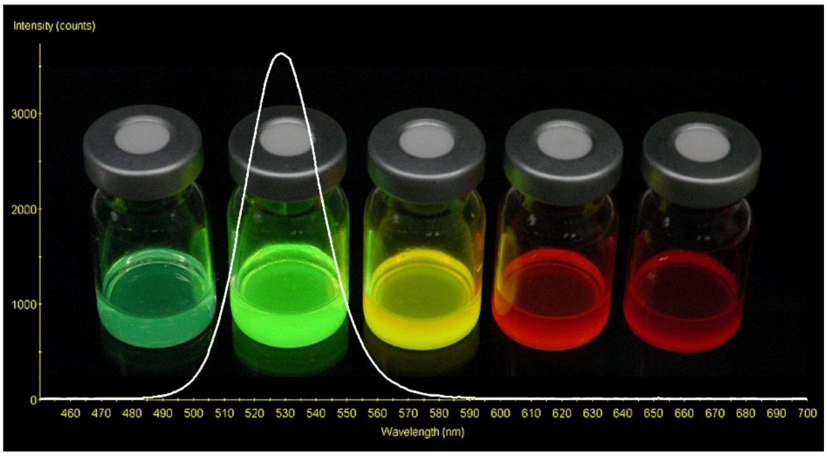

FIGURE 1.7: EXAMPLE OF QUANTUM DOTS SHOWING DIFFERENT EMISSION WAVELENGTHS AND NARROW EMISSION PEAK (PUBLIC DOMAIN, PRODUCED BY NASA)

The application of quantum dots to *in vivo* imaging has historically been limited by several factors, one of which is the difficulty of optical imaging in human tissue, the second of which is the composition of quantum dots which have traditionally been based on toxic metals such as cadmium and lead. Some interesting *in vivo* studies have been carried out where quantum dots have been encapsulated alongside drug molecules in phospholipids, where fluorescence acts as a measure of drug delivery through a quenching interaction between the delivery system and the quantum dots.

In addition to delivery vectors for traditional drugs such as methotrexate or doxorubicin, quantum dots have therapeutic applications in their own right through photodynamics, either directly sensitising tissue or as carriers for photosensitising agents[25]. Discussions of both photodynamic therapy and drug delivery applications can be found in the review by Xie et. al.[20].

Another material which has been widely studied for imaging and therapeutic nanoparticles is gold. Gold nanoparticles can be used as contrast agents in computed tomography[26], optical coherence tomography[17], photoacoustic imaging, and surface-enhanced Raman spectroscopy[27,28]. SPIONs with a gold shell have also been demonstrated as dual-modal T_1/T_2 imaging probes[29]. Much like iron, the synthesis of gold nanoparticles has been well-studied, and close control of both size and morphology is now possible. The effect of morphology on the behaviour of gold nanoparticles is more pronounced than in SPIONs, where the shape of gold changes the surface plasmonic absorption, making it possible to shift absorption into the near-IR region where there is a biological window[30]. Rather than the range of surface ligands seen with SPIONs, the majority of surface ligands used with gold nanoparticles are thiol-containing due to the strong affinity of the thiol groups to bind to the gold surface. Most of these ligands present carboxylic acid or amine groups on the surface for further functionalisation, though it is also possible to thiolate biomolecules such as short peptide or DNA sequences for the stabilisation of gold nanoparticles[12]. This is also a strategy for loading gold nanoparticles with drug molecules, resulting in a concentration effect which can enhance therapeutic behaviour and reduce off-target effects.

The surface plasmon resonance of gold nanoparticles can also be exploited in photothermal therapy, analogous to hyperthermia strategies with SPIONs, though rather than radiowaves, the excitation is through near-IR light[25]. Gold nanoparticles are also stable and biocompatible.

The third major inorganic player alongside iron and gold for nanoparticle synthesis is silica. Silica is well-known to be biocompatible with a history of use in surgical implants, and it is also possible to control the size and morphology of silica nanoparticles[31]. Of course, they lack any intrinsic imaging potential, but silica nanoparticles are easily loaded with cargos such as gadolinium-chelates[32], drug molecules[33,34], and organic dyes[31]. Silica nanoparticles have been the scaffold for multi-modal imaging, encapsulating both quantum dots and SPIONs for optical and magnetic resonance contrast[35–38].

Silica nanoparticles can be made in mesoporous rather than solid forms, pore size can be accurately controlled and result in nanoparticles with massive surface areas and huge interest for drug delivery strategies[39], particularly given the strategies to cap pores in silica nanoparticles to prevent premature drug delivery[40]. Capping can be through organic ligands, or even through other nanoparticles such as gold nanoparticles which introduce imaging capability and also controlled release through irradiation with light or exposure to enzymes[41].

1.2 MRI

1.2.1 MRI PHYSICS

The basis of MRI is the water content of the human body, more specifically the protons of the water molecules. MRI uses the same technique as nuclear magnetic resonance (NMR) spectroscopy, but rather than molecular structure, MRI gives information on the spatial distribution and intensity of proton signals in the body. In contrast to most other imaging modalities, MRI does not use ionising radiation, but rather uses the application of strong magnetic fields and radiofrequency gradients to affect the Larmor frequencies of protons in different positions in 3D space[1].

All nuclei have an intrinsic property called “spin". Spin can be positive or negative, and is always in multiples of ½. Protons, neutrons, and electrons all possess spin, however not all nuclei have an observable spin. In the case of a proton ^1H, the total electronic spin = ½ because the electron is unpaired, and the total nuclear spin also = ½ because the proton in the nucleus is unpaired. This contrasts to ^2H where the total electronic spin remains ½ but the total nuclear spin = 1 due to the presence of the unpaired neutron and unpaired proton in the nucleus.

A nucleus with a net spin will behave like a small magnet when exposed to a static external magnetic field. The spins align with that external magnetic field (B), and precess around that field at the Larmor frequency, which is defined by field strength and by the gyromagnetic ratio which is an intrinsic property of a given nucleus. For hydrogen, the gyromagnetic ratio, γ = 42.6 MHz/Tesla. Although NMR spectrometers can be much stronger, clinical MRI scanners usually use static magnetic fields B_0 of 1.5 or 3 Tesla. See figure 1.8.

When the spins align with the external field, they begin to precess and align either with or against the field, i.e. in a low or high energy state. At room temperature the number of particles in the lower energy state slightly outnumbers those in the higher energy state according to the Boltzmann distribution. Particles can undergo a transition between the low and high energy states by the absorption of a photon, the energy of which corresponds exactly to the energy gap. Given that Planck’s constant allows the relation of photon energy to frequency, this energy gap is referred to in MRI and NMR as the Larmor or resonance frequency.

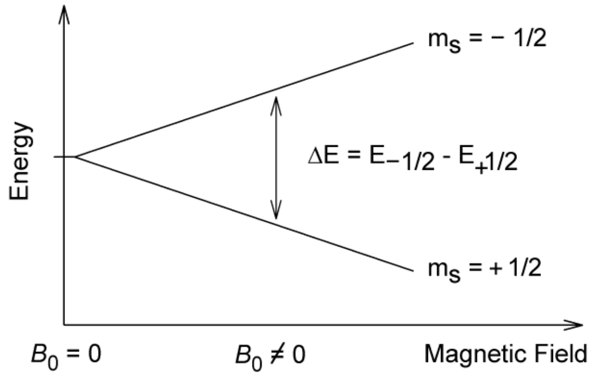

FIGURE 1.8: AN ILLUSTRATION OF THE ENERGY SPLITTING OF SPINS IN AN EXTERNAL MAGNETIC FIELD (PUBLIC DOMAIN, TAKEN FROM WIKIMEDIA COMMONS, BY JBANCROFTBROWN). HERE $\Delta E = \gamma\hbar B_0$ WHERE γ IS THE GYROMAGNETIC RATIO OF THE NUCLEUS AND B_0 IS THE EXTERNAL MAGNETIC FIELD.

After aligning with the external field B_0, the protons are exposed to a time-varying magnetic field B_1 in the form of an RF pulse, applied perpendicular to B_0 at a frequency close to the Larmor frequency. This tilts protons away from their alignment to the external field B_0, and causes the protons to tilt or flip in the xy-plane while still precessing around the z-axis of the original field B_0. The signal in MRI is generated by the relaxation of these protons back to equilibrium.

At equilibrium, the net magnetisation vector is aligned with the external static magnetic field B_0, which can be thought of as the z-axis. Longitudinal magnetisation refers to magnetisation along the z axis, or the axis around which the protons are precessing. When the spins are knocked out of their precessional plane, i.e. by an RF pulse, the time taken to return to equilibrium along the z-axis is the spin-lattice relaxation time, or T_1, which is an important measure in MRI and in contrast agent design for MRI (figure 1.9).

In addition to returning to equilibrium along the z-axis, the net magnetisation vector dephases in the xy-plane. This occurs before the return of equilibrium along the z-axis. The time taken for the transverse magnetisation to return to equilibrium is the spin-spin relaxation time, denoted by T_2 (figure 1.9). Unlike T_1, T_2 has two components: molecular interactions which result in a pure T_2 effect, and inhomogeneities in the local magnetic field B_0 which also shorten transverse relaxation time. It is difficult to separate these two components, and so they are often combined and represented as T_2^*, or the combined time constant of both molecular and field variation effects. T_2 is always shorter than T_1.

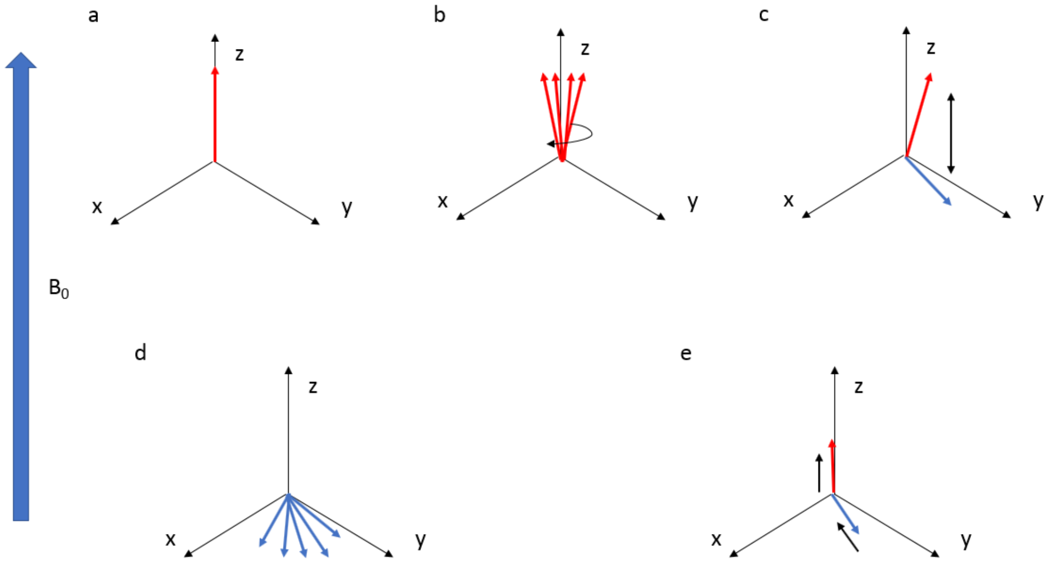

FIGURE 1.9: ILLUSTRATION OF THE PROCESS OF SPIN FLIPPING AND RECOVERY IN MRI PHYSICS: A) NET MAGNETISATION VECTOR IS ALIGNED WITH Z-AXIS B) NET MAGNETISATION VECTOR PRECESSES AROUND Z-AXIS AT LARMOR FREQUENCY C) APPLICATION OF PULSE B1 FLIPS THE MAGNETISATION VECTOR INTO THE XY PLANE D) NET MAGNETISATION DEPHASES IN THE XY PLANE, THIS IS THE SPIN-SPIN RELAXATION TIME OR T2 E) FINALLY MAGNETISATION RECOVERS ALONG THE Z-AXIS, THIS IS SPIN-LATTICE RELAXATION, OR T1

1.2.2 SPATIAL ENCODING

Although the physics underlying NMR and MRI are identical, the fundamental difference is that NMR is only looking at structural information on a molecular level, whereas MRI is trying to measure the intensity and spatial distribution of the proton signals. This is achieved via spatial encoding done by the application of RF gradients in the x, y, and z directions. The application of these gradients changes the Larmor frequency of protons by varying the magnetic field strength they are exposed to, thus it is possible to only excite protons in specific regions or 'slices' by applying the external RF pulse which only corresponds to that particular energy gap or photon energy, exciting a specific region in space. The different frequencies allow the generation of a 3D image via Fourier transform of the frequency data.

1.2.3 MRI CONTRAST AGENTS

MRI contrast agents fall into two categories: those that enhance T_1 and those that enhance T_2. T_1 contrast agents result in positive contrast, or a brightening of the image, whereas T_2 contrast agents result in negative contrast, or a darkening of the image. This goes some way towards explaining their relative popularity in clinical applications, where loss of signal can be challenging to identify, particularly in abdominal scans, whereas the brightening of T_1 agents is much simpler to detect.

1.2.3.1 T_1 CONTRAST AGENTS

T_1 contrast agents are most commonly based around gadolinium(III) which is a lanthanide element with seven unpaired electrons making it hugely paramagnetic. There are many commercially available gadolinium-based contrast agents used in the clinic such as Dotarem, Omniscan, MultiHance, Magnevist and others. The majority of gadolinium-based contrast agents by far are small molecule agents which consist of the gadolinium centre and a chelating ligand, though some work has looked into gadolinium-containing micelles. Although gadolinium-based contrast agents are widely used, there are toxicity concerns particularly in patients with kidney disease[42]. Gadolinium can leach out of the chelating ligands and cause a condition known as nephrogenic system fibrosis[43], and recent studies have identified gadolinium deposits in the brains of patients scanned with gadolinium-based contrast agents[44].

Some interesting work has been published by Pan et al. examining the potential of manganese-based contrast agents[43], and recent research has demonstrated that ultra-small SPIONs in the region of 3-5 nm can be synthesised on a large scale, clear renally, and demonstrate enhanced T_1 contrast compared to gadolinium-chelates while also posing fewer safety risks[45]. This suggests that the future of MRI contrast may well move towards nanoparticle-based materials, primarily iron oxide, though manganese-containing nanoparticles and SPIONs doped with other agents such as cobalt have also been developed.

Manganese has a maximum of five unpaired electrons in the high spin state, not as high as gadolinium, but significant. There is some evidence that naked manganese also poses health risks to patients, but in chelating molecules, liposomal preparations, or in silica nanoparticles as discussed previously in this introduction, manganese can generate effective T_1 contrast[43]. Studies have also doped iron oxide nanoparticles with manganese to enhance T_2 relaxivity[43,46].

1.2.3.2 T_2 CONTRAST AGENTS

T_2 contrast agents are generally based around superparamagnetic iron oxide nanoparticles (SPIONs)[47], SPIONs with a core diameter of less than 20 nm display superparamagnetic behaviour (please see the next section for a discussion of superparamagnetism) which allows them to function as MRI contrast agents through creating local inhomogeneities in the magnetic field which greatly reduce the transverse relaxation time of water molecules. SPIONs have the distinct advantage of being much less toxic than traditional T1 agents because the body has effective mechanisms in place to deal with iron overload. SPIONs are also hugely tunable agents with a range of characteristics which can be altered to enhance contrast agent behaviour, including composition, size, shape, surface functionalisation, and particle charge. All of these properties are discussed in much greater depth in chapter 2.

SPIONs also have theranostic potential in hyperthermia treatments for cancers. SPIONs have been demonstrated to accumulate in tumours through the enhanced permeability and retention (EPR) effect, due to the leaky vasculature formed through tumour angioneogenesis. It is then possible to apply radiowaves to tumours, causing the SPIONs to vibrate and heat up surrounding tissue in the region of 40 ˚C, causing apoptosis of cells specifically in the overheated region.

1.2.4 MAGNETISATION

1.2.4.1 DIAMAGNETISM VS PARAMAGNETISM

The magnetic properties of a material are yet another aspect which is governed by the material structure. In the case of magnetism, the electronic structure of the material is what determines its behaviour. There are many kinds of magnetism, but at the most superficial level materials are either paramagnetic or diamagnetic (figure 1.10)

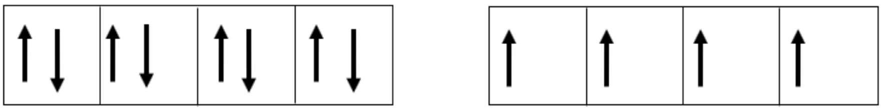

FIGURE 1.10: ILLUSTRATION OF THE ELECTRONIC STRUCTURE OF A DIAMAGNETIC MATERIAL (L) AND A PARAMAGNETIC MATERIAL (R)

Diamagnetic materials have no unpaired electrons in their structure, and this results in no bulk magnetic moment when exposed to an external magnetic field. All materials display some degree of diamagnetism but in materials with unpaired electrons (paramagnetic) other forms of magnetism come to dominate. In a diamagnetic material the orbital motion of the electrons results in a repulsion from an external magnetic field, but this tends to be a weak force which is difficult to detect.

Paramagnetic materials have unpaired electrons within their structure, allowing the magnetic moments of those electrons to align with the field rather than being cancelled out by neighbouring electrons as a result of the Pauli exclusion principle. These unpaired electrons aligning with the field in a low energy state results in a net magnetic moment when an external field is applied, and the loss of magnetism when the field is removed. Paramagnetic materials display a weak attraction to external magnets. Paramagnetism is the basis for MRI contrast agents, most notably gadolinium(III)-based T_1 contrast agents.

According to Curie's law, paramagnetic materials increase in magnetic susceptibility as temperature decreases. In some materials, spins are still disordered at absolute zero meaning that these materials are paramagnetic in the ground state, rather than being ferro-, ferri-, or antiferro-magnetic.

1.2.4.2 SUPERPARAMAGNETISM

Superparamagnetism arises in materials which are small enough to consist of one single magnetic domain. The diameter of nanoparticle required for superparamagnetic behaviour depends on each individual behaviour. When the domain is sufficiently small, it behaves as a single giant magnetic moment which is the sum of all individual atomic magnetic moments within the domain or nanoparticle. The superparamagnetic state arises when the time between magnetisation flips is longer than the Neel relaxation time and magnetisation appears to be zero. When magnetised by an external field, the magnetic susceptibility of superparamagnetic substances is much larger than paramagnets.

Superparamagnetic iron oxide nanoparticles can be used as MRI contrast agents on the basis of this behaviour, and their higher magnetic susceptibility means that they show stronger contrast than paramagnetic gadolinium complexes. Commercialisation and widespread clinical use has not yet caught on for several reasons including negative vs positive contrast, and potential issues with synthesis and quality control. Nanoparticles are an unknown in terms of long term effects, but the body has methods for processing excess iron in the body whereas toxicity concerns over gadolinium complexes are only increasing.

1.2.4.3 FERROMAGNETISM, ANTIFERROMAGNETISM, AND FERRIMAGNETISM

Ferromagnetism is the strongest of the magnetic forces a material can display. It is the basis for permanent magnetic behaviour, or attraction to magnets. A material is ferromagnetic only if all magnetic ions contribute to the net magnetisation of the material. If any ions are aligned against the net magnetisation, the material is ferrimagnetic. Antiferromagnetism occurs when those moments aligned with the field, and those aligned against, perfectly cancel each other out resulting in a net zero magnetic moment for the material. These three magnetic moments are illustrated in figure 1.11.

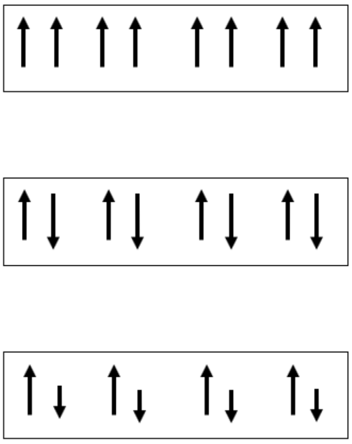

FIGURE 1.11: ILLUSTRATION OF MAGNETIC MOMENTS IN FERRO- (TOP), ANTIFERRO- (MIDDLE), AND FERRIMAGNETIC (BOTTOM) MATERIALS

As before, magnetic behaviour including spontaneous magnetisation is temperature dependent, with magnetic susceptibility increasing inverse to temperature. Above the Curie temperature of each material, the materials become paramagnetic rather than ferri- or ferro-magnetic, so they still respond to an external field but can no longer behave as permanent magnets.

1.3 ATHEROSCLEROSIS

1.3.1 CARDIOVASCULAR DISEASE

Cardiovascular disease (CVD) is now the leading cause of death worldwide, and a classification which includes multiple pathologies including atherosclerosis. Atherosclerosis is a chronic, lipid-driven, inflammatory disease involving the deposition of plaque in the walls of blood vessels (figure 1.12). This plaque can rupture, resulting in myocardial infarction or stroke. Atherosclerosis is often asymptomatic, particularly in cases of vulnerable plaque rupture, and according to the British Heart Foundation, survival rates for out-of-hospital cardiac arrests (as measured by patients subsequently discharged alive from hospital) remain below 10%[48].

CVD therefore represents a huge burden on health services, and on national budgets. Although deaths resulting from CVD are declining, increased survival rates often mean increased costs in terms of productivity and long-term care costs, particularly in survivors of stroke. According to the European Cardiovascular Disease Statistics 2017 report, CVD cost the UK in excess of €26 billion in 2015[48].

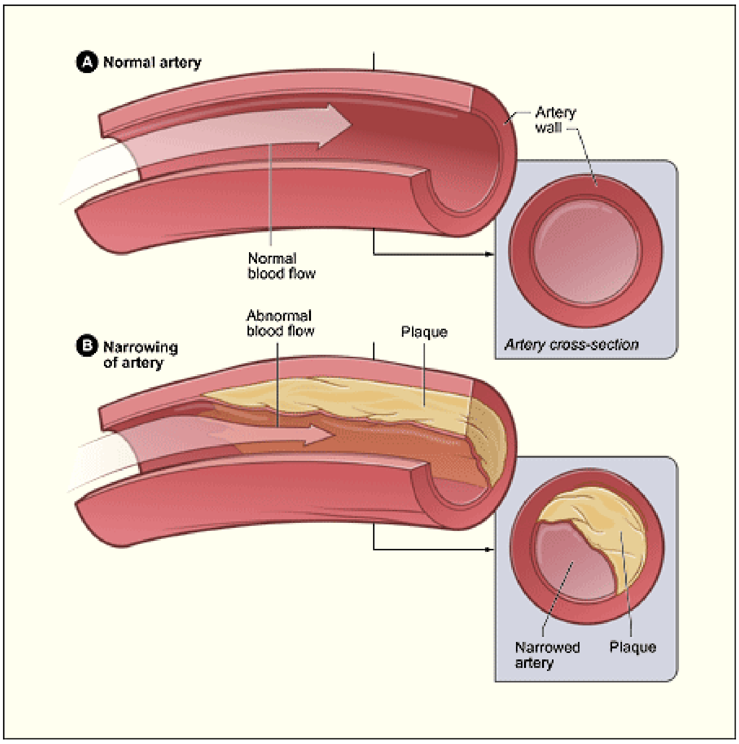

FIGURE 1.12: ILLUSTRATION OF PLAQUE IN ATHEROSCLEROSIS COMPARING A HEALTHY AND DISEASED ARTERY (PUBLIC DOMAIN IMAGE BY NHLBI)

1.3.2 PLAQUE FORMATION

Plaque deposition occurs in areas of low and oscillatory shear stress, for example close to bifurcations in vessels[49,50]. These plaques tend to take two forms, vulnerable or stable, but are initiated in the same way. Vulnerable plaque arises in areas of low shear stress, whereas stable plaque deposits occur in areas of oscillatory shear stress[49–52].

The hallmarks of vulnerable plaque are a high burden of inflammatory macrophages and a large necrotic core, with a thin cap of smooth muscle cells which is prone to rupture, resulting in the exposure of the fibrin-rich core to the blood stream and the formation of a thrombus[47,53]. Thrombii can have major and fatal consequences, including myocardial infarction and stroke. This plaque rupture and thrombus formation is the common cause of death by atherosclerosis. Stable plaque is rich in collagen and smooth muscle cells, with a much smaller macrophage burden.

The alterations in shear stress result in dysfunctional endothelium, allowing lipids to diffuse into the vessel wall[51,54]. This triggers an immune response, resulting in the extravasation of monocytes in an attempt to resolve the inflammation. However, the inflammation remains unresolved and monocytes continue to extravasate, resulting in an initial macrophage burden and the formation of a 'fatty streak' in the vessel wall[51].

The LDL (low-density lipoprotein) is oxidised in the vessel wall and ingested by macrophages, resulting in the formation of foam cells[51,55]. These foam cells are no longer efficient in efferocytosis of dead cell debris, or in the clearance of further lipids by phagocytosis[56,57]. The deficient cell clearance mechanisms mean that when these immune cells die, they are not cleared properly and tend to undergo necrosis rather than apoptosis. The inflammatory processes effectively form positive feedback loops resulting in the continued extravasation of immune cells and the build-up of the large necrotic core which is a hallmark of vulnerable plaque. This process is shown in figure 1.13.

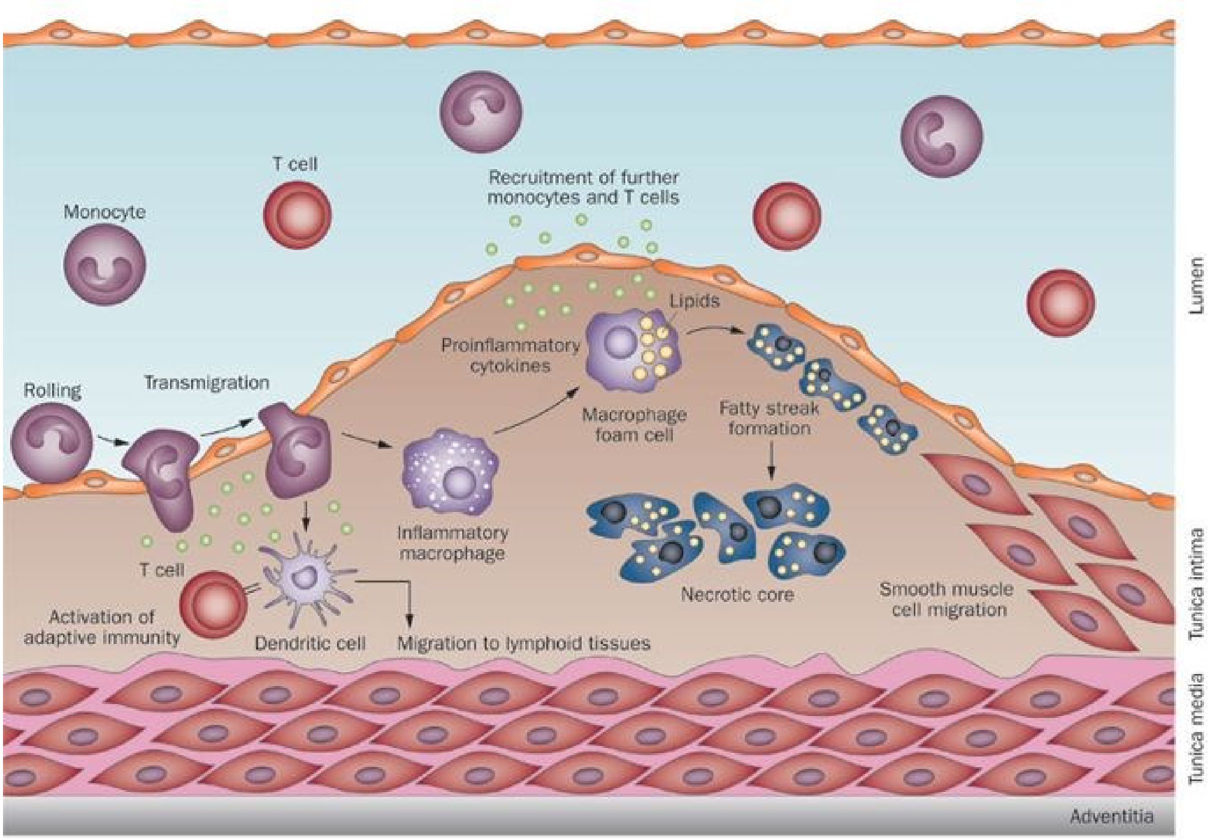

FIGURE 1.13: FIGURE ILLUSTRATING THE FORMATION OF ATHEROSCLEROTIC PLAQUE TAKEN FROM MONOCYTE SUBPOPULATIONS AND CARDIOVASCULAR RISK IN CHRONIC KIDNEY DISEASE BY HEINE ET. AL.[58] AND USED WITH PERMISSION FROM SPRINGERNATURE

1.3.3 PLAQUE PHENOTYPES

Plaque is generally classified under two categories: vulnerable and stable, illustrated in figure 1.14.

Stable plaque is so-called because its thick fibrous cap and small lipid core and macrophage burden makes it much less prone to rupture. Stable plaque can be symptomatic because it involves inward remodelling of the vessel, restricting the lumen and reducing blood flow. This is a common cause of angina, particularly chest pain on exercise when the increased oxygen demand leaves the narrowed vessel unable to keep up. Stable plaque occurs in areas of oscillatory shear stress.

Vulnerable plaque occurs in areas of low shear stress, such as bifurcations, and is characterised by a thin fibrous cap (it is also known as Thin-Cap Fibroatheroma or TCFA), a large necrotic core, and a high burden of inflammatory macrophages. Vulnerable plaque is associated with outward remodelling where the lumen of the blood vessel remains largely unrestricted and thus is asymptomatic. The thin fibrous cap leaves so-called vulnerable plaque prone to rupture, particularly through erosion at the shoulder of the plaque or as a result of higher levels of matrix metalloproteinases (MMPs) digesting the extracellular matrix (ECM) proteins of the cap. The rupture of the cap brings the hugely thrombogenic material in the necrotic core of the plaque into contact with the blood stream, resulting in a thrombus. This can then go on to occlude a coronary artery resulting in a myocardial infarction, or a carotid artery, causing a stroke. If it occurs in a peripheral artery it can cause damage to limbs.

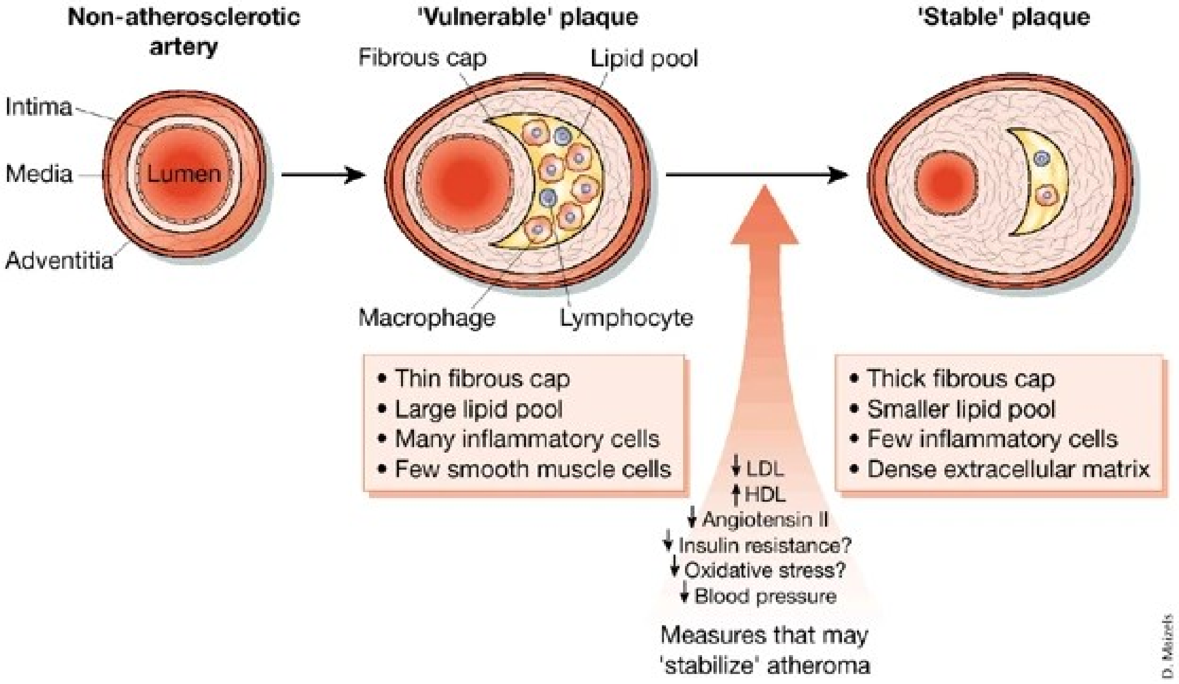

FIGURE 1.14: FIGURE ILLUSTRATING PLAQUE PHENOTYPES AND PROGRESSION INCLUDING THE ROLE OF VARIOUS FACTORS, TAKEN FROM STABILIZATION OF ATHEROSCLEROTIC PLAQUES: NEW MECHANISMS AND CLINICAL TARGETS BY LIBBY AND AIKAWA[59] AND USED WITH PERMISSION FROM SPRINGERNATURE.

Currently there is not a reliable technique to differentiate between vulnerable and stable plaques through non-invasive imaging means, and the aim of this project is to develop a contrast agent which is specific to vulnerable plaque, enabling the identification and treatment of vulnerable plaques before events which can lead to death or reduced quality of life.

1.3.4 MACROPHAGES

Monocytes are circulating immune cells which can express different phenotypes. When discussing atherosclerosis the ones of primary interest are Ly6C^{hi} and Ly6C^{lo} cells, which roughly correspond to CD14^{+}CD16^{-} and CD14^{dim}CD16^{+} cells in humans[60,61]. There is not a direct parallel because in mice the numbers of each class are roughly equal, but in humans CD14^{+}CD16^{-} cells account for 85-90% of circulating monocytes, with CD14dim cells accounting for the remaining 15%[56,61]. Ly6C^{lo}/CD14^{dim} cells are 'patrolling' monocytes which adhere to the vessel wall[61].

Monocytes differentiate into macrophages when they extravasate into tissue, and macrophages are very complex and plastic cells which can express a whole variety of receptors and phenotypes. Although classically they were divided into M1 and M2 cells, more recent thought considers macrophage polarisation to be on a spectrum rather than a permanent state, and new classifications of macrophages have also arisen. M2 cells can be subdivided into M2a, M2b, M2c and sometimes even M2d cells, M4 cells have been identified in atherosclerotic plaque, as have M_{ox}, M_{hem} and M_{Ha} cells[52,62–66]. The wide variety of macrophage phenotypes present in plaque confirm that it is a very complex environment, and it would be foolish to assume that targeting one 'cell type' is simple.

In broad terms, M1 macrophages are pro-inflammatory cells. They tend to differentiate from Ly6C^{hi}/CD14^{+} cells after exposure to interferon-γ (IFN-γ) and lipopolysaccharide (LPS) which is a toll-like receptor (TLR) ligand[63,67]. M1 cells express high levels of CCR1, CCR2 and CCR5. They also express CX3CR1, albeit at lower levels than Ly6C^{lo}/CD14^{dim} cells. Despite the lower level of CX3CR1 expression, Ly6C^{hi}/CD14^{+} monocytes have been shown to use a combination of CCR2, CCR5 and CX3CR1 to extravasate into the vessel wall[67,68], with blocking of these three axes resulting in a 90% decrease in plaque volume[69]. Ly6C^{lo}/CD14^{dim} cells express higher levels of CX3CR1 but have been shown to extravasate using other methods[68].

Although M2, or anti-inflammatory macrophages tend to be present at the early stages[67], as the inflammation remains unresolved the M1 macrophage burden increases, exacerbating the inflammation[68]. This is a way to identify more advanced lesions, and likely arises in humans due to the much higher proportion of Ly6C^{hi} precursors which are in circulation and their efficient extravasation.

Although the more recent view is that macrophages in plaque tend to increase via proliferation rather than constant recruitment, if recruitment is blocked then proliferation cannot continue indefinitely. The range of immune cells associated with atherosclerosis can be seen in figure 1.15.

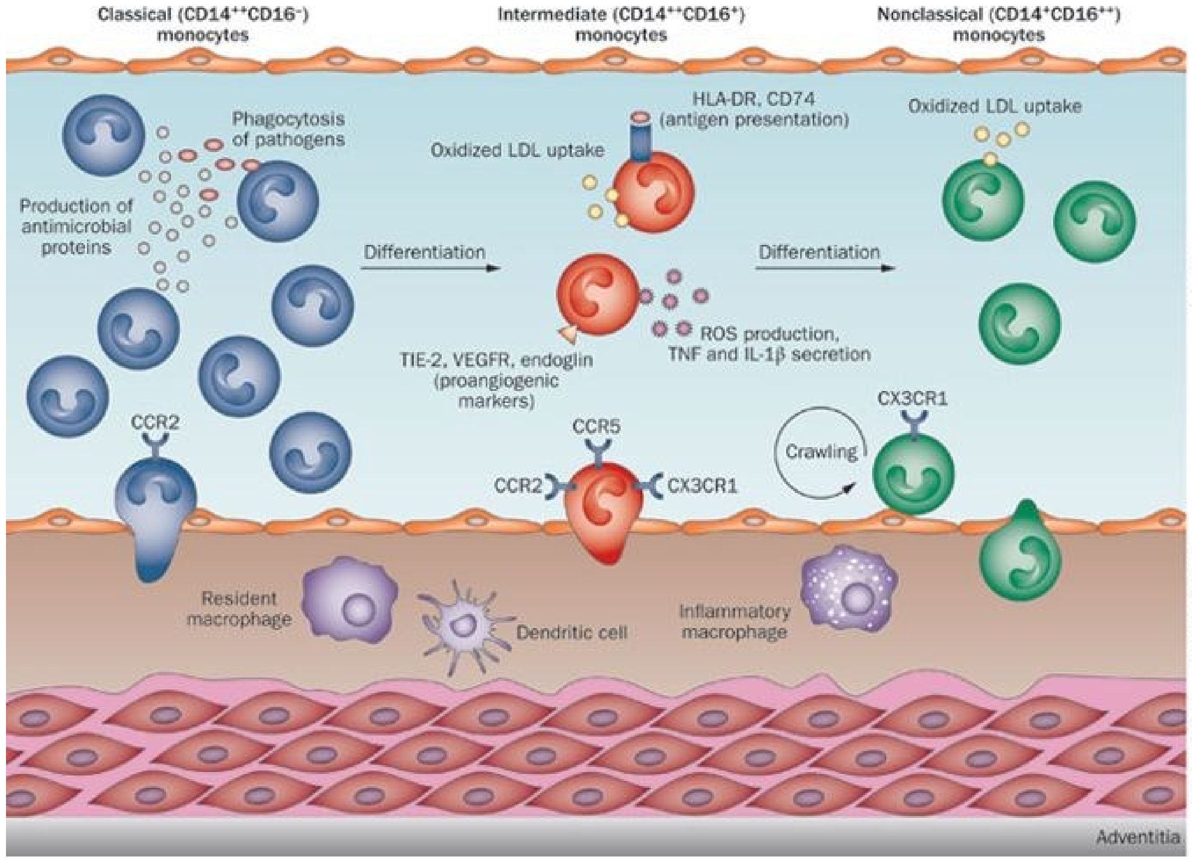

FIGURE 1.15: FIGURE ILLUSTRATING THE DIFFERENT POPULATIONS OF MONOCYTES ASSOCIATED WITH ATHEROSCLEROTIC PLAQUE AND THEIR ROLES, TAKEN FROM MONOCYTE SUBPOPULATIONS AND CARDIOVASCULAR RISK IN CHRONIC KIDNEY DISEASE BY HEINE ET. AL.[58] AND USED WITH PERMISSION FROM SPRINGER NATURE.

1.3.5 THE ROLE OF FRACTALKINE (CX3CL1)

CX3CR1 is the receptor for the ligand fractalkine (CX3CL1), a unique chemokine which is the only member of the CX3C family of chemokines (small cytokines with chemotactic properties). Fractalkine has a unique structure in that it has both a soluble and a bound form. The ligand is expressed on a long mucin-like stalk protruding from the vessel wall (figure 1.16). It is often expressed on cardiac smooth muscle cells, although it is only expressed in damaged rather than healthy arteries, and studies have shown that it is overexpressed in the vulnerable plaque phenotype, rather than in the stable plaque[49,70–73].

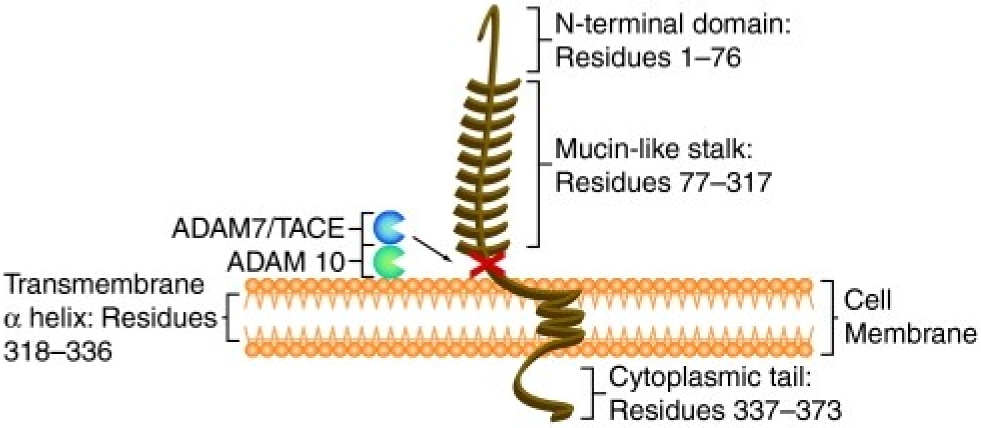

FIGURE 1.16: FIGURE ILLUSTRATING THE STRUCTURE OF FRACTALKINE (CX3CL1) AND WHERE IT SITS IN THE CELL MEMBRANE, TAKEN FROM FRACTALKINE/CX3CL1: A POTENTIAL NEW TARGET FOR INFLAMMATORY DISEASES BY B. A. JONES ET. AL.[73] AND USED UNDER CC BY-NC-ND 3.0.

Adhesion of CX3CR1 expressing cells to CX3CL1 is an effective method of extravasation and is somewhat unique in being an integrin-independent adhesion mechanism[69] illustrated in figure 1.17. It has been shown to tether cells even in under flow conditions[73], and so CX3CL1 expression is linked to higher levels of more efficient monocyte extravasation, resulting in an accumulation of macrophages in the vessel wall. A high macrophage burden is a characteristic of vulnerable plaque, and the apoptosis of these cells in combination with a defective efferocytosis mechanism results in the formation of a necrotic core[56,57].

When the monocytes extravasate into the vessel wall, they phagocytose the lipids in an attempt to resolve the cause of the inflammation there. These lipids have often been oxidised in the environment resulting in oxLDL. Work by Barlic et al. seemed to demonstrate that exposure to major components of oxLDL resulted in a switch of chemokine receptor expression[55]. CCR2 was downregulated and CX3CR1 was hugely upregulated. This has a two-fold effect in that it mediates adhesion of monocytes and macrophages to the smooth muscle cells, and CX3CR1 expression has also been linked to cell survival[69].

All of these factors in concert would explain the formation of the necrotic core in vulnerable plaque: higher levels of CX3CL1 expression resulting in enhanced adhesion and extravasation of monocytes, particularly in the presence of oxLDL switching chemokine receptor expression to upregulate CX3CR1 expression in pro-inflammatory, pro-atherogenic cells. It would also explain why the blocking of CX3CL1 using antibodies was shown to result in an increase in plaque stability, and even regression[49,69,72,74].

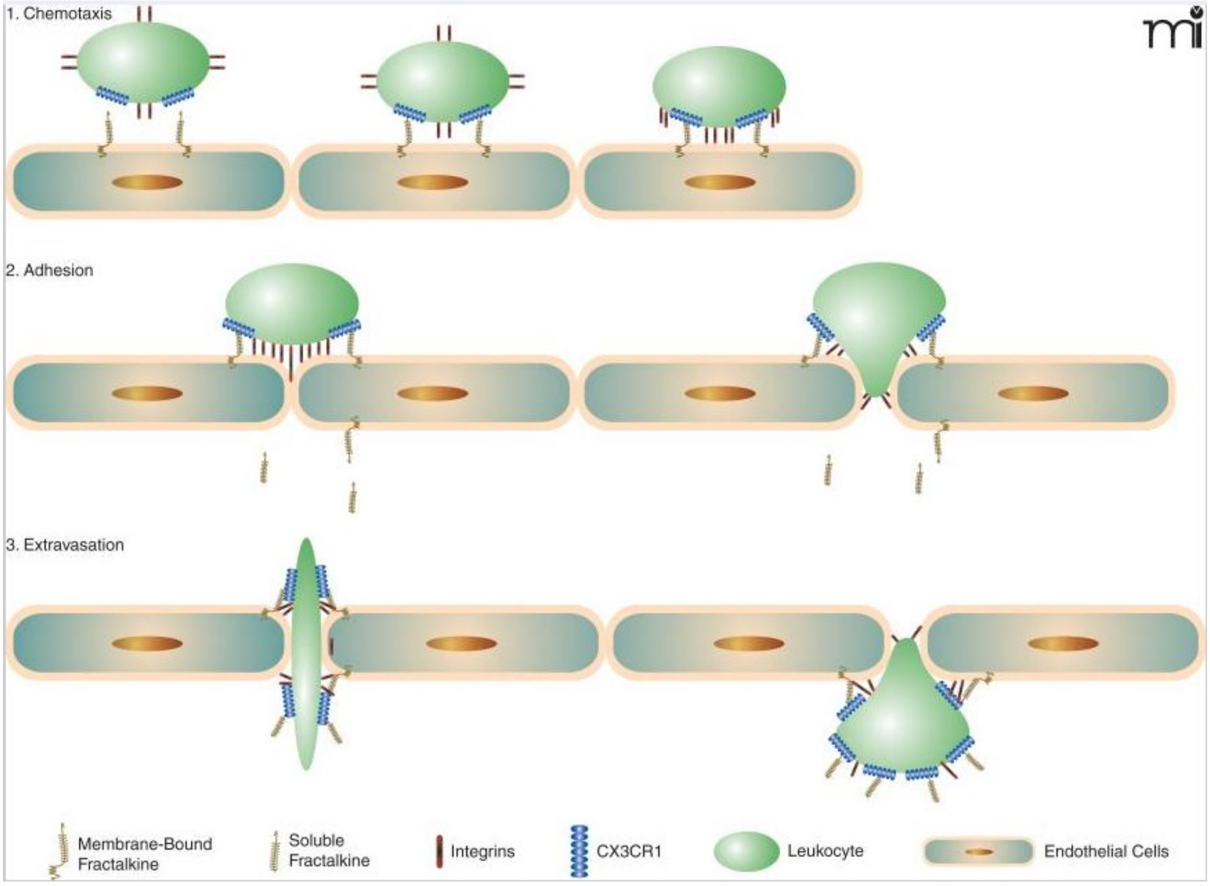

FIGURE 1.17: FIGURE ILLUSTRATING THE PROCESS OF EXTRAVASATION BY ADHESION TO CX3CL1 TAKEN FROM FRACTALKINE/CX3CL1: A POTENTIAL NEW TARGET FOR INFLAMMATORY DISEASES BY B. A. JONES ET. AL.[73] AND USED UNDER CC BY-NC-ND 3.0.

That is not to say that fractalkine is the only suitable target for imaging atherosclerosis, indeed work is being undertaken into many other targets including, but not limited to: hypoxia[47,53,75], apoptosis[53,75–77], angioneogenesis[47,78], collagen[22,75], fibrin[43,75,79], platelets and selectins[47,69,71,75,80], Vascular Adhesion Molecule 1 (VCAM-1)[75,79,81], αvβ3 integrin[47], and Vascular Endothelial Growth Factor (VEGF)[82]. All of these targets do not have a high degree of specificity for vulnerable plaque, and can be associated with other conditions, most notably cancer.

There is also a range of chemokines expressed at high levels in atherosclerosis including CCL5 (RANTES)[69,72,74,82,83], CCR2 (MCP-1)[69,72,74,82,83], macrophage inflammatory protein 1α/β (MIP-1α/β)[72,82], high-sensitivity C reactive protein (hCRP)[82,83], and macrophage migration inhibitory factor[72]. CCR5 and CCR2 can be inhibited alongside fractalkine to result in a ~90% reduction of plaque burden[67], and CCR5 and CCR2 are expressed at the early stages of plaque development alongside fractalkine[72]. MIP-1β alongside tumour necrosis factor α (TNF-α) and interferon-γ (INF-γ) is more associated with vulnerable plaque. TNF-α and INF-γ are involved in the polarisation of macrophages towards an inflammatory M1 phenotype[63,67].

Fractalkine displays notable advantages over these other potential targets due to being a biomarker specifically for vulnerable plaque and present through the course of disease, as well as being potentially theranostic if the contrast agent is designed to block expression as well as generate a signal for imaging purposes.

1.4 THE CONTEXT AND AIMS OF THE PROJECT

There is a need for early detection and identification of vulnerable plaque to reduce cardiovascular disease-related mortality. Medical imaging can non-invasively provide diagnostic information and guide treatment, particularly in conjunction with an appropriate biomarker. MRI has particular advantages in terms of its anatomical detail, its resolution and contrast, and its safety. Fractalkine has unique features which make it a potential biomarker of particular interest.

We therefore hypothesise that superparamagnetic iron oxide nanoparticles targeted to fractalkine will be a specific, non-toxic contrast agent for the identification of vulnerable atherosclerotic plaque.

The aims of this project are as follows:

- To synthesise a range of superparamagnetic iron oxide nanoparticles, varying core size and surface ligands.
- To characterise those agents with respect to size, stability, surface charge, and relaxivity.
- To conjugate an anti-CX3CL1 antibody to the surface of the SPION which demonstrates the best properties for a long-circulating *in vivo* contrast agent.
- To test the contrast agent in a murine model of atherosclerosis and perform histological and *in vitro* studies to support the preclinical work.
- To carry out a second phase of nanoparticle development, building on the lead candidate identified in phase one, moving towards the synthesis of a multi-modal nanoparticle contrast agent.

1.5 REFERENCES

1 G.-L. Law and W. T. Wong, in *The Chemistry of Molecular Imaging*, eds. N. J. Long and W. T. Wong, John Wiley & Sons Inc., 1st edn., 2015, pp. 1–24.

2 D. J. Brenner and E. J. Hall, *N. Engl. J. Med.*, 2007, **357**, 2277.

3 L. Hrvoje and M. W. Greenstaff, *Chem. Rev.*, 2014, **113**, 1641–1666.

4 P. M. Herst and M. V. Berridge, *Curr. Pharm. Biotechnol.*, 2013, **14**, 289–299.

5 T. F. Massoud, T. F. Massoud, S. S. Gambhir and S. S. Gambhir, *Genes Dev.*, 2003, **17**, 545–580.

6 P. J. Blower, *Dalt. Trans.*, 2015, **44**, 4819–4844.

7 L. Goense, J. P. Ruurda, B. W. Carter, P. Fang, L. Ho, G. J. Meijer, R. van Hillegersberg, W. L. Hofstetter and S. H. Lin, *Eur. J. Nucl. Med. Mol. Imaging*, 2018, **45**, 1742–1751.

8 T. G. Papaioannou, C. Kalantzis, E. Katsianos, D. Sanoudou, M. Vavuranakis and D. Tousoulis, *J. Pers. Med.*, 2019, **9**, 8.

9 M. J. K. Blomley, J. C. Cooke, E. C. Unger, M. J. Monaghan and D. O. Cosgrove, *Br. Med. J.*, 2001, **322**, 1222–1225.

10 K. Ferrara, R. Pollard and M. Borden, *Annu. Rev. Biomed. Eng.*, 2007, **9**, 415–447.

11 S. V. Morse, A. N. Pouliopoulos, T. G. Chan, M. J. Copping, J. Lin, N. J. Long and J. J. Choi, *Radiology*, 2019, **291**, 459–466.

12 T. G. Chan, S. V. Morse, M. J. Copping, J. J. Choi and R. Vilar, *ChemMedChem*, 2018, **13**, 1311–1314.

13 K. Hansen, M. Nielsen and C. Ewertsen, *Diagnostics*, 2015, **6**, 2.

14 M. F. Bode and F. A. Jaffer, *Curr. Cardiovasc. Imaging Rep.*, 2019, **12**, 1–11.

15 J. Kim, W. Brown, J. R. Maher, H. Levinson and A. Wax, *Phys. Med. Biol.*, 2015, **60**, R211-37.

16 D. Huang, E. A. Swanson, C. P. Lin, J. S. Schuman, W. G. Stinson, W. Chang, M. R. Hee, T. Flotte, K. Gregory, C. A. Puliafito and J. G. Fujimoto, *Sci. Novemb.*, 1991, **22**, 1178–1181.

17 A. de la Zerda, S. Prabhulkar, V. L. Perez, M. Ruggeri, A. S. Paranjape, F. Habte, S. S. Gambhir and R. M. Awdeh, *Clin. Experiment. Ophthalmol.*, 2015, **43**, 358–366.

18 J. Hu, D. Romero Abujetas, D. Tsoutsi, L. Leggio, F. Rivero, E. Martín Rodríguez, R. Aguilar Torres, J. A. Sánchez-Gil, H. Loro Ramírez, D. Gallego, H. Lamela Rivera, P. Rivera Gil, F. Alfonso, J. García Solé and D. Jaque, *APL Photonics*, 2018, **3**, 1–14.

19 L. E. Jennings and N. J. Long, *Chem. Commun.*, 2009, 3511.

20 J. Xie, S. Lee and X. Chen, *Adv. Drug Deliv. Rev.*, 2010, **62**, 1064–1079.

21 Y. Ali, A. Alqudah, S. Ahmad, S. Abd Hamid and U. Farooq, *Des. Monomers Polym.*, 2019, **22**, 91–97.

22 G. S. van Bochove, H. M. H. F. Sanders, M. de Smet, H. M. Keizer, W. J. M. Mulder, R. Krams, G. J. Strijkers and K. Nicolay, *Eur. J. Inorg. Chem.*, 2012, **2012**, 2115–2125.

23 V. Amirbekian, M. J. Lipinski, K. C. Briley-Saebo, S. Amirbekian, J. G. S. Aguinaldo, D. B. Weinreb, E. Vucic, J. C. Frias, F. Hyafil, V. Mani, E. A. Fisher and Z. A. Fayad, *Proc. Natl. Acad. Sci. U. S. A.*, 2007, **104**, 961–966.

24 J. L. J. Dearling and A. B. Packard, *J. Control. Release*, 2017, **261**, 23–30.

25 T. Nann, *Nano Biomed. Eng.*, 2011, **3**, 137–143.

26 X. Li, C. Wang, H. Tan, L. Cheng, G. Liu, Y. Yang, Y. Zhao, Y. Zhang, Y. Li, C. Zhang, Y. Xiu, D. Cheng and H. Shi, *Biomaterials*, 2016, **108**, 71–80.

27 L. Han, Y. Zhang, Y. Zhang, Y. Shu, X. W. Chen and J. H. Wang, *Talanta*, 2017, **171**, 32–38.

28 V. Dugandžić, D. Drikermann, O. Ryabchykov, A. Undisz, I. Vilotijević, S. Lorkowski, T. W. Bocklitz, C. Matthäus, K. Weber, D. Cialla-May and J. Popp, *J. Biophotonics*, 2018, **11**, 1–12.

29 S. J. Cho, B. R. Jarrett, A. Y. Louie and S. M. Kauzlarich, *Nanotechnology*, 2006, **17**, 640–644.

30 H. Yin, S. Dai, C. Wang, S. Peng, Y. Lee and S. Sun, *Nano Res.*, 2008, **1**, 229–234.

31 M. M. Van Schooneveld, D. P. Cormode, R. Koole, J. T. Van Wijngaarden, C. Calcagno, T. Skajaa, J. Hilhorst, D. C. 'T Hart, Z. A. Fayad, W. J. M. Mulder and A. Meijerink, *Contrast Media Mol. Imaging*, 2010, **5**, 231–236.

32 Y. Z. Shao, L. Z. Liu, S. Q. Song, R. H. Cao, H. Liu, C. Y. Cui, X. Li, M. J. Bie and L. Li, *Contrast Media Mol. Imaging*, 2011, **6**, 110–118.

33 I. I. Slowing, J. L. Vivero-Escoto, C. W. Wu and V. S. Y. Lin, *Adv. Drug Deliv. Rev.*, 2008, **60**, 1278–1288.

34 I. I. Slowing, B. G. Trewyn, S. Giri and V. S. Y. Lin, *Adv. Funct. Mater.*, 2007, **17**, 1225–1236.

35 R. Ji, X. Li, C. Zhou, Q. Tian, C. Li, S. Xia, R. Wang, Y. Feng and W. Zhan, *Nanoscale*, 2018, **10**, 20246–20255.

36 D. Ling, N. Lee and T. Hyeon, *Acc. Chem. Res.*, 2015, **48**, 1276–1285.

37 N. Insin, J. B. Tracy, H. Lee, J. P. Zimmer, R. M. Westervelt and M. G. Bawendi, *ACS Nano*, 2008, **2**, 197–202.

38 D. K. Yi, S. T. Selvan, S. S. Lee, G. C. Papaefthymiou, D. Kundaliya and J. Y. Ying, *J. Am. Chem. Soc.*, 2005, **127**, 4990–4991.

39 Y. Zhou, G. Quan, Q. Wu, X. Zhang, B. Niu, B. Wu, Y. Huang, X. Pan and C. Wu, *Acta Pharm. Sin. B*, 2018, **8**, 165–177.

40 C. Y. Lai, B. G. Trewyn, D. M. Jeftinija, K. Jeftinija, S. Xu, S. Jeftinija and V. S. Y. Lin, *J. Am. Chem. Soc.*, 2003, **125**, 4451–4459.

41 P. Eskandari, B. Bigdeli, M. Porgham Daryasari, H. Baharifar, B. Bazri, M. Shourian, A. Amani, A. Sadighi, B. Goliaei, M. Khoobi and A. A. Saboury, *J. Drug Target.*, 2019, **0**, 1–10.

42 Z. T. Shen, S. Zheng, M. J. Gounis and A. B. Sigalov, *PLoS One*, 2015, **10**, e0143453.

43 D. Pan, S. D. Caruthers, A. Senpan, A. H. Schmieder, S. A. Wickline and G. M. Lanza, *Wiley Interdiscip. Rev. Nanomedicine Nanobiotechnology*, 2011, **3**, 162–173.

44 V. Gulani, F. Calamante, F. G. Shellock, E. Kanal and S. B. Reeder, *Lancet Neurol.*, 2017, **16**, 564–570.

45 U. I. Tromsdorf, O. T. Bruns, S. C. Salmen, U. Beisiegel and H. Weller, *Nano Lett.*, 2009, **9**, 4434–4440.

46 S. Sun, H. Zeng, D. B. Robinson, S. Raoux, P. M. Rice, S. X. Wang, G. Li, S. X. Wand and G. Li, *J. Am. Chem. Soc.*, 2004, **126**, 273–279.

47 M. E. Lobatto, V. Fuster, Z. A. Fayad and W. J. M. Mulder, *Nat. Rev. Drug Discov.*, 2011, **10**, 835–852.

48 British Heart Foundation, *BHF CVD STATISTICS COMPENDIUM 2017*, 2017.

49 C. Cheng, D. Tempel, R. van Haperen, H. C. de Boer, D. Segers, M. Huisman, A. J. van Zonneveld, P. J. M. Leenen, A. van der Steen, P. W. Serruys, R. de Crom and R. Krams, *J. Clin. Invest.*, 2007, **117**, 616–626.

50 R. M. Pedrigi, R. De Silva, S. M. Bovens, V. V. Mehta, E. Petretto and R. Krams, *Arterioscler. Thromb. Vasc. Biol.*, 2014, **34**, 2224–2231.

51 M. Wildgruber, F. K. Swirski and A. Zernecke, *Theranostics*, 2013, **3**, 865–884.

52 A. N. Seneviratne, J. E. Cole, M. E. Goddard, I. Park, Z. Mohri, S. Sansom, I. Udalova, R. Krams and C. Monaco, *J. Mol. Cell. Cardiol.*, 2015, **89**, 168–172.

53 C. Silvestre-Roig, M. P. De Winther, C. Weber, M. J. Daemen, E. Lutgens and O. Soehnlein, *Circ. Res.*, 2014, **114**, 214–226.

54 H. Ait-Oufella, S. Taleb, Z. Mallat and A. Tedgui, *Arterioscler. Thromb. Vasc. Biol.*, 2011, **31**, 969–979.

55 J. Barlic, Y. Zhang, J. Foley and P. Murphy, *Circulation*, 2006, 807–819.

56 G. J. Randolph, *Circ. Res.*, 2014, **114**, 1757–1771.

57 I. Tabas and K. E. Bornfeldt, *Circ. Res.*, 2016, **118**, 653–667.

58 G. H. Heine, A. Ortiz, Z. A. Massy, B. Lindholm, A. Wiecek, A. Martínez-Castelao, A. Covic, D. Goldsmith, G. Süleymanlar, G. M. London, G. Parati, R. Sicari, C. Zoccali and D. Fliser, *Nat. Rev. Nephrol.*, 2012, **8**, 362–369.

59 P. Libby and M. Aikawa, *Nat. Med.*, 2002, **8**, 1257–1262.

60 K. J. Woollard, *Clin. Sci.*, 2013, **125**, 221–235.

61 K. J. Woollard and F. Geissmann, *Nat. Rev. Cardiol.*, 2010, **7**, 77–86.

62 S. Colin, G. Chinetti-Gbaguidi and B. Staels, *Immunol. Rev.*, 2014, **262**, 153–166.

63 M. A. Hoeksema, J. L. Stöger and M. P. J. De Winther, *Curr. Atheroscler. Rep.*, 2012, **14**, 254–263.

64 C. A. Gleissner, *Front. Physiol.*, 2012, **3 JAN**, 1–7.

65 C. Cochain and A. Zernecke, *Basic Res. Cardiol.*, 2015, **110**, 1–12.

66 J. J. Boyle, *Curr. Opin. Lipidol.*, 2012, **23**, 453–61.

67 K. J. Moore, F. J. Sheedy and E. a Fisher, *Nat. Rev. Immunol.*, 2013, **13**, 709–21.

68 P. L. Taghavie-Moghadam, M. J. Butcher and E. V. Galkina, *Ann. N. Y. Acad. Sci.*, 2014, **1319**, 19–37.

69 S. Apostolakis and D. Spandidos, *Acta Pharmacol. Sin.*, 2013, **34**, 1251–6.

70 X. Zhang, X. Feng, W. Cai, T. Liu, Z. Liang, Y. Sun, C. Yan and Y. Han, *Thromb. Res.*, 2015, **135**, 1147–1153.

71 U. Flierl, J. Bauersachs and A. Schäfer, *Eur. J. Clin. Invest.*, 2015, **45**, 624–633.

72 A. Zernecke and C. Weber, *Cardiovasc. Res.*, 2010, **86**, 192–201.

73 B. A. Jones, M. Beamer and S. Ahmed, *Mol. Interv.*, 2010, **10**, 263–270.

74 P. Nie, D. Li, L. Hu, S. Jin, Y. Yu, Z. Cai, Q. Shao, J. Shen, J. Yi, H. Xiao, L. Shen and B. He, *PLoS One*, 2014, **9**, 1–8.

75 M. Juenet, M. Varna, R. Aid-Launais, C. Chauvierre and D. Letourneur, *Biochem. Biophys. Res. Commun.*, 2015, **468**, 476–484.

76 G. A. F. van Tilborg, E. Vucic, G. J. Strijkers, D. P. Cormode, V. Mani, T. Skajaa, C. P. M. Reutelingsperger, Z. A. Fayad, W. J. M. Mulder and K. Nicolay, *Bioconjug. Chem.*, 2010, **21**, 1794–1803.

77 E. M. Laufer, C. P. M. Reutelingsperger, J. Narula and L. Hofstra, *Basic Res. Cardiol.*, 2008, **103**, 95–104.

78 G. L. Ten Kate, E. J. G. Sijbrands, R. Valkema, F. J. Ten Cate, S. B. Feinstein, A. F. W. Van Der Steen, M. J. A. P. Daemen and A. F. L. Schinkel, *J. Nucl. Cardiol.*, 2010, **17**, 897–912.

79 P. Charoenphol, S. Mocherla, D. Bouis, K. Namdee, D. J. Pinsky and O. Eniola-Adefeso, *Atherosclerosis*, 2011, **217**, 364–370.

80 M. T. Ali, K. Martin, A. H. S. Kumar, E. Cavallin, S. Pierrou, B. M. Gleeson, W. L. McPheat, E. C. Turner, C. L. Huang, W. Khider, C. Vaughan and N. M. Caplice, *Biomaterials*, 2015, **69**, 22–29.

81 K. A. Kelly, J. R. Allport, A. Tsourkas, V. R. Shinde-Patil, L. Josephson and R. Weissleder, *Circ. Res.*, 2005, **96**, 327–336.

82 A. Edsfeldt, H. Grufman, G. Asciutto, M. Nitulescu, A. Persson, M. Nilsson, J. Nilsson and I. Gonçalves, *Atherosclerosis*, 2015, **241**, 443–449.

83 Z. X. Zhong, B. Li, C. R. Li, Q. F. Zhang, Z. D. Liu, P. F. Zhang, X. F. Gu, H. Luo, M. J. Li, H. S. Luo, G. H. Ye and F. L. Wen, *Brazilian J. Med. Biol. Res.*, 2015, **48**, 161–166.

Chapter 2

Development of functionalised nanoparticle contrast agents

2.1 INTRODUCTION

2.1.1 SHAPE

Shape can play an interesting role in the targeting, circulation, and clearance of a nanoparticulate contrast agent, and has been shown to affect phagocytosis more than simple changes in size[1]. There is no shape which is invulnerable to phagocytosis but this provides another route for tuning the contrast agent to maximise targeting through both active and passive routes by reducing the number of orientations from which a particle can be easily engulfed[1,2]. Size and shape also affects endocytosis based targeting of the endothelium[3,4]. Shape affects T_2 relaxivity through the anisotropy which leads to increased local field inhomogeneities[5–7], and ultra-high transverse (T_2) relaxivities have been demonstrated in octapod nanoparticles[8]. Other non-spherical shapes include nanoworms and discoid structures[2,7], with the option to develop lipid-based contrast agents[9] as a way of varying size and concentrating contrast agent in a micelle[10–13] or liposome[13,14]. More information on the range of shapes available for iron oxide nanoparticles can be found in the detailed review by Roca et. al.[15], and an example of the range of shapes available can be seen in figure 2.1.

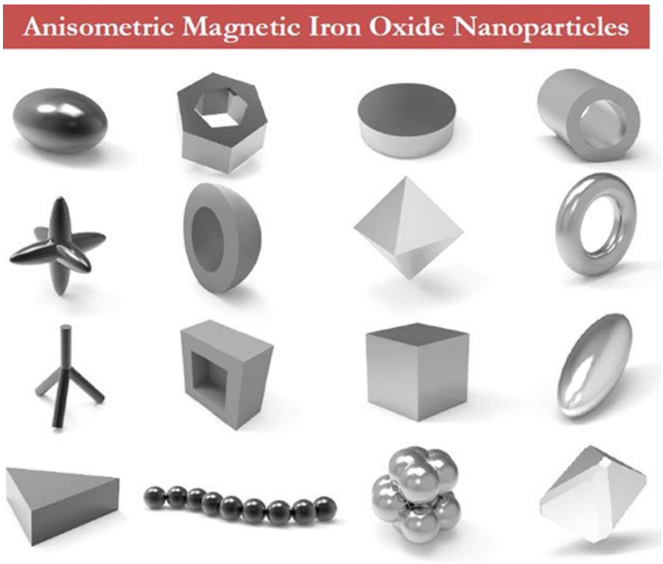

FIGURE 2.1: GRAPHICAL ABSTRACT FROM THE REVIEW BY ROCA ET. AL.[15] SHOWING THE RANGE OF NON-SPHERICAL NANOPARTICLE SHAPES WHICH HAVE BEEN SYNTHESISED.

2.1.2 SIZE

Size is an important consideration for SPION-based contrast agents for several reasons. It is generally accepted that relaxivity varies with size, increasing up to a threshold where the particles no longer behave in a superparamagnetic way (example in figure 2.2). There seems to be no consensus on where this threshold is, with conflicting information ranging from anywhere between 15-30 nm[16–18]. This is also likely to depend on the composition of the particles, which will be addressed further in section 2.1.4.

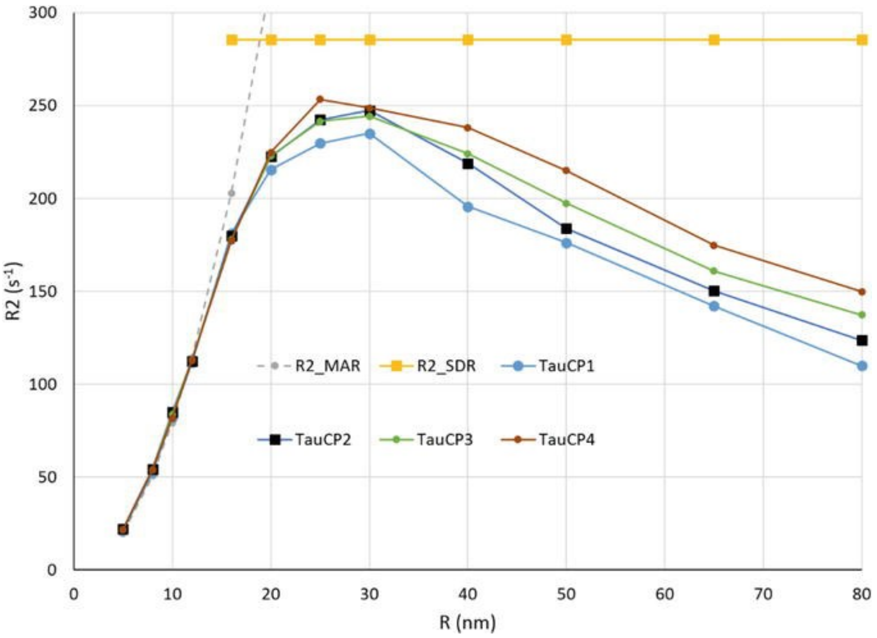

FIGURE 2.2: GRAPH SHOWING A RELATION BETWEEN NANOPARTICLE SIZE AND RELAXIVITY IN A MONTE CARLO SIMULATION TAKEN FROM ISSA AND OBAIDAT[19], DEMONSTRATING THE LIMIT IN RELAXIVITY INCREASE WITH PARTICLE SIZE.

Relaxivity is a measure of efficacy in MRI contrast agents, referring to the change in signal related to the concentration of the contrast agent. Agents with high relaxivities generate greater change in signal (i.e. improved contrast agent) for a lower concentration, meaning that lower dosages are required of contrast agents with high relaxivities. SPION relaxivities tend to be higher than gadolinium complexes for both T_1 and T_2, however the r_2/r_1 ratio (usually regarded as the classification metric for T_1 vs T_2 contrast agents) is high enough to classify them as T_2 agents. Interestingly, ultra-small SPIONs in the region of 3 nm in diameter have shown to be effective T_1 contrast agents, with better relaxivities than some gadolinium complexes currently in clinical use such as Gd-DTPA[20]. This may be the most obvious pathway for SPIONs into clinical use due to the rapid clearance and the positive contrast which is generally favoured by clinicians for diagnostic practice.

Size also dictates *in vivo* behaviour. Particles smaller than 5-6 nm are understood to follow the renal excretion route, which means that clearance from the blood pool is relatively rapid, within a matter of hours[21]. Small molecule gadolinium complexes clear quickly through the kidneys, and in patients with renal failure or late-stage kidney disease poor glomerular filtration results in slow excretion, increasing the probability of gadolinium leaching from the complexes and causing conditions such as nephrogenic system fibrosis, thus making gadolinium complexes inappropriate for use in patients with kidney disease. Some recent studies have also found gadolinium deposits in the brains of patients who have been repeatedly scanned with these contrast agents[22].

The intention of this project is to develop a targeted contrast agent which uses an antibody against a vulnerable plaque-specific protein. Antibody-targeted contrast agents require long circulation times in excess of 24 hours, and occasionally up to several days. This means that the contrast agent must be in excess of 6 nm in diameter to avoid renal clearance.

Above 200 nm, particles are cleared quickly by the reticuloendothelial system (RES), passing through the liver and spleen[21]. This gives a window between 6-200 nm where it is possible to synthesise long-circulating contrast agents. They will eventually be cleared through the RES pathway, with some side products resulting from the degradation of these agents possibly passing through the renal clearance (i.e. if the particles are digested to iron salts).

2.1.3 SURFACE CHARGE

Surface charge affects how SPIONs interact with the immune system. Monocytes and macrophages are prone to phagocytose SPIONs as foreign bodies and this results in both faster clearance through the RES and increased non-specific uptake. Uncoated SPIONs are cleared rapidly from the bloodstream and are also prone to oxidation, therefore the selection of a ligand coating to render the nanoparticle hydrophilic, protect it from oxidation and shield it from the immune system is very important. For molecular contrast agents, the ligand system must also be easy to functionalise with the targeting moiety.

Nanoparticles with neutral surfaces are the most successful in evading the immune system, with a slight negative charge also being quite effective and a positively charged surface often resulting in higher cellular and non-specific uptake, and clearance through the RES[23–25]. Although it is necessary to take into account surface charge when designing a long-circulating contrast agent for targeting purposes, it is impossible to entirely prevent clearance by the immune system. This does not need to be a design flaw, and the likelihood of phagocytosis of the contrast agent by the macrophages present in the plaque is likely to contribute to a high signal-to-noise ratio. Non-specific immune uptake results in background signal but the combination of phagocytosis by the high plaque macrophage burden, active targeting of CX3CL1, and the enhanced permeability and retention (EPR) effect are likely to combine to result in a good specific signal in the area of the plaque.

2.1.4 COMPOSITION

Iron oxide is the most common material for non-gadolinium MRI contrast agents because of its magnetic properties in crystal form, however the modification of the crystal structure to include other metal ions can also affect the behaviour of nanoparticle-based contrast agents.

Sun et. al. developed an approach for synthesising MFe_2O_4 nanoparticles via thermal decomposition, varying the composition with the inclusion of manganese and cobalt in the place of the Fe^{2+} ions in the lattice structure[26] (Figure 2.3). In the cases of both manganese and cobalt, there was no alteration to the crystal structure, which remained a cubic spinel. The introduction of these alternative metal centres into the nanoparticles affected the magnetic anisotropy of the material, which is the most important aspect of a T_2 contrast agent. T_2 agents work by affecting the transverse relaxation of protons, and contrast is enhanced by increasing the local inhomogeneities in the magnetic field: greater magnetic anisotropy leads to greater inhomogeneity and faster T_2 relaxation. Whilst cobalt enhances the magnetic anisotropy of the particles, manganese reduces it. Although it is possible that cobalt-containing SPIONs might have promising applications in medical imaging in the future, the potential toxicity if cobalt were to leach from the crystal structure means that it would have higher barriers than simply using iron to overcome.

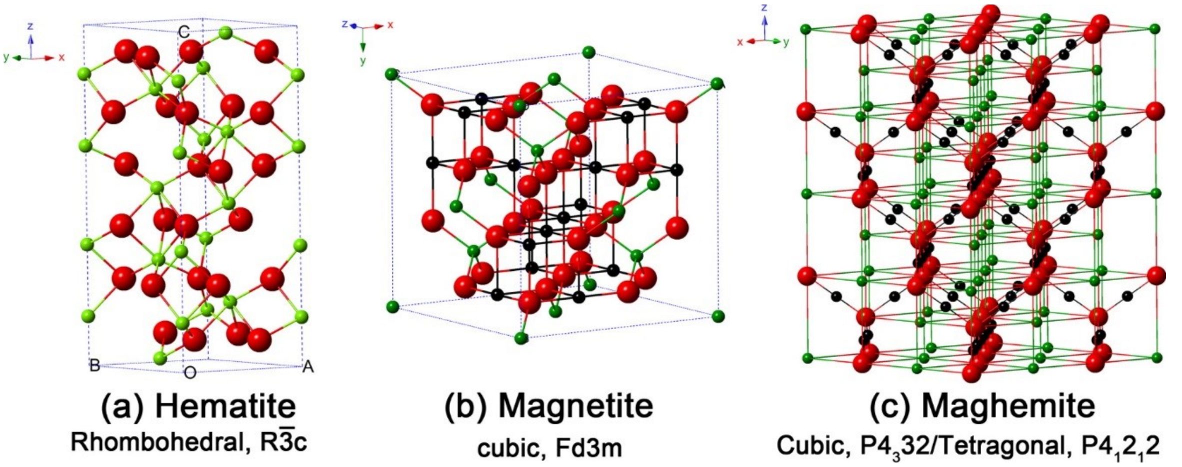

FIGURE 2.3: CRYSTAL STRUCTURE AND CRYSTALLOGRAPHIC DATA OF THE HEMATITE, MAGNETITE AND MAGHEMITE (THE BLACK BALL IS FE^{2+}, THE GREEN BALL IS FE^{3+} AND THE RED BALL IS O^{2-}) TAKEN FROM WU ET. AL.[27] AND USED UNDER CREATIVE COMMONS ATTRIBUTION 3.0 LICENCE.

Manganese is an interesting element because Mn(II) has a high spin state and is paramagnetic, although not as paramagnetic as Gd(III), with five unpaired electrons to gadolinium's seven (Figure 2.4). The majority of interest in manganese is as an alternative to gadolinium for T_1 contrast agents, particularly since manganese is a bio-compatible metal and has fewer toxicity concerns associated with it than gadolinium (although it is important to note that it is not completely non-toxic, and the brain and nervous system are particularly susceptible to overexposure)[28]. When used in a micellar contrast agent, Mn-doped SPIONs show very strong contrast[28]. Although manganese might therefore seem to be an obvious modification to the crystal structure, perhaps in the hope of developing a dual modal T_1- T_2 contrast agent, the experiments performed by Sun et. al.[26] do suggest this approach is unlikely to be fruitful.

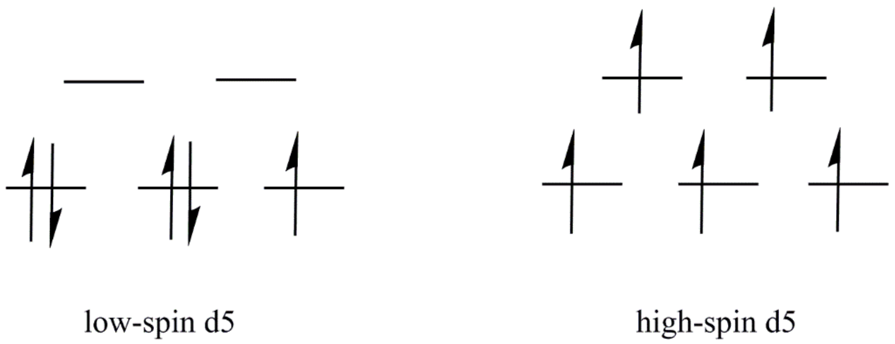

FIGURE 2.4: FIGURE ILLUSTRATING THE DIFFERENCE BETWEEN LOW AND HIGH SPIN D5 CONFIGURATIONS, SHOWING THE FIVE UNPAIRED ELECTRONS PRESENT IN MN2+.

Some dual modal T_1- T_2 MRI contrast agents have been developed, and many of these involve the addition of a gold coating to the surface of iron oxide nanoparticles[29]. The addition of a gold coating to the surface also opens up other imaging modalities besides MRI, including CT and OCT[30,31] which rely on high density to attenuate radiation and generate contrast in images. Given that OCT is currently the ‘gold standard’ for imaging atherosclerosis, the inclusion of a gold coating on the nanoparticles is something that may be interesting to investigate further. Other dual modal agents include SPIONs doped with Gd[32] and SPIONs coupled to Gd-containing chelates[33,34].

2.1.5 SURFACE LIGANDS/STABILISATION

For *in vivo* use, SPIONs are usually coated with some kind of biocompatible ligand[35,36]. This serves several purposes: i) it shields the iron oxide core from oxidation to prevent the loss of contrast activity; ii) it can mask the SPIONs from the immune system to increase circulation time[37–39]; iii) it allows opportunities for further functionalisation e.g. with dyes, labels, or targeting moieties[40]; iv) in some cases the coating itself can be used for targeting purposes[41–43]. These coatings affect the hydrodynamic size, and the surface charge of the particle and are the most easily modified aspect of a contrast agent.

Coatings can be monomeric or polymeric, and are often inspired by biological polymers. Common coatings include polyethyleneglycol (PEG)[20,44–49], citric acid[50], and dextran[35]. There are many ligand families available for coating SPIONs although some are used more commonly than others. Ligands which offer anchoring groups with an affinity for iron, and which are themselves water soluble, are usually capable of solubilising uncoated or hydrophobic SPIONs. Some ligand families include carboxylates, alcohols, thiols (commonly used with gold or gold-coated nanoparticles), phosphates, bisphosphonates, and sulfonates.

Nanoparticle surfaces can also be designed to be enzyme-sensing, most notably matrix metalloproteinases (MMPs)[51–54]. This has the potential to be particularly relevant to atherosclerosis images, where MMPs are upregulated in vulnerable plaque regions.

2.1.6 EFFECT OF SPIONS ON MACROPHAGES

The prospective imaging of atherosclerotic plaque, specifically vulnerable atherosclerotic plaque, with superparamagnetic iron oxide nanoparticles (SPIONs) raises some interesting questions on the effect of these nanoparticles on macrophage phenotype.

Work by Rojas et al. studied the effects of SPION treatment on M2 polarised macrophages[55] after demonstrating that polyethyleneimine-coated SPIONs designed for the magnetofection of material into cells had activating properties which could result in polarisation towards an M1 or inflammatory phenotype[56]. Given that poly ethyleneimine (PEI) is a common coating for SPIONs, and one which is under investigation as a part of this project, this aspect of SPION design is obviously one that will need careful consideration.

For the work performed as part of the study on M2 macrophages, Rojas et al. used several different coatings designed to vary in hydrodynamic size and surface charge. They looked at two differently-activated forms of M2 macrophages: IL-4 activated primary murine macrophages and human THP-1 cells differentiated into M2-like macrophages. The results of the study seemed to show a shift in phenotype, although the cells continued to express high levels of M2 associated proteins such as IL-10 and the conclusion was reached that SPION treatment alone did not result in re-polarisation towards an M1 phenotype. Although SPIONs were non-toxic at the levels tested in this study, it should also be considered that iron overload can result in M1 polarisation and so dose levels must be considered in terms of their likely inflammatory effects. This is an argument in support of maximising relaxivity to reduce the maximum dose needed in order to achieve good contrast.

AIMS OF THE CHAPTER

This chapter addresses the first two aims presented in section 1.4 of the thesis:

- To synthesise a range of superparamagnetic iron oxide nanoparticles, varying core size and surface ligands.
- To characterise those agents with respect to size, stability, surface charge, and relaxivity.

It discusses different approaches for the synthesis of SPIONs, and the selection of surface ligands for this project. It also presents the characterisation data and uses these data to draw conclusions regarding the best approach for further development of the contrast agent.

2.2 DISCUSSION OF NANOPARTICLE SYNTHESIS

SPIONs can be synthesised in multiple ways, however these approaches most commonly fall into the categories of co-precipitation of iron salts, or decomposition of iron salts. Decomposition can be achieved under a variety of conditions, but most frequently results from high temperatures. These can be reached using direct heating of the solution, or by sonication resulting in cavitation and high temperatures in specific regions.

A full list of approaches discussed in a thorough review by Laurent et al. includes co-precipitation, constrained environments, high-temperature reactions, sol-gel reactions, polyol methods, flow injection syntheses, electrochemical methods, aerosol/vapour methods and sonolysis[37]. Qiao et al. classify these methods as hydrolytic or as thermal decomposition in polar or non-polar solvents[39].

Co-precipitation of ferrous and ferric salts results in bulk production of nanoparticles which are often uncoated. Although it is possible to introduce synthetic control in a co-precipitation system by controlling pH, temperature, the ratio of reactants, the ionic strength of the reaction mixture, the rate of stirring and many other parameters, nanoparticles produced by co-precipitation tend to be more polydisperse than those produced by other methods. This difficulty in controlling synthetic parameters has led to the development of other approaches.

Thermal decomposition of iron-containing precursors tends to result in the production of monodisperse nanoparticles which are pre-capped with hydrophobic ligands resulting in a greater degree of stability for storage purposes. Iron acetylacetonates and oleates are commonly used precursors for this reaction, although a range of compounds are available[57–59].

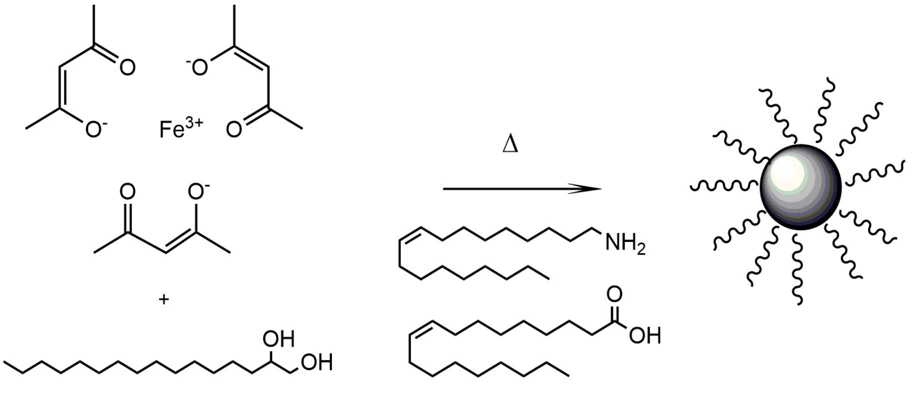

FIGURE 2.5: SYNTHETIC SCHEME SHOWING THERMAL DECOMPOSITION OF IRON ACETYLACETONATE FOR SPION FORMATION

In this research the decision was taken to follow a thermal decomposition approach using an iron acetylacetonate precursor as proposed by Sun et al.[58] (Figure 2.5) which generates monodisperse nanoparticles with the potential to tune size using a seed-mediated growth approach. Given that size is an important parameter for contrast agent design, the initial decision was to synthesise four different sizes of iron oxide core to examine whether the expected relationship between size and relaxivity could be observed. The core diameters were measured using Transmission Electron Microscopy (TEM).

Although many iron salts are suitable for thermal decomposition and some alternative routes use pure iron oleate, this route uses iron acetylacetonate as the iron source. The iron was heated in a high boiling point solvent with a reducing agent and a mixture of long-chain organic ligands, initially at 200 ˚C for decomposition of the salt, and then to 300 ˚C for nucleation and growth of the particles. The size was controlled by varying the duration of the growth phase. A photograph of the experimental set-up can be seen below (Figure 2.6).

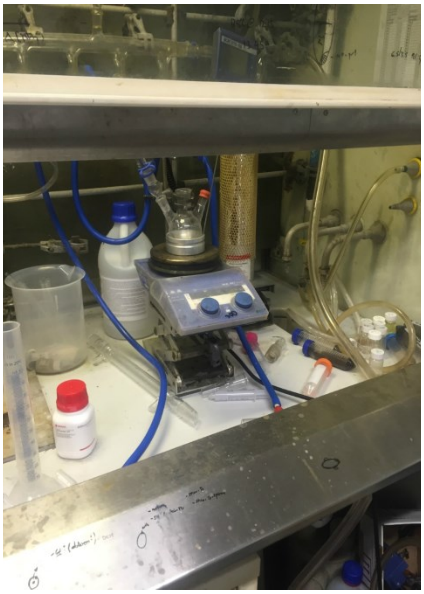

FIGURE 2.6: PHOTOGRAPH OF THE EXPERIMENTAL SET-UP FOR THE THERMAL DECOMPOSITION OF IRON ACETYLACETONATE UNDER NITROGEN.

The work-up of the particles was through centrifugation, first in ethanol to precipitate the hydrophobic particles out of the organic solvent, then in hexane for the removal of oversized particles and aggregates. The particles were then precipitated out of the organic phase again with ethanol and dried under vacuum. Unlike the experimental protocol in Sun et. al.[26] the particles were stored dry. The particles could be stored dry and used for functionalisation for several months, but after that aggregates formed which proved insoluble in a range of organic solvents even with sonication.

Given the intention to synthesise a range of core sizes, a comparison was undertaken early in the process to investigate whether it would be more efficient to submit the oversized cores removed in the hexane centrifugation step for a further growth, and those were compared to nanoparticles grown from the hexane supernatant. The oversized cores proved unsuitable for further growth, with a wide size dispersion which negated the advantage of thermal decomposition in that it generally provides a high level of control over particle size.

Very few modifications were made to the experimental protocol, however it was established that the addition of small volumes of the long-chain organic ligands to the work-up was unnecessary and could extend the retrieval process. Nanoparticles synthesised without the addition of oleylamine and oleic acid in the hexane resuspension step had entirely comparable behaviour to those with the extra addition of the ligand, but the addition of the ligands at that step often resulted in multiple centrifugations and a large excess of ethanol being required to precipitate the particles back out again.

2.3 EVALUATION OF TEM DATA

The sizes of the iron oxide cores were determined by Transmission Electron Microscopy (TEM). The measurements were taken in ImageJ and analysed in Excel (Figures 2.7 and 2.8). Three syntheses were performed and analysed, but in the 10 nm and 12 nm categories one datapoint was omitted in each case from the earliest synthesis. In the first nanoparticle synthesis, the particles taken forward for seed-mediated growth to 10 nm and 12 nm respectively were not from the solution phase during purification, but from the pellet of oversized particles removed by centrifugation with hexane. This resulted in average diameters being measured at 13 nm and 17 nm respectively, and much greater polydispersity in sizes, which did not correspond to later syntheses. This data has been excluded from the chart below (figure 2.8). Bearing in mind this variation in the approach to growth, and the consistency at the smaller size points, it seems reasonable to view this synthetic approach as being consistent. The increase in the standard deviation with size makes sense with the nature of the seed-mediated growth process, and the formation of further small nuclei at the 10 and 12 nm growth stages.

The TEM images recorded show the faceted nature of the seed-mediated growth process. This results in irregularly-shaped nanoparticles which leads to better T_2 contrast due to greater inhomogeneity in the magnetic field[5]. Another interesting observation from the images is the need for better size-selection at the 10 nm and 12 nm points (Figure 2.7). The nature of the seed-mediated growth process is that the conditions are identical to the initial synthesis. When growing to 10 nm and beyond, it is possible to observe novel, smaller cores in the TEM images which result in a bimodal size distribution when measured. In the 12 nm images, these cores are still present but have also correspondingly increased in size having undergone the seed-mediated growth process (Figure 2.7). This is not necessarily a weakness in the synthetic approach, but a method for separating the two populations of nanoparticle would be necessary if one of these sizes proves to have better magnetic properties for contrast agent behaviour.

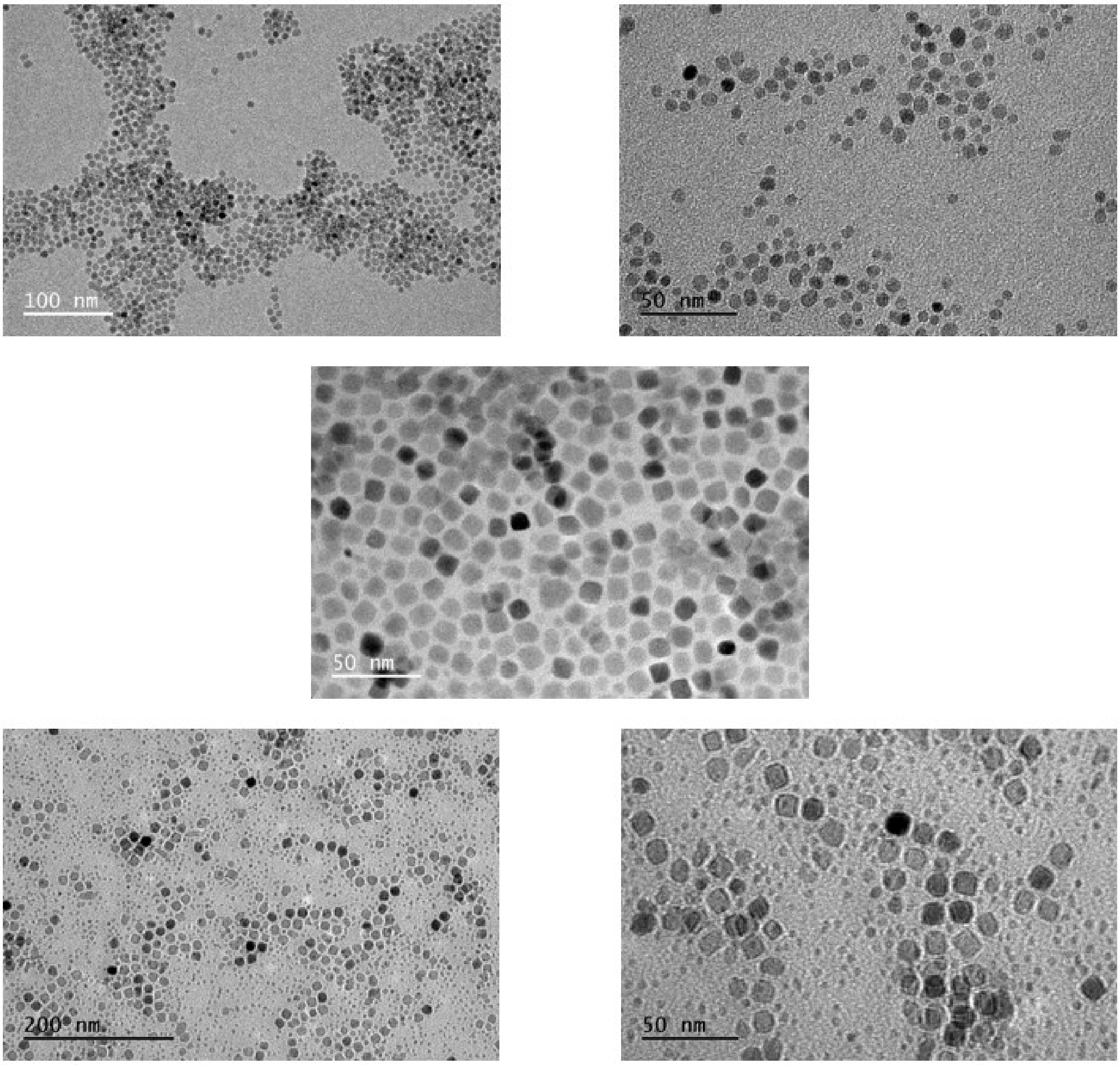

FIGURE 2.7: SELECTED EXAMPLES OF TEM IMAGES SHOWING THE IRON OXIDE CORES OF THE NANOPARTICLES. THE TOP TWO EXAMPLES ARE 6 NM CORES AT DIFFERENT MAGNIFICATION, 50K AND 80K RESPECTIVELY. THE MIDDLE IS 8 NM CORES AT 100K MAGNIFICATION, AFTER ONE GROWTH STAGE THE IRREGULAR FACETING RESULTING FROM THE SEED-MEDIATED GROWTH STRATEGY IS APPARENT[5]. THE BOTTOM ROW SHOWS TWO IMAGES OF 12 NM CORES AT 60K AND 100K MAGNIFICATION RESPECTIVELY. AT THE LARGER GROWTH STAGES THERE ARE TWO SIZE POPULATIONS VISIBLE IN TEM.

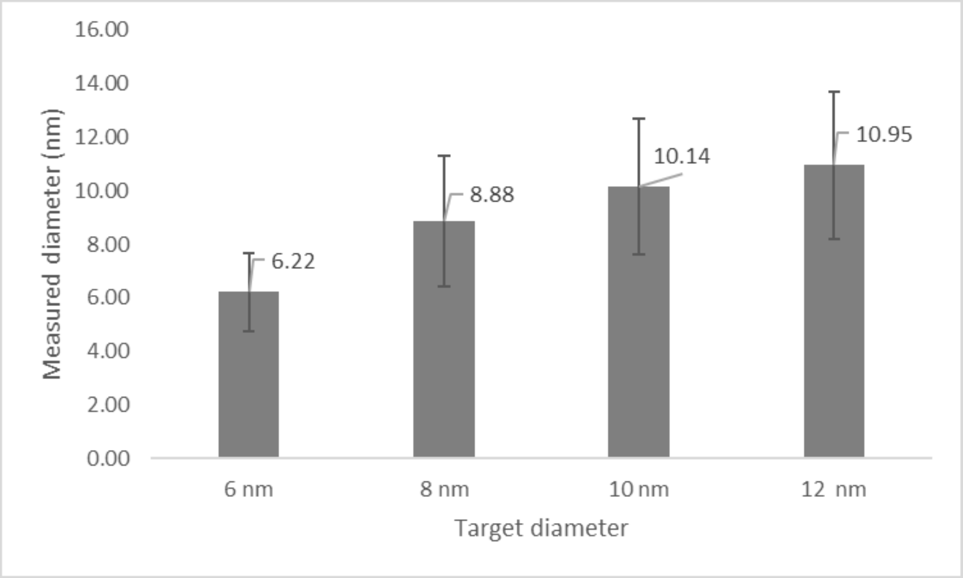

FIGURE 2.8: CHART SHOWING THE SIZE DISTRIBUTION OF NANOPARTICLE CORES SYNTHESISED VIA SEED-MEDIATED GROWTH. N = 2378, 1276, 1187, 1467 RESPECTIVELY. STANDARD DEVIATION FROM MEANS ARE: 1.45, 2.44, 2.55, 2.75 RESPECTIVELY. INCREASE OF STANDARD DEVIATION WITH PARTICLE SIZE MAKES SENSE, THOUGH AN INCREASED SAMPLE SIZE MAY REDUCE THE STANDARD DEVIATION FURTHER.

A paper by Rivas et al. suggested that the introduction of an additional centrifugation step improved monodispersity in a nanoparticle population[60]. It seemed likely that, given the size and mass difference of the two populations, centrifugation would be an appropriate method of size separation. This built on a step in the initial synthesis where overlarge nanoparticles were separated from the sample by centrifugation in hexane[58]. The Rivas paper[60] used an additional centrifugation step of 12 hours and the decision was taken to examine the effect of different centrifugation time on the mondispersity of the nanoparticles synthesised, following the method set forth by Sun et. al.[58]. It seemed possible that the disparity between the populations would be great enough for a shorter centrifugation to suffice. Unfortunately TEM measurements showed that these centrifugation steps of 1 and 3 hours respectively were not sufficient to differentiate the different size populations of nanoparticle cores. These results can be seen in figure 2.9.

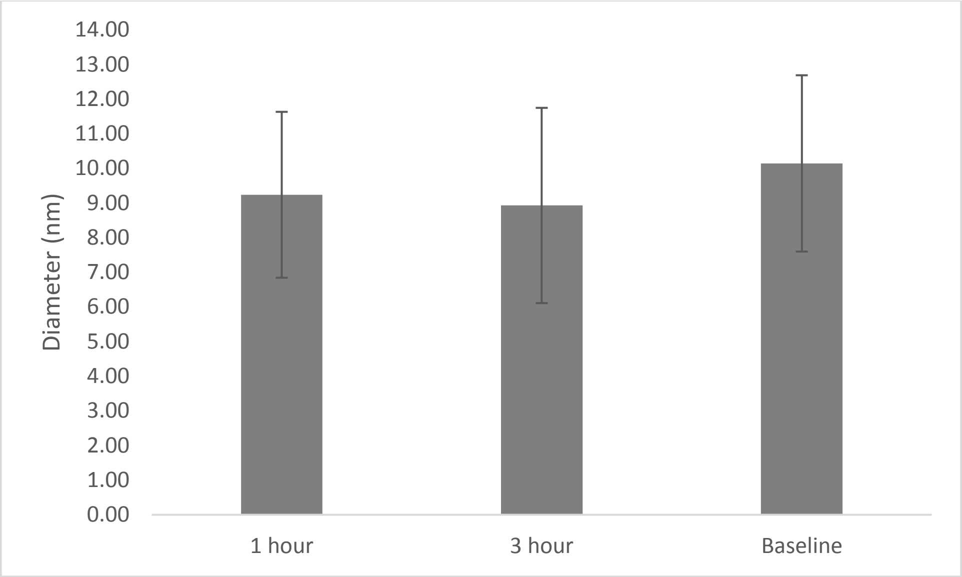

FIGURE 2.9: GRAPH SHOWING THE RESULTS OF CENTRIFUGATION TESTS FOR SIZE SEPARATION OF 10 NM NANOPARTICLE CORES AFTER 1 AND 3 HOURS RESPECTIVELY RELATIVE TO BASELINE (UNCENTRIFUGED). STANDARD DEVIATIONS: 2.39, 2.82, 2.55 RESPECTIVELY.

2.4 DISCUSSION OF NANOPARTICLE COATINGS

2.4.1 PMAO

Poly (maleic anhydride-alt-1-octadecene) is an interesting surface coating for the solubilisation of hydrophobic nanoparticles, which has not yet been widely used or explored. It offers an alternative to ligand exchange processes, which are often necessitated by the thermal decomposition approach to nanoparticle synthesis, instead relying on encapsulation of the particles.

The structure of the polymer is such that it has long hydrophobic tails, which intercalate with the long hydrophobic ligands installed on the nanoparticles during the synthetic process. The monomers are joined together by anhydride groups, which can be hydrolysed through acid or basic conditions to give carboxylic acids on the surface of the nanoparticle, resulting in water solubility. In the protocol used here, the process is achieved by 0.05 M NaOH in a phase-transfer process from a minimal amount of chloroform into the basic solution.

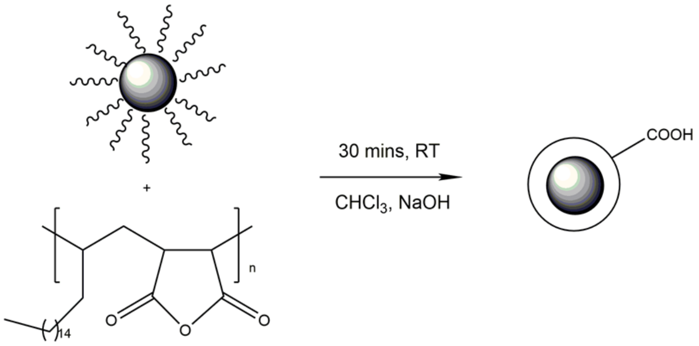

FIGURE 2.10: SYNTHETIC SCHEME SHOWING THE COATING PROTOCOL FOR POLY (MALEIC ANHYDRIDE-ALT-1-OCTADECENE)

As illustrated in figure 2.10, the ligand is first dissolved in chloroform, then the dry hydrophobic nanoparticles are added to the solution. The pale yellow solution then changes to a dark brown/black as the aggregated nanoparticles are dispersed in the chloroform. The mixture is stirred for 30 minutes, the chloroform is then removed and the residue re-suspended in a minimal amount of chloroform. Although the initial protocol suggested 2 ml, the hydrolysis of the anhydride groups is accelerated if the volume of chloroform is reduced. A volume of 0.05 M NaOH is then added, in the region of 10 ml, and the suspension agitated by hand and heated gently to 60 ˚C. The hydrolysis is a gradual process which can take in the region of 1 hour, occasionally longer. The further addition of base can accelerate the process, but it then extends the work-up, so there is a balance to be struck between the volume of base and the speed of the hydrolysis. There was no notable difference in the speed of hydrolysis between 0.05 M NaOH and 1 M KOH which was used for a comparison given its involvement in the alendronate ligand exchange process. Given the lack of benefit in using a stronger base, it is preferable to use the weaker solution, particularly for safety reasons.

The work-up for the PMAO-coated particles involved two filtration stages, one to remove undersized particles and one to remove large aggregates. The particles were retrieved from the base suspension by filtration on 50k mW centrifuge filter units, then re-suspended in smaller volumes of water. These aqueous suspensions were then filtered on 0.45 μm syringe filter units.

The PMAO coating is useful in that the process is faster than many other ligand exchange reactions, and it does not require the successful removal of the hydrophobic ligands for the particles to be hydrophilic. A roadblock to some ligand exchange processes is the difficulty in removing these surface ligands, which became evident in the cases of both the PEI and the alendronate used in this study. The PMAO-coating reaction also proved to be very reliable and replicable, over multiple reactions, only one batch was unsuccessful, and it is likely that this was due to some reagent contamination given that the same set of reactions performed the same way and the issue was not encountered again. It is perhaps the case that a mislabelled polymer salt was used in place of PMAO in that one event, but the precise error was unable to be identified.

Particles coated in PMAO appear to be stable in solution at room temperature for long periods of time (in excess of a year) by DLS and zeta potential measurements.

2.4.2 PEI

Polyethyleneimine is an amine-based polymer which is widely used in nanoparticle chemistry for the development of transfection agents for the intracellular delivery of materials such as DNA probes[61]. Although it is commonly used, extensive literature searches did not locate a protocol for the use of polyethyleneimine in a ligand exchange reaction, and so efforts were made to develop a protocol in house (Figure 2.11).

A range of conditions were tested, using varying pHs, reaction durations, and biphasic versus monophasic systems. Given that the majority of ligand exchange reactions including the alendronate protocol discussed in section 2.4.3 (Figure 2.12) use a basic pH, and that acidic pHs run the risk of oxidising or digesting the particles, reactions were performed at pH 8, pH 10, and pH 12 adjusted using a 1M KOH solution similarly to the alendronate protocol. The reactions were carried out over 24, 48, and 72 hours, the solvents were removed by magnetic decantation and washed with acetone. All conditions were tested in a biphasic THF/EtOH system and the variation of pH over a 48-hour period was also tested in a monophasic THF system, but without success or a notable difference in result. It seemed likely that one or more of these sets of conditions might result in the successful solubilisation of at least a proportion of the hydrophobic cores, but unfortunately this was not the case. These experiments are summarised in table 2.1 below.

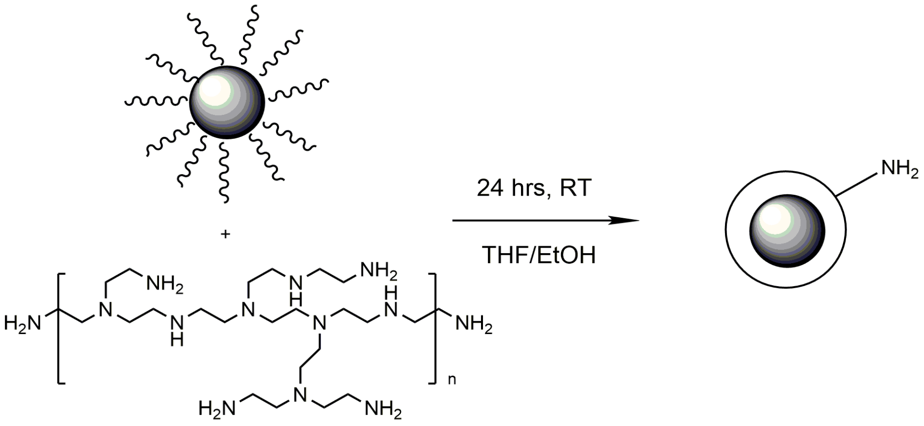

FIGURE 2.11: SYNTHETIC SCHEME SHOWING SAMPLE REACTION CONDITIONS FOR COATING WITH POLY (ETHYLENEIMINE)

TABLE 2.1: TABLE OF EXPERIMENTAL CONDITIONS FOR PEI COATING

pH	Reaction Time (hours)	System	Success?
8	24	THF/EtOH	No
10	24	THF/EtOH	No
12	24	THF/EtOH	No
8	48	THF/EtOH	No
10	48	THF/EtOH	No
12	48	THF/EtOH	No
8	72	THF/EtOH	No
10	72	THF/EtOH	No
12	72	THF/EtOH	No
8	48	THF	No
10	48	THF	No
12	48	THF	No

Although at first the particles seemed to form a stable dispersion, they precipitated out rapidly, and sonication was not sufficient to re-suspend them. Although ICP detects iron in the solutions, the inhomogeneity of the suspension meant that it was not appropriate to take the PEI-coated particles forward, and this was supported by further characterisation including DLS and zeta potential measurements. This suggests that although PEI may have useful applications in nanoparticle functionalisation, it does require a co-ligand in order to successfully functionalise nanoparticles.

2.4.3 ALENDRONATE

Alendronate is not widely used in contrast agent chemistry which is what made it interesting to explore in the first place. It is also a different class of ligand from the other two ligands under investigation, having a bisphosphonate group which has a strong affinity for the surface of the iron oxide rather than relying on electrostatic interaction or intercalation. This is also an alternative to PEG which is a very widely used ligand and which usually relies on carboxy or hydroxyl group affinity to the iron oxide surface, dependent upon the modifications the PEG chain has undergone.

Alendronate was selected as a potential surface coating because previous work in the group had identified it as promising[62], however, even using a protocol developed within the group[33] (Figure 2.12), some difficulties were encountered, most notably with stability. This could be due to the short chain on the ligand being insufficient to prevent aggregation of the particles. It could also be accounted for by difficulties in the ligand exchange process resulting in the long chain hydrophobic surface ligands not being fully removed.

Previous work had identified this ligand exchange as being pH sensitive, and some success was achieved by adjusting the pH of the solution prior to dissolving the alendronate ligand as opposed to adjusting the pH after the addition of the alendronate, but it is unclear thus far whether that was the deciding factor. The reaction conditions were tested multiple times but the success rate remained around 25%, despite no real variation in the approach. Other groups have synthesised PEGylated bisphosphonates based on alendronate and other similar molecules which have shown more consistency in their functionalisation of particles, as well as providing a good scaffold for further functionalisation such as labelling with fluorophores or targeting moieties[63].

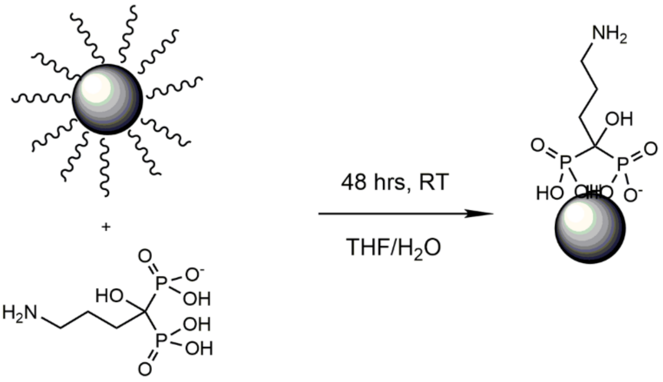

FIGURE 2.12: SYNTHETIC SCHEME SHOWING THE CONDITIONS FOR COATING WITH ALENDRONATE

2.5 EVALUATION OF DLS DATA

Dynamic Light Scattering (DLS) is a technique used to measure the size distribution of particles in suspension or solution. This gives a measure of the diameter of the nanoparticles taking into account the surface ligands, and the solvosphere around them when in solution. The surface ligands of the nanoparticles result in a larger diameter than can be measured simply from the iron oxide cores, particularly in the case of encapsulation such as with the PMAO polymer where the long chain hydrophobic surface ligands remain *in situ*. DLS can also give an idea of stability concerns such as aggregation. Hydrodynamic size plays a role in clearance[21], and the thickness of the ligand shell impacts the relaxivity of a contrast agent by changing the distance between water molecules and the inhomogeneities in the magnetic field originating from the iron oxide cores.

A selection of DLS plots comparing the different surface ligands and different core sizes of particle can be found below in figures 2.13, 2.14, and 2.15.

Alendronate showed large particle diameters relative to the core size, with the exception of the 8 nm cores. The 10 and 12 nm cores had diameters of 339 and 443 nm respectively, and relatively large standard deviations compared to PMAO-coated particles. Although they had low polydispersity indices (PDI), this is likely to be as a result of precipitation of the sample, rather than consistent particle sizes – a similar observation was made with the PEI-coated particles. Figure 2.14 shows evidence of large aggregates in the solution, particularly at the 10 and 12 nm core sizes.

PMAO produced by far the narrowest size dispersions measured on DLS, all values being below 200 nm. This is important for a long-circulating particle to avoid rapid clearance by the RES. Another important consideration in encapsulating particles in PMAO is ensuring the ratio of polymer to cores results in the encapsulation of single cores rather than aggregates or multiple cores. Although that might prove advantageous in terms of improving relaxivity, it would affect the ability to produce narrow size dispersions of well-controlled contrast agent which would be a prerequisite for any move towards clinical trials or manufacture meeting good manufacturing practice standards. The peak of hydrodynamic size at 10 nm (194.6 nm) might be indicative of two cores being encapsulated within the polymer. The PDI for the PMAO-coated particles indicates a mid-range dispersity, around 0.5. For pharmaceutical purposes a PDI <0.3 is preferred, so these are not ideal, but the larger particles have lower PDIs of 0.46. Although this is still too high, it is likely that the introduction of a further size-exclusion step could result in a final product which meets pharmaceutical standards.

PEI proved to be very challenging as a surface ligand, and it was impossible to measure hydrodynamic size for the 10 nm particles. The other sizes of particles were measured but as there was an increase in reported size with every repeat, it was evident that they were aggregating. This was further confirmed through visual inspection of the suspensions which indicated that they were not stable and precipitated out despite multiple attempts to optimise the coating conditions. Although the 6 nm and 8 nm cores have data which is superficially comparable to the PMAO-coated particles (148.5 and 113.2 nm respectively, and a similarity between the 8 nm at 206.5 nm with the larger PMAO-coated particles at 10 and 12 nm cores at 194.6 and 134.6 nm respectively), with much lower PDI (0.15 vs 0.51), this is likely to be an artefact of precipitation, and the lack of consistency in repeated measurements does not support the use of PEI as a coating going forward. Figure 2.16 shows evidence of some of the large aggregates detected by DLS, particularly at the 10 and 12 nm core sizes.

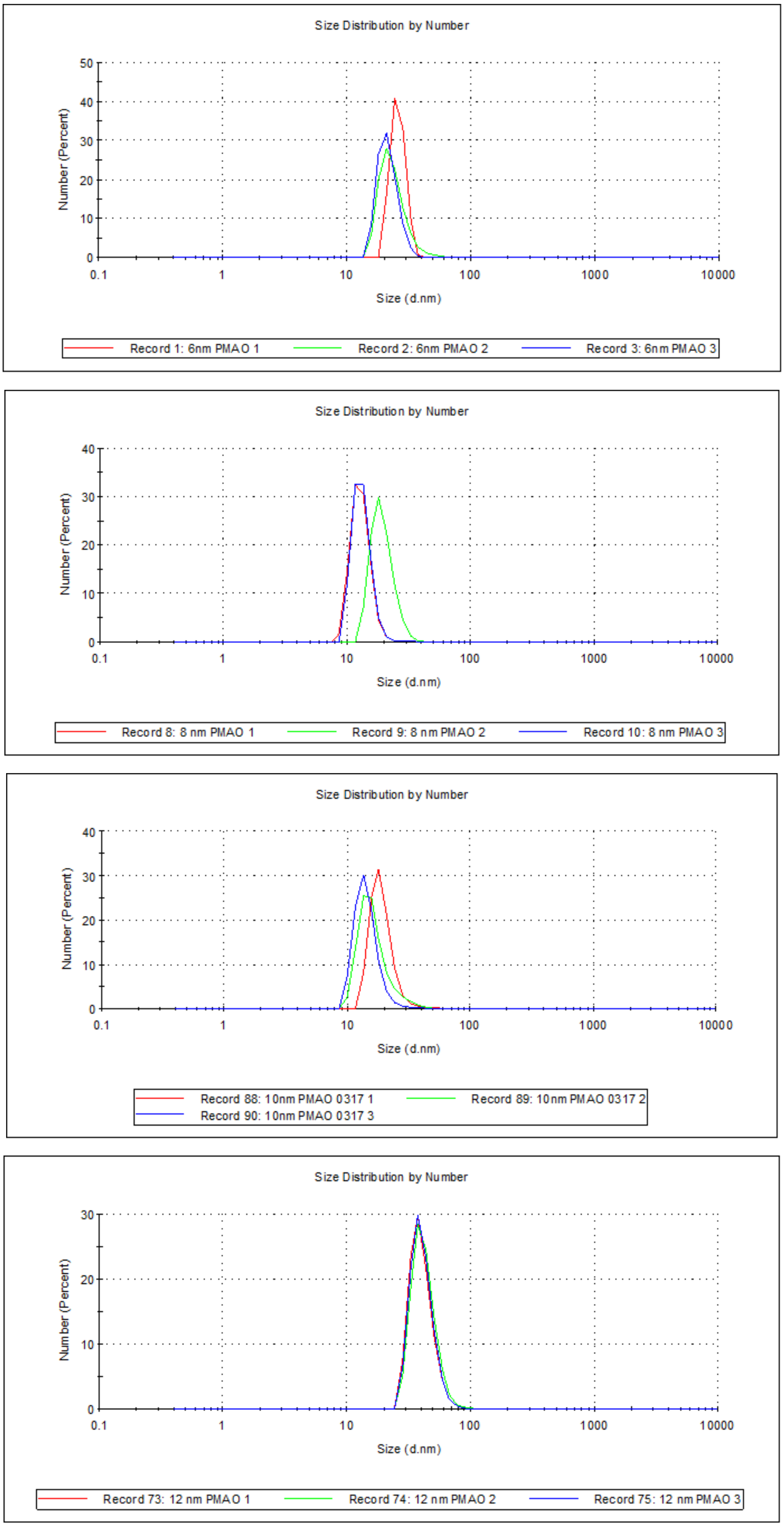

FIGURE 2.13: DLS PLOTS SHOWING DIZE DISTRIBUTION BY NUMBER OF 6, 8, 10, AND 12 NM CORES FUNCTIONALISED WITH PMAO

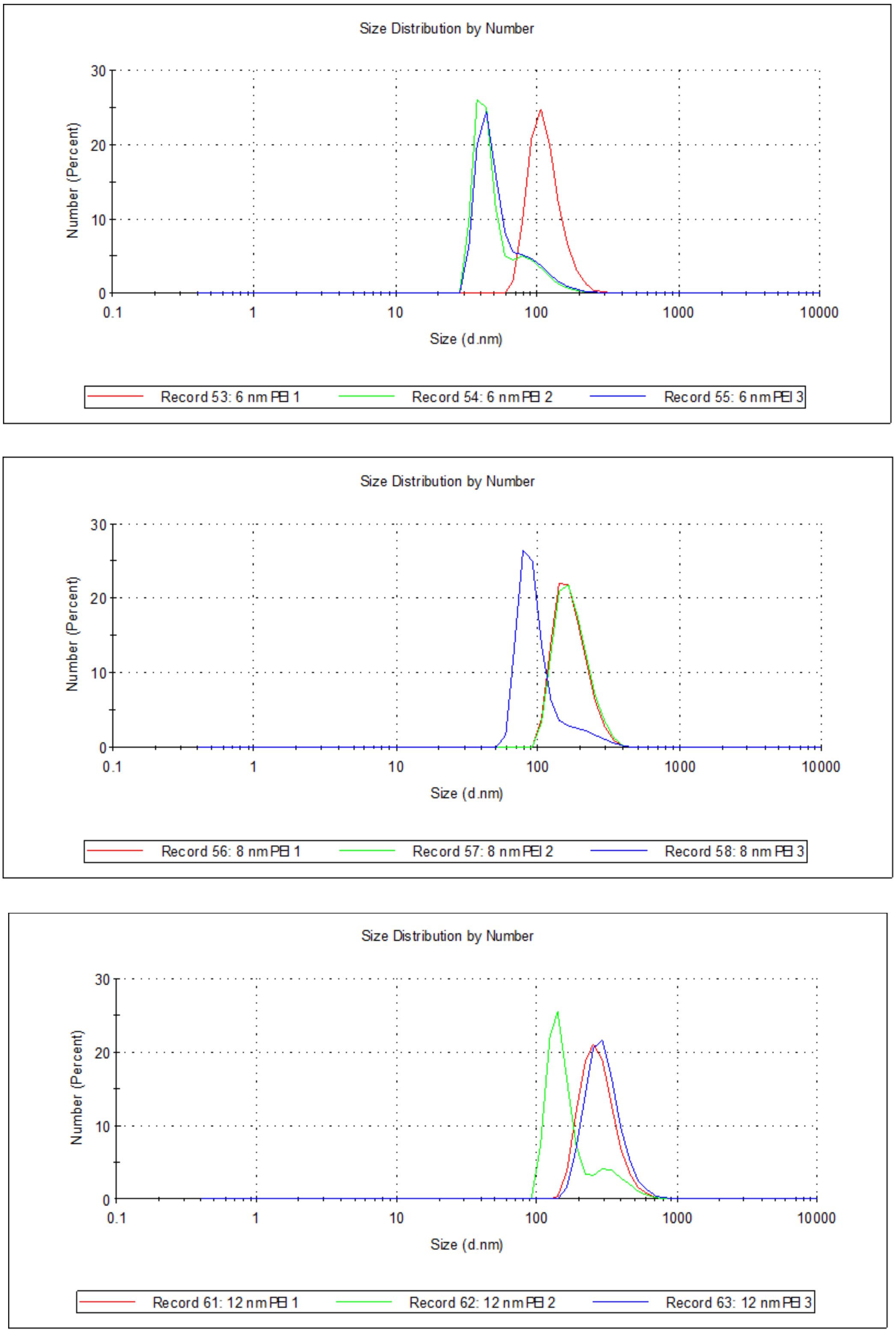

FIGURE 2.14: SIZE DISTRIBUTION PLOTS SHOWING 6, 8, AND 12 NM CORES FUNCTIONALISED WITH PEI. LARGE AGGREGATES ARE VISIBLE WITH LITTLE VARIATION BETWEEN CORE SIZE, SUGGESTING THAT THE LIGANDS ARE NOT INTERACTING WELL WITH THE NANOPARTICLE CORE SURFACE. THE 10 NM CORES WERE NOT ABLE TO BE MEASURED DUE TO PRECIPITATING OUT OF SOLUTION. IT WAS NOT POSSIBLE TO OBTAIN DATA FOR THOSE PARTICLES.

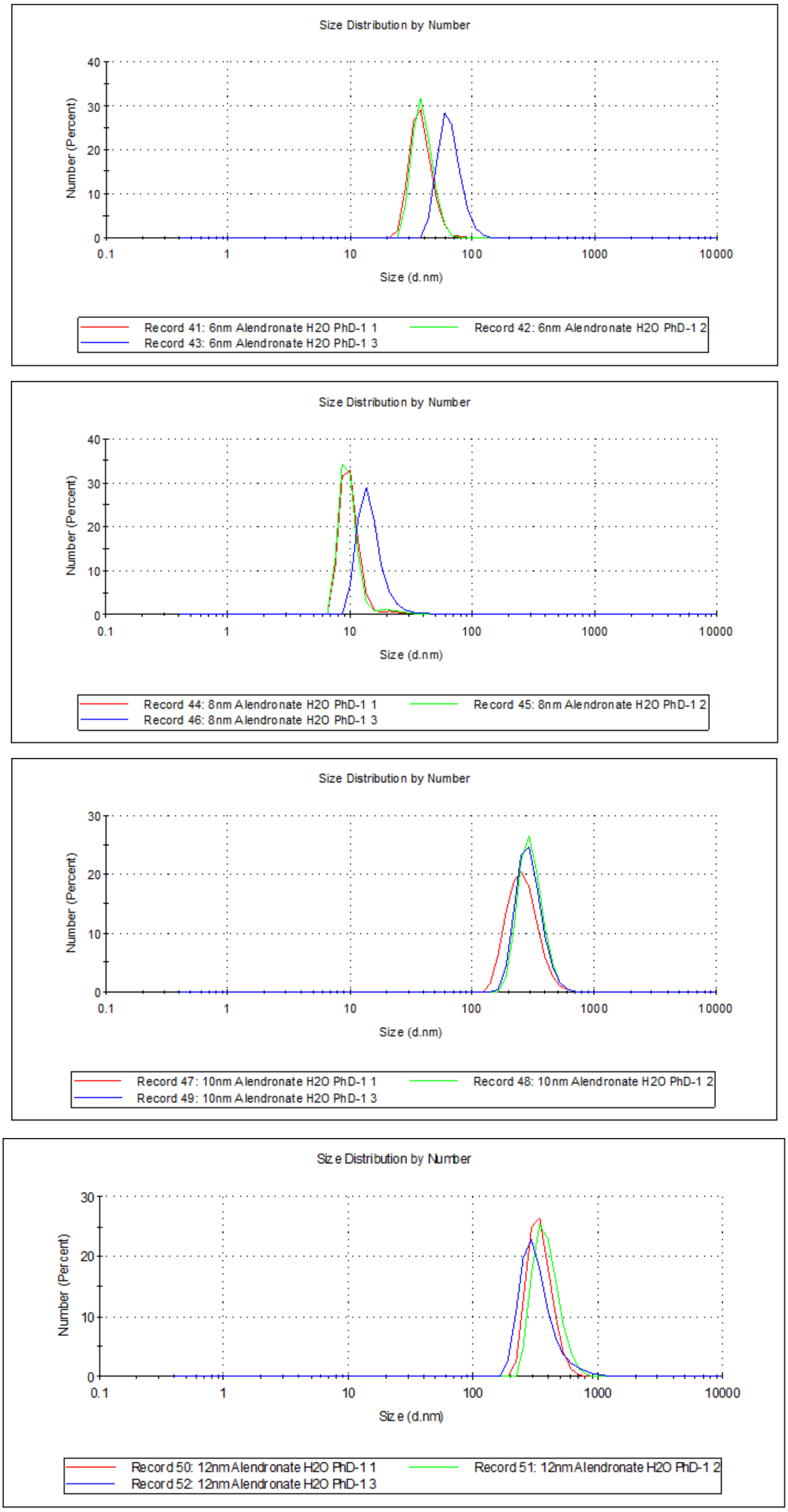

FIGURE 2.15: SIZE DISTRIBUTION BY NUMBER PLOTS FOR 6, 8. 10, AND 12 NM CORES FUNCTIONALISED WITH ALENDRONATE, SHOWING THE WIDE RANGE OF SIZES IRRESPECTIVE OF CORE SIZE AND THE FORMATION OF AGGREGATES ENCOUNTERED WITH THIS LIGAND.

TABLE 2.2: TABLE OF DLS DATA AS MEASURED ON A MALVERN UV ZETASIZER (DISTRIBUTION BY NUMBER, 3 REPRESENTATIVE RUNS, AVERAGED)

Sample	Diameter (nm)	Standard dev.	PDI
6 nm PMAO	113.2	1.91	0.51
8 nm PMAO	56.36	4.25	0.56
10 nm PMAO	194.6	4.73	0.46
12 nm PMAO	139.6	5.70	0.46
6 nm PEI	148.5	3.40	0.15
8 nm PEI	206.5	4.87	0.16
10 nm PEI	------	------	------
12 nm with PEI	371.5	4.16	0.23
6 nm alendronate	176.0	14.66	0.66
8 nm alendronate	58.2	1.27	0.43
10 nm alendronate	338.7	10.31	0.12
12 nm alendronate	443.2	19.59	0.20

Table 2.2 presents representative data for all twelve particles. The diameter is the Z-average. Although the PEI-coated particles seem to have narrow standard deviations and low polydispersity, I suspect this is due to the low concentration of the samples. The lack of success in the ligand exchange process did not result in stable suspensions of nanoparticles at any meaningful concentrations, and thus the samples themselves are unlikely to be representative. In the case of the 10 nm cores coated with PEI it was impossible to get any actual data. In terms of the other ligand systems, it is interesting to observe a decrease in measured diameter for the 8 nm cores relative to the others, however the size of the alendronate nanoparticles otherwise increases hugely with core diameter. Given the relatively small size of the ligand and the short chain, it is far more likely that these large diameters are the result of aggregation which was also observed visually. Although more possible with alendronate than PEI, it was challenging to reliably form a stable suspension, and the DLS graphs themselves show large aggregate peaks. PMAO on the other hand seems relatively consistent in size, and the variation is likely to result from the thickness of the polymer coating around the nanoparticle cores, with the possibility that the polymer might encapsulate multiple cores in a way which is unlikely to occur with the alendronate.

Overall DLS indicates that hydrodynamic sizes are suitable for a long-circulating probe, being too big for renal excretion (> 6 nm) and too small for immediate clearance through the RES (< 300 nm), and also demonstrates that of the three ligand systems under examination here, PMAO is the most stable suspension of nanoparticles and not prone to aggregation. It is also a reliable and easily replicable reaction, whereas the PEI reactions were not successful under a variety of conditions, and the alendronate coating reaction was variable in its hit rate without changing conditions. PMAO-coated particles were shown to be stable long-term on benchtop when stored in ambient conditions, with little to no aggregation or change in DLS or zeta potential over time.

2.6 EVALUATION OF ZETA POTENTIAL DATA

The surface charge of a contrast agent has a great impact on how it behaves *in vivo*. Neutral particles have the longest circulation times evading the immune system, because a surface charge results in a degree of opsonisation or coating by proteins in the blood which are attracted to the electrostatic charge, which can then result in phagocytosis and clearance[38]. Positively charged particles are cleared most rapidly from the blood, with the highest levels of cellular uptake and phagocytosis, therefore for a contrast agent designed to be long-circulating, a positive surface charge is not ideal[23,25]. The measured zeta potential values for all twelve nanoparticles can be found tabulated in table 2.3 below.

TABLE 2.3: ZETA POTENTIAL VALUES MEASURED AT 1 MM [FE] ON A BROOKHAVEN INSTRUMENTS CORPORATION ZETAPALS ANALYSER

Sample	Zeta Potential (mV)	Standard Error
6 nm PMAO	-42.11	0.95
8 nm PMAO	-36.66	0.60
10 nm PMAO	-36.21	1.40
12 nm PMAO	-22.84	1.69
6 nm PEI	3.30	1.26
8 nm PEI	1.60	1.24
10 nm PEI	10.91	0.56
12 nm PEI	5.73	0.42
6 nm Alendronate	26.86	2.22
8 nm Alendronate	12.12	0.42
10 nm Alendronate	26.60	0.95
12 nm Alendronate	28.44	0.82

PEI has a positive charge due to the surface amine groups, and is often used for transfection and intracellular delivery purposes. A positively charged surface results in greater cellular uptake through electrostatic attraction to the cell membrane, it also attracts opsonisation proteins in the blood which flag the agent for clearance[23,25,38]. This in tandem with the synthetic issues and the lack of stability means that PEI was deemed an inappropriate ligand to take forward in this study.

Interestingly the sodium alendronate coating also has a positive charge and this is again likely to be due to the surface amine groups. The slight aberration of the 8 nm charge appearing lower than the others which are all relatively consistent was due to the precipitation of that sample and reduced solubility compared to the other three sizes. It is also interesting that there was seemingly no trend in surface charge with size on the alendronate-coated particles.

Although it makes sense that the amine groups would result in a positively charged particle, this result is at odds with previous work within the group which identified alendronate as a potentially promising candidate[62]. That work measured alendronate coated particles as having the most negative surface charge of all ligands under investigation in that study. At present it is unclear how to account for this difference in findings, however it may be that the measured zeta potential is pH-dependent and related to the protonation of the amines.

The PMAO coating was looking most promising on the basis of DLS data. The negative surface charge confirmed that this was the most suitable of these three surface ligands to be taken forward, although the inverse trend in surface charge with size is interesting. This may arise from the same amount of polymer being used to solubilise the particles at every core size, meaning that larger particles had more spatial distribution of the carboxy groups resulting in the reduction of charge as size increases. The negative charge is not as ideal as a neutral surface coating, but it is a much better choice for an *in vivo* agent than a positively charged coating.

2.7 EVALUATION OF RELAXIVITY DATA

The relaxivity of an MR contrast agent is defined as the change in relaxation rate as a function of concentration. It corresponds to a measure of how ‘effective’ a contrast agent is. If the relaxivity of a contrast agent is high, then a lower concentration or a smaller dose of that contrast agent is required compared to other contrast agents.

When dealing with SPIONs, there is a relationship between size and relaxivity: relaxivity increases with size in a linear way. However, this only remains the case while the particles are still small enough to be superparamagnetic, although there seems to be some debate about where the threshold lies that marks the end of this relationship. Some sources that the relationship holds until the diameter reaches 20 nm[16], others say 30 nm[17] and some say 15 nm[18]. At very small sizes, the T_1 contrast (or r_1 relaxivity values) exceed the T_2, resulting in the SPIONs performing as T_1 contrast agents, causing a brightening[64]. T_2 relaxivity values tend to be larger than T_1 for SPIONs, and these values also tend to exceed T_1 relaxivities for T_1 contrast agents, meaning that SPIONs generate better contrast. Due to the contrast being negative (darkening of the area), SPIONs are not ideal for imaging in low-contrast or low-signal areas of the body. The r_2/r_1 ratio determines whether something is more effective as a T_1 or T_2 contrast agent. Very small SPIONs e.g. 3-5 nm have been shown to have a ratio low enough to be used as T_1 agents[16,20].

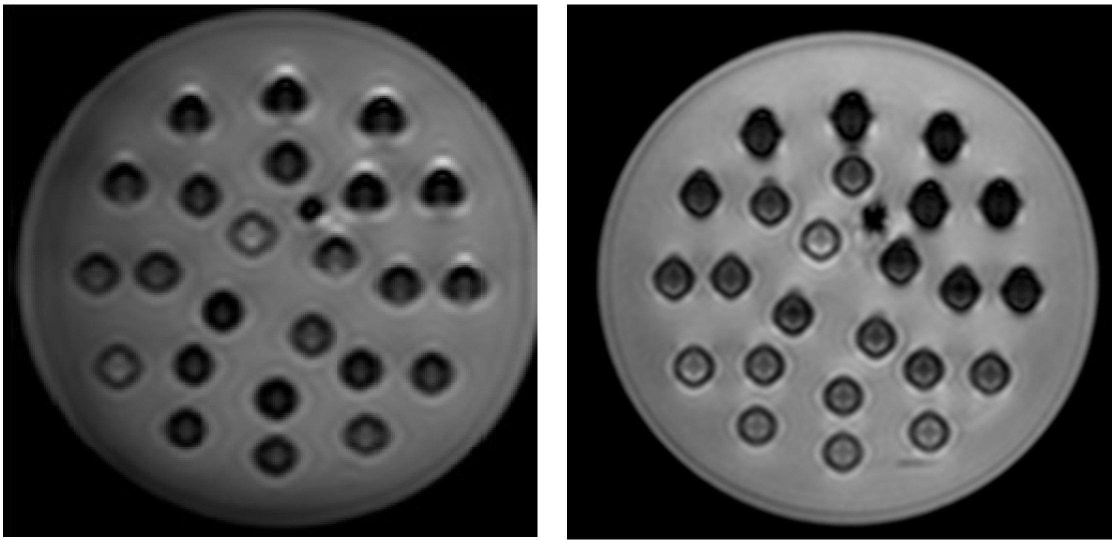

FIGURE 2.16: TWO MRI PHANTOM IMAGES OF IRON OXIDE NANOPARTICLES AT DIFFERENT DIAMETERS AND WITH DIFFERENT SURFACE COATINGS, AT A RANGE OF CONCENTRATIONS FOR THE CALCULATION OF RELAXIVITY VALUES, SHOWING A T_1 WEIGHTED SCAN (LEFT) AND A T_2* WEIGHTED SCAN (RIGHT) AT 3T.

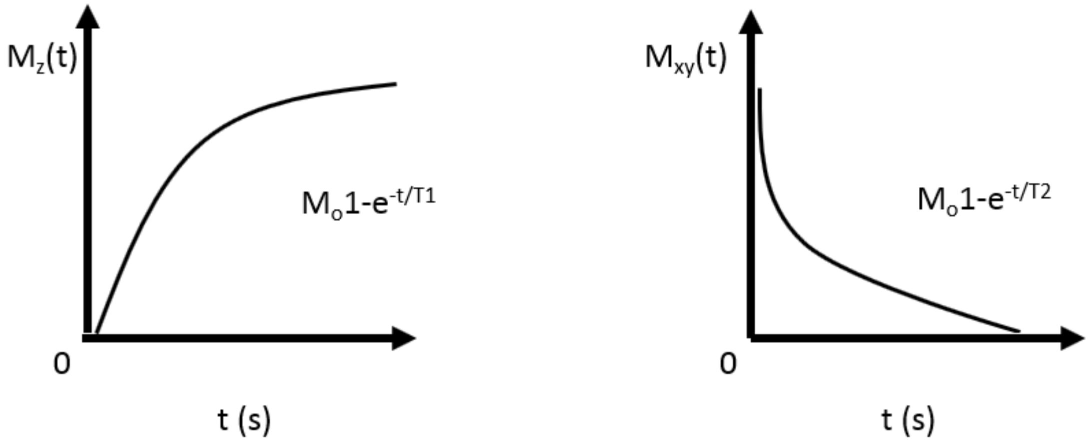

FIGURE 2.17: GRAPHS ILLUSTRATING THE RECOVERY OF LONGITUDINAL MAGNETISATION (T_1) AND TRANSVERSE MAGNETISATION (T_2), L AND R RESPECTIVELY. THESE EQUATIONS WERE USED FOR THE CALCULATIONS OF RELAXIVITY FROM PHANTOM MEASUREMENTS.

The relaxivity values for these nanoparticles were measured at ambient temperature on a Phillips 3T Achieva scanner. The ambient temperature was the same for all measurements, and the coil and phantom were identical. Examples of the phantom images which were then analysed in ImageJ, Matlab, and Excel, can be seen in figure 2.16. T_1, T_2 and T_2* weighted images were all analysed. The measured results are tabulated in table 4 below. The sequences used were T_1, T_2 and T_2* mapping sequences, and a 3D-MOLLI, and the relaxivity values were calculated by plotting $1/T_1$ or $1/T_2$ vs concentration. The T_1 and T_2 values were calculated from the phantom scans by using different inversion and echo times (three per phantom) to calculate the best fit equations seen in figure 2.17. Each particle was measured at 1 mM, 0.75 mM, 0.5 mM, and 0.25 mM with a water standard as 0, giving five points for the calculation of the relaxivity slope where r1 = R1/[Fe]. Each Eppendorf in the phantom was analysed individually. Example of relaxivity graphs calculating r_2 for PMAO coated particles can be seen in figure 2.18 below. A tabulation of the calculated relaxivities for all samples can be found in table 2.4.

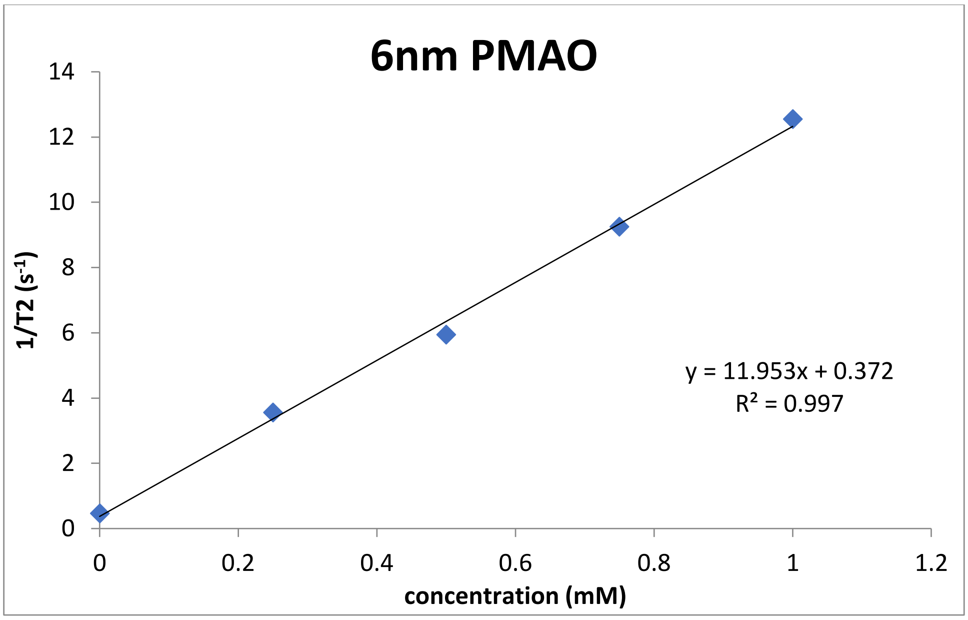

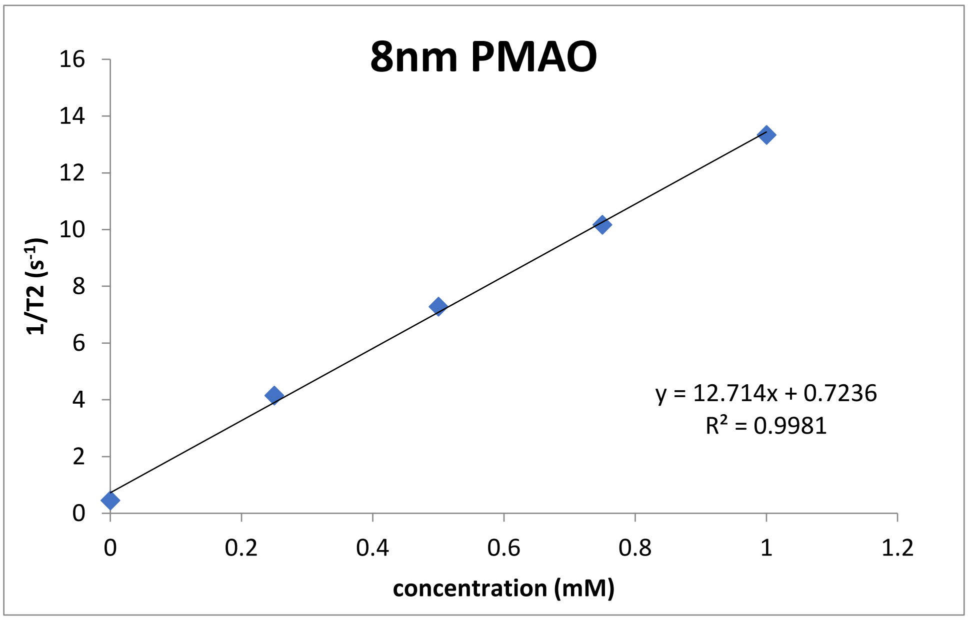

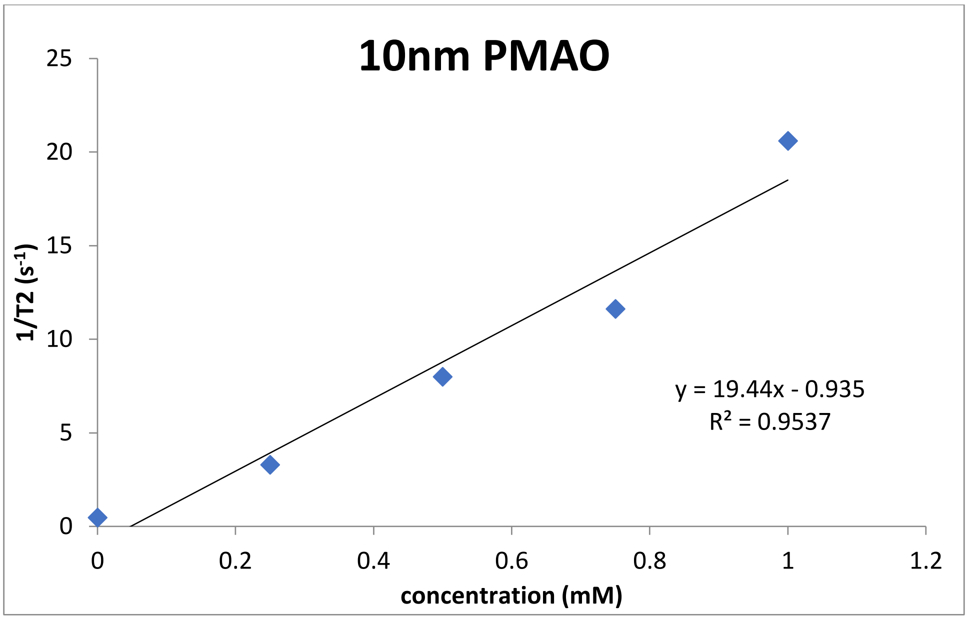

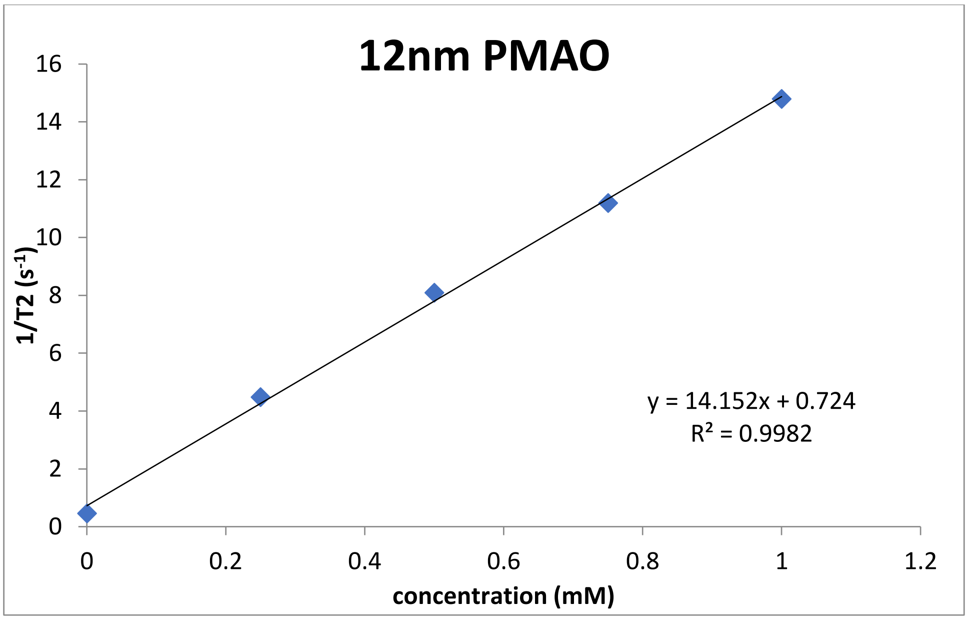

FIGURE 2.18: GRAPHS CALCULATING THE r_2 RELAXIVITY OF PMAO COATED PARTICLES BY PLOTTING $1/T_2$ AGAINST CONCENTRATION IN mM.

TABLE 2.4: RELAXIVITY VALUES OF IRON OXIDE NANOPARTICLES WITH DIFFERENT LIGAND SYSTEMS MEASURED ON 3T PHILLIPS ACHIEVA MRI SCANNER

Sample	r1/mM^{-1}s^{-1}	r2/mM^{-1}s^{-1}
6 nm PMAO	0.22	11.9
8 nm PMAO	0.25	12.2
10 nm PMAO	0.28	18.8
12 nm PMAO	0.32	14.0
6 nm PEI	0.39	36.1
8 nm PEI	0.14	5.2
10 nm PEI	----	0.53
12 nm PEI	----	3.7
6 nm alendronate	0.34	29.2
8 nm alendronate	3.00	3.6
10 nm alendronate	0.25	2.6
12 nm alendronate	----	0.69

As expected there is an increase in relaxivity with size, however it is known that relaxivity increases with size only to a point[16–18]. There seems to be a debate in the literature as to where the threshold is but the measurements here seem to suggest that threshold to be around 10-12 nm because there is a decrease in signal between these two rather than an increase. It may be that at higher temperatures (such as 37 ˚C) this relationship no longer holds true and it would be necessary to take measurements at higher temperature to confirm this. These measurements were carried out at 20 ˚C.

The high relaxivity measurements for the 6 nm PEI and Alendronate particles are unfortunately more likely to be due to aggregation and the presence of uncoated SPIONs in the solution. Visual inspection and measurement with the DLS both confirmed that these particles were not successfully solubilised – aggregates were present and it is unlikely that the ligand exchange took place. Uncoated SPIONs would be expected to have a higher relaxivity than coated ones. The failed coating reactions are also likely to explain the poor quality of data for these two ligands overall, with the notable exception of the 8 nm alendronate experiment which was successful (as confirmed by DLS).

The 8 nm alendronate particles are similar in relaxivity to the 8 nm PMAO coated particles which is encouraging for the consistency of data. The slightly higher value is likely to be due to the thinner shell of alendronate ligands when compared to the encapsulation by the PMAO polymer.

The relaxivity data supported the use of PMAO as a coating, not simply because of the greatly improved stability compared to the other systems under investigation but because the values are acceptable for a potential contrast agent. It is difficult to make comparisons to other licensed contrast agents due to the variation in magnetic field and temperature encountered in the literature and also the unfortunate variation in the literature as to whether r_2 refers to the change in T_2 signal or T_2* signal. Although T_2* would be more officially recorded as r_2*, literature description seems to be inconsistent. Here r_2 refers to the change in T_2* signal. Some T_2* data which was also measured for the nanoparticles was in the same region as data supplied in literature.

Relaxivity can also be affected by the core of the nanoparticle, e.g. by including other metals such as zinc or cobalt[58], and by the shape of the nanoparticle. Studies have shown that irregularly shaped nanoparticles rather than perfectly spherical SPIONs show enhanced relaxivities, because the irregular shape results in greater local field inhomogeneities which further reduce T_2[5]. The seed-mediated growth technique used to synthesise these SPIONs results in faceted structures as can be seen in Figure 2.7, meaning they are more effective than spherical particles of the same size[5]. Some work has suggested that shapes such as octapods may have even greater relaxivities than spheroid particles[8], and the effect of shapes such as nanorods would be interesting to examine further[7]

2.8 CONCLUSION

In conclusion, iron oxide nanoparticles are very promising candidates for use as MRI contrast agents. One of the advantages of using SPIONs is that they are almost infinitely customisable: it is possible to modify their properties from the most fundamental composition of the crystal structure, to their size, to the surface ligands which can predispose intracellular accumulation or mask the particles from the immune system. While it would be possible to attempt the optimisation of almost every parameter of nanoparticle design, it was necessary to narrow down the selection within the scope of the project, and so arguably the two most important parameters were selected for modification.

The effect of the surface ligand on *in vivo* SPION behaviour cannot be overestimated: it governs hydrodynamic size, zeta potential, and further functionalisation. All of these have an impact on targeting and circulation times which are particularly relevant when using an antibody to target a specific protein. In this project, three different surface ligands were tested and compared: one was selected for novelty, one was already widely used in *in vivo* nanoparticle studies, and one had been identified as promising as part of previous work in the group. Using a combination of DLS, zeta potential, and relaxivity data, the novel ligand was determined to be superior. The synthesis is simple, quick, and reliable, in addition to which the nanoparticles remain stable on the benchtop long-term.

It was also demonstrated that the seed-mediated growth approach proposed by Sun et al. does indeed result in different sizes of nanoparticle core, although the conditions do result in novel seed particles becoming visible at larger sizes if an appropriate separation method is not devised. A relationship between size and relaxivity was observed, although with the PMAO coating the peak occurs at 10 nm rather than 12 nm. This may have something to do with the PMAO coating method resulting in reduced anisotropy due to the thickness of the coating relative to the core at larger sizes.

After synthesising and comparing twelve different nanoparticles, one lead candidate was identified as a 10 nm particle with a PMAO surface coating, and this was confirmed by the repetition of experiments, particularly taking more relaxivity readings. The resulting hydrodynamic size of 30-40 nm also falls within the range which should maximise circulation time, being above both the 5 nm reported by Choi et. al.[21] and the 20 nm reported by Veiseh et. al.[36]. In this chapter, attempts were also made to optimise a ligand exchange between PEI and hydrophobic oleate surface ligands on pre-synthesised SPIONs, however these were unsuccessful.

2.9 EXPERIMENTAL

2.9.1 SYNTHESIS OF 6 NM HYDROPHOBIC SPIONS[58]

$Fe(acac)_3$ (0.71 g, 2 mmol) and 1,2-hexadecanediol (2.58 g, 10 mmol) were dissolved in benzyl ether (20 ml). Oleic acid (2.11 ml, 6 mmol) and oleylamine (2.80 ml, 6 mmol) were added, and the mixture was stirred for 2 hours under N_2 at 200 °C. The mixture was then heated to reflux (300 °C) for 1 hour and cooled by the removal of the heat source.

Nanoparticles were precipitated with EtOH (40 ml) and centrifuged for 30 minutes at 4000 rpm. Pellet was re-dispersed in hexane (20 ml) with the addition of oleic acid and oleylamine (50 µl), centrifuged for 10 minutes at 4000 rpm and then precipitated again with EtOH (20 ml). The solution was centrifuged for 30 minutes at 4000 rpm, supernatant removed and pellet dried under vacuum. SPIONs were stored dry.

2.9.2 SEED-MEDIATED GROWTH OF SPIONS[58]

$Fe(acac)_3$ (0.18 g, 0.5 mmol) and 1,2-hexadecanediol (0.65g, 2.5 mmol) were dissolved in benzyl ether (15 ml). Oleic acid (0.70 ml, 0.5 mmol), oleylamine (0.93 ml, 0.5 mmol) and SPIONs (5-10 mg) were added and the mixture was stirred for 1 hour at 200 °C. The mixture was then heated to reflux (300 °C) for half an hour and cooled by the removal of the heat source.

The workup was performed as with 6 nm hydrophobic SPIONs.

For centrifugation tests, post-growth from 8-10 nm workup was followed as per the original protocol[58] until the hexane centrifugation. At this point several aliquots were removed from the sample and centrifuged for 1, 2, or 3 hours. The supernatant was then removed because the purpose of the hexane centrifugation step is to remove undersized particles, leaving the correct size in the pellet. Samples were prepared for TEM from this pellet by dissolution in chloroform and spotting onto TEM sample grids, then analysed in ImageJ and Excel.

2.9.3 COATING WITH POLY(MALEIC ANHYDRIDE-ALT-1-OCTADECENE)[65]

Poly(maleic anhydride-alt-1-octadecene) (PMAO) (45 mg) was dissolved in $CHCl_3$ (20 ml). The SPIONs (2 mg) were added and mixture was stirred for 30 minutes. Chloroform was removed, and residue re-dissolved in a small amount of $CHCl_3$. NaOH (aq) (0.05 M) was added and mixture was heated at 60 °C until SPIONs transferred to the aqueous phase.

The solution was filtered using on a 0.45 µm filter, and then concentrated by centrifugation with a filter of 30k Mw. Particles were re-suspended in water and stored.

2.9.4 COATING WITH ALENDRONATE[33]

Sodium alendronate trihydrate (50 mg) was dissolved in water (5 ml) adjusted to pH 9 with 1 M KOH. The SPIONs (6 mg) were suspended in THF. The solutions were combined and stirred at room temperature for 2 days. The solution was magnetically decanted and washed with acetone (3x 10 ml). The particles were re-suspended in water and stored.

2.9.5 COATING WITH POLY (ETHYLENEIMINE)

Poly (ethyleneimine) (46.20 µl) was dissolved in EtOH (2 ml) and SPIONs (6 mg) were dissolved in THF (2 ml), pH was adjusted with 1 M KOH. Solutions were combined and stirred at room temperature for 2 days. Monophasic reactions were performed solely in THF.

The solution was magnetically decanted and washed with acetone (3x 10 ml). The particles were re-suspended in water and stored.

2.9.6 MRI PROTOCOLS FOR RELAXIVITY PHANTOMS

The nanoparticle phantom consisted of eppendorfs in a Perspex phantom, submerged in water. There was one blank tube with 1 ml of water, the rest contained 1 ml of each probe (6 nm PMAO, 6 nm PEI, etc.) at each of 0.25, 0.5, 0.75, and 1 mM [Fe]. Iron concentrations of the stock solutions were determined through ICP-MS measurements. The phantoms were scanned on a Phillips Achieva 3T Clinical Scanner at the Rayne Institute, and all measurements were received on a SENSE coil.

TSE T1 weighted scan:

Number of echoes: 1 Number of averages: 4

Repetition time/Echo time=515.820/5.387 ms, and flip angle=90°

T2 multi-echo scan:

Number of echoes: 4 Number of averages: 1

Repetition time/Echo time=380.146/56 ms, and flip angle=90°

T2* multi-echo scan:

Number of echoes: 1 Number of averages: 32

Repetition time/Echo time=10.771/3.1 ms, and flip angle=25°

2.9.7 PREPARATION OF FE SAMPLES FOR ICP-MS MEASUREMENT

40 µl of stock nanoparticle solution was digested with 160 µl of concentrated nitric acid for 48 hours. This volume was made up to 10 ml with deionised water and analysed by ICP-MS for Fe

concentration to determine the concentration of the stock. Measurements were performed on a PerkinElmer Optima 2000 DV ICP-OES Spectrometer.

2.10 REFERENCES

1 J. A. Champion and S. Mitragotri, *Proc. Natl. Acad. Sci. U. S. A.*, 2006, **103**, 4930–4.

2 E. A. Simone, T. D. Dziubla and V. R. Muzykantov, *Expert Opin. Drug Deliv.*, 2008, **5**, 1283–1300.

3 S. Muro, C. Garnacho, J. A. Champion, J. Leferovich, E. H. Schuchman, S. Mitragotri and V. R. Muzykantov, *Mol. Ther.*, 2008, **16**, 1450–1458.

4 P. Charoenphol, S. Mocherla, D. Bouis, K. Namdee, D. J. Pinsky and O. Eniola-Adefeso, *Atherosclerosis*, 2011, **217**, 364–370.

5 E. D. Smolensky, H. E. Park, Y. Zhou, G. A. Rolla, M. Marjańska, M. Botta and V. C. Pierre, *J. Mater. Chem. B*, 2013, **1**, 2818–2828.

6 S. Aktas, S. C. Thornton, C. Binns, L. Lari, A. Pratt, R. Kröger and M. A. Horsfield, *Mater. Res. Express*, 2015, **2**, 035002.

7 G. Wang, S. Inturi, N. J. Serkova, S. Merkulov, K. McCrae, S. E. Russek, N. K. Banda and D. Simberg, *ACS Nano*, 2014, **8**, 12437–12449.

8 Z. Zhao, Z. Zhou, J. Bao, Z. Wang, J. Hu, X. Chi, K. Ni, R. Wang, X. Chen, Z. Chen and J. Gao, *Nat. Commun.*, 2013, **4**, 2266.

9 Z. T. Shen, S. Zheng, M. J. Gounis and A. B. Sigalov, *PLoS One*, 2015, **10**, e0143453.

10 G. S. van Bochove, H. M. H. F. Sanders, M. de Smet, H. M. Keizer, W. J. M. Mulder, R. Krams, G. J. Strijkers and K. Nicolay, *Eur. J. Inorg. Chem.*, 2012, **2012**, 2115–2125.

11 V. Amirbekian, M. J. Lipinski, K. C. Briley-Saebo, S. Amirbekian, J. G. S. Aguinaldo, D. B. Weinreb, E. Vucic, J. C. Frias, F. Hyafil, V. Mani, E. A. Fisher and Z. A. Fayad, *Proc. Natl. Acad. Sci. U. S. A.*, 2007, **104**, 961–966.

12 M. E. Lobatto, C. Calcagno, A. Millon, M. L. Senders, F. Fay, P. M. Robson, S. Ramachandran, T. Binderup, M. P. M. Paridaans, S. Sensarn, S. Rogalla, R. E. Gordon, L. Cardoso, G. Storm, J. M. Metselaar, C. H. Contag, E. S. G. Stroes, Z. A. Fayad and W. J. M. Mulder, *ACS Nano*, 2015, **9**, 1837–1847.

13 G. S. Van Bochove, L. E. M. M. Paulis, D. Segers, W. J. M. M. Mulder, R. Krams, K. Nicolay and G. J. Strijkers, *Contrast Media Mol. Imaging*, 2011, **6**, 35–45.

14 S. Meier, G. Pütz, U. Massing, C. E. Hagemeyer, D. von Elverfeldt, M. Meißner, K. Ardipradja,

S. Barnert, K. Peter, C. Bode, R. Schubert and C. von zur Muhlen, *Biomaterials*, 2015, **53**, 137–148.

15 A. G. Roca, L. Gutiérrez, H. Gavilán, M. E. Fortes Brollo, S. Veintemillas-Verdaguer and M. del P. Morales, *Adv. Drug Deliv. Rev.*, 2019, **138**, 68–104.

16 D. Ling, N. Lee and T. Hyeon, *Acc. Chem. Res.*, 2015, **48**, 1276–1285.

17 G. Kandasamy and D. Maity, *Int. J. Pharm.*, 2015, **496**, 191–218.

18 F. Assa, H. Jafarizadeh-Malmiri, H. Ajamein, N. Anarjan, H. Vaghari, Z. Sayyar and A. Berenjian, *Nano Res.*, 2016, **9**, 2203–2225.

19 B. Issa and I. M. Obaidat, in *Magnetic Resonance Imaging*, ed. L. Manchev, Intech, 2019.

20 U. I. Tromsdorf, O. T. Bruns, S. C. Salmen, U. Beisiegel and H. Weller, *Nano Lett.*, 2009, **9**, 4434–4440.

21 H. S. Choi, W. Liu, P. Misra, W. Tanaka, J. P. Zimmer, B. I. Ipe, M. G. Bawendi and J. V. Frangioni, *Nat. Biotechnol.*, 2007, **25**, 1165–1170.

22 V. Gulani, F. Calamante, F. G. Shellock, E. Kanal and S. B. Reeder, *Lancet Neurol.*, 2017, **16**, 564–570.

23 A. Albanese, P. S. Tang and W. C. W. Chan, *Annu. Rev. Biomed. Eng.*, 2012, **14**, 1–16.

24 K. Ulbrich, K. Holá, V. Šubr, A. Bakandritsos, J. Tuček and R. Zbořil, *Chem. Rev.*, 2016, **116**, 5338–5431.

25 E. Blanco, H. Shen and M. Ferrari, *Nat. Biotechnol.*, 2015, **33**, 941–951.

26 S. Sun, H. Zeng, D. B. Robinson, S. Raoux, P. M. Rice, S. X. Wang and G. Li, *J. Am. Chem. Soc.*, 2004, **126**, 273–279.

27 W. Wu, Z. Wu, T. Yu, C. Jiang and W.-S. Kim, *Sci. Technol. Adv. Mater.*, 2015, **16**, 023501.

28 D. Pan, S. D. Caruthers, A. Senpan, A. H. Schmieder, S. A. Wickline and G. M. Lanza, *Wiley Interdiscip. Rev. Nanomedicine Nanobiotechnology*, 2011, **3**, 162–173.

29 S. J. Cho, B. R. Jarrett, A. Y. Louie and S. M. Kauzlarich, *Nanotechnology*, 2006, **17**, 640–644.

30 M. M. Van Schooneveld, D. P. Cormode, R. Koole, J. T. Van Wijngaarden, C. Calcagno, T. Skajaa, J. Hilhorst, D. C. 'T Hart, Z. A. Fayad, W. J. M. Mulder and A. Meijerink, *Contrast Media Mol. Imaging*, 2010, **5**, 231–236.

31 A. de la Zerda, S. Prabhulkar, V. L. Perez, M. Ruggeri, A. S. Paranjape, F. Habte, S. S. Gambhir and R. M. Awdeh, *Clin. Experiment. Ophthalmol.*, 2015, **43**, 358–366.

32 Z. Zhou, D. Huang, J. Bao, Q. Chen, G. Liu, Z. Chen, X. Chen and J. Gao, *Adv. Mater.*, 2012, **24**, 6223–6228.

33 N. A. Keasberry, M. Bañobre-López, C. Wood, G. J. Stasiuk, J. Gallo and N. J. Long, *Nanoscale*, 2015, **7**, 16119–16128.

34 A. Szpak, S. Fiejdasz, W. Prendota, T. Strączek, C. Kapusta, J. Szmyd, M. Nowakowska and S. Zapotoczny, *J. Nanoparticle Res.*, 2014, **16**, 1–11.

35 E. Tombácz, R. Turcu, V. Socoliuc and L. Vékás, *Biochem. Biophys. Res. Commun.*, 2015, **468**, 442–453.

36 O. Veiseh, J. Gunn and M. Zhang, *Adv. Drug Deliv. Rev.*, 2011, **62**, 284–304.

37 S. Laurent, D. Forge, M. Port, A. Roch, C. Robic, L. Vander Elst and R. N. Muller, *Chem. Rev.*, 2008, **108**, 2064–110.

38 K. Hola, Z. Markova, G. Zoppellaro, J. Tucek and R. Zboril, *Biotechnol. Adv.*, 2015, **33**, 1162–1176.

39 R. Qiao, C. Yang and M. Gao, *J. Mater. Chem.*, 2009, **19**, 6274.

40 G. A. F. van Tilborg, E. Vucic, G. J. Strijkers, D. P. Cormode, V. Mani, T. Skajaa, C. P. M. Reutelingsperger, Z. A. Fayad, W. J. M. Mulder and K. Nicolay, *Bioconjug. Chem.*, 2010, **21**, 1794–1803.

41 C. Tu, T. S. C. Ng, H. K. Sohi, H. A. Palko, A. House, R. E. Jacobs and A. Y. Louie, *Biomaterials*, 2011, **32**, 7209–7216.

42 H. Vu-Quang, M. Muthiah, Y. K. Kim, C. S. Cho, R. Namgung, W. J. Kim, J. H. Rhee, S. H. Kang, S. Y. Jun, Y. J. Choi, Y. Y. Jeong and I. K. Park, *Carbohydr. Polym.*, 2012, **88**, 780–788.

43 H. Vu-Quang, M. Muthiah, H. J. Lee, Y. K. Kim, J. H. Rhee, J. H. Lee, C. S. Cho, Y. J. Choi, Y. Y. Jeong and I. K. Park, *Carbohydr. Polym.*, 2012, **87**, 1159–1168.

44 A. Kolate, D. Baradia, S. Patil, I. Vhora, G. Kore and A. Misra, *J. Control. Release*, 2014, **192**, 67–81.

45 Y. C. Park, J. B. Smith, T. Pham, R. D. Whitaker, C. A. Sucato, J. A. Hamilton, E. Bartolak-Suki and J. Y. Wong, *Colloids Surfaces B Biointerfaces*, 2014, **119**, 106–114.

46 A. Mukhopadhyay, N. Joshi, K. Chattopadhyay and G. De, *ACS Appl. Mater. Interfaces*, 2012, **4**, 142–149.

47 J. S. Suk, Q. Xu, N. Kim, J. Hanes and L. M. Ensign, *Adv. Drug Deliv. Rev.*, 2016, **99**, 28–51.

48 L. Song, F. Zang, M. Song, G. Chen, Y. Zhang and N. Gu., *J. Nanosci. Nanotechnol.*, 2015, **15**, 4111–4118.

49 L. Rao, J.-H. Xu, B. Cai, H. Liu, M. Li, Y. Jia, L. Xiao, S.-S. Guo, W. Liu and X.-Z. Zhao, *Nanotechnology*, 2016, **27**, 085106.

50 L. Li, K. Y. Mak, C. W. Leung, K. Y. Chan, W. K. Chan, W. Zhong and P. W. T. Pong, *Microelectron. Eng.*, 2013, **110**, 329–334.

51 P. S. Kulkarni, M. K. Haldar, R. R. Nahire, P. Katti, A. H. Ambre, W. W. Muhonen, J. B. Shabb, S. K. R. Padi, R. K. Singh, P. P. Borowicz, D. K. Shrivastava, K. S. Katti, K. Reindl, B. Guo and S. Mallik, *Mol. Pharm.*, 2014, **11**, 2390–2399.

52 Y. Il Park, E. Kim, C. Huang, K. S. Park, C. M. Castro, H. Lee and R. Weissleder, *Bioconjug. Chem.*, 2016, **28**, 33–37.

53 J. Gallo, N. Kamaly, I. Lavdas, E. Stevens, Q. De Nguyen, M. Wylezinska-Arridge, E. O. Aboagye and N. J. Long, *Angew. Chemie - Int. Ed.*, 2014, **53**, 9550–9554.

54 Y. Wang, P. Shen, C. Li, Y. Wang and Z. Liu, *Anal. Chem.*, 2012, **84**, 1466–1473.

55 J. M. Rojas, L. Sanz-Ortega, V. Mulens-Arias, L. Gutiérrez, S. Pérez-Yagüe and D. F. Barber, *Nanomedicine Nanotechnology, Biol. Med.*, 2016, **12**, 1127–1138.

56 V. Mulens-Arias, J. M. Rojas, S. Pérez-Yagüe, M. P. Morales and D. F. Barber, *Biomaterials*, 2015, **52**, 494–506.

57 L. Zhang, W.-F. Dong and H.-B. Sun, *Nanoscale*, 2013, **5**, 7664–84.

58 S. Sun, H. Zeng, D. B. Robinson, S. Raoux, P. M. Rice, S. X. Wang, G. Li, S. X. Wand and G. Li, *J. Am. Chem. Soc.*, 2004, **126**, 273–279.

59 J. Park, K. An, Y. Hwang, J.-G. Park, H.-J. Noh, J.-Y. Kim, J.-H. Park, N.-M. Hwang and T. Hyeon, *Nat. Mater.*, 2004, **3**, 891–895.

60 N. Guldris, B. Argibay, Y. V. Kolen’ko, E. Carbó-Argibay, T. Sobrino, F. Campos, L. M. Salonen, M. Bañobre-López, J. Castillo and J. Rivas, *J. Colloid Interface Sci.*, 2016, **472**, 229–236.

61 J. Duan, J. Dong, T. Zhang, Z. Su, J. Ding, Y. Zhang and X. Mao, *Nanomedicine*, 2013, **9**, 789–

801.

62 R. Sabra, J. P. Gallo, T. Homma, N. Long and R. Krams, MRes thesis, Imperial College London, 2013.

63 L. Sandiford, A. Phinikaridou, A. Protti, L. K. Meszaros, X. Cui, Y. Yan, G. Frodsham, P. A. Williamson, N. Gaddum, R. M. Botnar, P. J. Blower, M. A. Green and R. T. M. De Rosales, *ACS Nano*, 2013, **7**, 500–512.

64 M. Suzuki, L. Bachelet-Violette, F. Rouzet, A. Beilvert, G. Autret, M. Maire, C. Menager, L. Louedec, C. Choqueux, P. Saboural, O. Haddad, C. Chauvierre, F. Chaubet, J.-B. Michel, J.-M. Serfaty and D. Letourneur, *Nanomedicine (Lond).*, 2015, **10**, 73–87.

65 M. Moros, B. Pelaz, P. López-Larrubia, M. L. García-Martin, V. Grazú and J. M. de la Fuente, *Nanoscale*, 2010, **2**, 1746–1755.

Chapter 3

Biological Evaluation of Contrast Agents

3.1 INTRODUCTION

3.1.1 ANTIBODIES AND THEIR USE FOR TARGETING

Antibodies (Ab), also known as immunoglobulins (Ig), are large glycoproteins of about 150 kDa produced by the immune system for the identification and neutralisation of pathogens. They bind to antigens (Ag), which are molecules capable of binding to Ag-specific receptors, but which are not necessarily capable of provoking an immune response on their own. The original definition of an antigen, and the definition still used in immunology, is stricter and only applies to molecules capable of binding to antibodies and provoking an immune response. That definition was widened to any molecule which could be recognised by the adaptive immune system, thus it is possible for something to be an antigen without being an immunogen. Antigens can be many classes of molecules including polysaccharides, proteins, and peptide chains. When modified by or combined with proteins or sugars, lipids and nucleic acids can also behave as antigens.

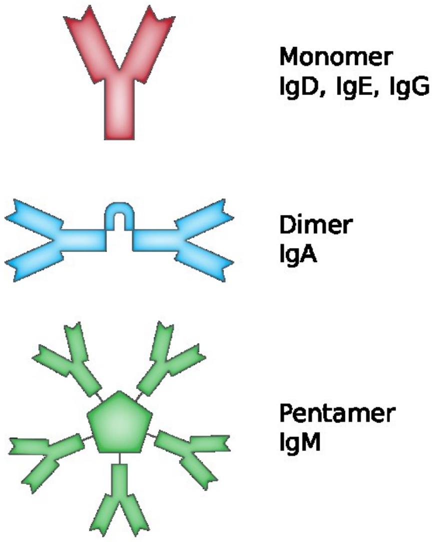

FIGURE 3.1: FIGURE SHOWING THE MONOMERIC, DIMERIC, AND PENTAMERIC STRUCTURES OF IMMUNOGLOBULIN (MARTIN BRÄNDLI, USED UNDER CC BY-SA 2.5)

The five isotypes present in mammalian immunity are IgA, IgD, IgE, IgG, and IgM (figure 3.1). IgG is the subclass which is responsible for the majority of antibody-based immunity against invading pathogens, and antigen recognition. The five isotypes all display different heavy chain regions denoted by Greek letters which are used for antibody classification, thus IgG has a γ heavy chain region of c.a. 450 amino acids, whereas IgE has an ε heavy chain region of c.a. 550 amino acids. Each heavy chain consists of a constant and a variable region, with the constant region being the same across all antibodies in a subtype. Antibodies also have a light chain, which also consists of a constant and a variable region, and which has two subtypes in mammals, α and κ. The arms of the Y end in hypervariable regions which present the paratope of the antibody, the region which binds to the specific epitope of the target antigen in a lock and key fashion (figure 3.2) through electrostatic and van der Waals forces, hydrogen bonding, and hydrophobic interactions.

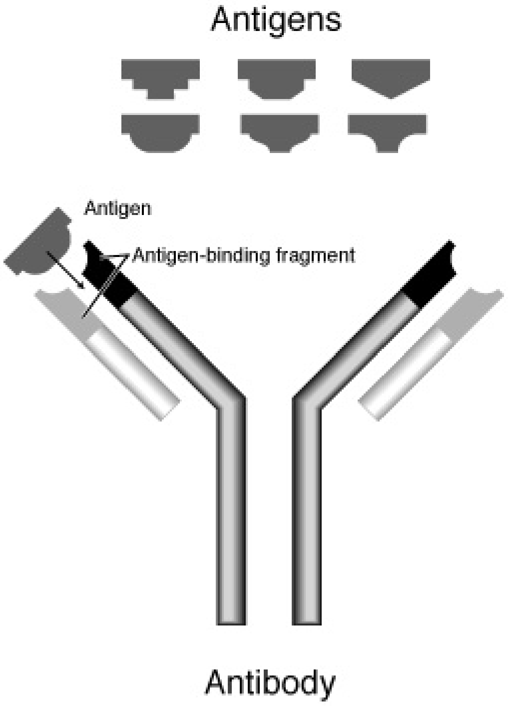

FIGURE 3.2: A FIGURE ILLUSTRATING THE "LOCK AND KEY" MODEL OF ANTIBODY-ANTIGEN INTERACTIONS AND THEIR SPECIFICITY, COURTESY OF THE NATIONAL HUMAN GENOME RESEARCH INSTITUTE.

One role of the immune system in which antibody-antigen interactions play a key role is the differentiation between self and nonself cells and proteins. This is primarily achieved through the major histocompatibility complexes I and II. Bodies identified as nonself are targeted by the immune response, for example, bacteria and viruses, whereas cells identified as self are not marked for destruction by the immune system. Of course, in addition to defending the body from external pathogens, the immune system also has a regulatory role in clearing aging, dead, or diseased cells from the body. Changes in cell status can result in different antigens being expressed, signalling leukocytes to clear cells. Malfunctions in this mechanism, particularly in the recognition of self versus nonself proteins are the underlying cause of immune diseases where the body turns on itself, these mechanisms can also be exploited by diseases such as cancer to avoid detection by the immune system or prevent cell death.

Antibody structure is highly related to their function, and there are several subclasses of antibody with attendant variations in structure illustrated in figure 3.1. These different isotypes mediate the antibody-antigen interaction in different ways, and are defined by differences in the heavy chain crystallisable fragment (Fc) of the protein.

Antibody affinity to antigens is relative rather than absolute, because antibody binding is reversible. This can result in some cross-reactivity of antibodies to other, similar antigens, and some antibodies have very broad reactivity.

When using antibodies for targeting or therapeutic purposes, there are many aspects to consider, the first of which is the choice between polyclonal and monoclonal antibodies.

Antibodies are produced by B-cells. Polyclonal antibodies are produced from multiple B-cells, and therefore recognise multiple epitopes on an antigen, whereas monoclonal antibodies are produced from identical B-cells from a parent clone and recognise a single epitope. For proteins which are expressed at low levels, or which might display polymorphism, polyclonal antibodies amplify the signal arising from the protein and are more tolerant to structural changes including denaturation. Polyclonal antibodies cannot be used for quantification of a target protein due to multiple antibodies binding to different epitopes on the antigen, and can display batch-to-batch variability. Polyclonal antibodies also demonstrate a higher degree of cross-reactivity than monoclonal antibodies due to their recognition of multiple epitopes, and can generate non-specific signal. Monoclonal antibodies on the other hand are highly reproducible, suitable for quantification, and show little to no cross-reactivity due to their specificity for a single epitope on the antigen. Their specificity can make them more prone to losing their ability to bind under some reaction conditions. Recombinant antibodies are manufactured by cloning light and heavy chains into an expression vector which is then introduced to a host such as a bacterium or yeast, or a mammal. They are highly specific, and reproducible.

A further potential consideration in antibody selection in the selection of an antibody is the species in which the antibody was generated.

Antibodies are a popular choice of targeting moiety for contrast agents and also for some therapeutic applications because of their specificity to target proteins where small molecules or oligopeptides may have higher levels of cross-reactivity or non-specific binding.

3.1.2 ANIMAL MODELS IN ATHEROSCLEROSIS

3.1.2.1 MURINE MODELS

Mouse models are very commonly used in preclinical research due to their relatively low-cost and easy handling. Mice are widely available, and the development of genetic knockout mouse models is relatively facile. Mice do not naturally develop atherosclerosis, but genetically modified mice on a C57BL/6 background with disturbed lipid metabolism develop atherosclerotic lesions[1]. The most commonly used mouse model is an Apolipoprotein E knockout (ApoE -/-)[1–3]. ApoE is a protein involved in fat metabolism, which plays a role in both Alzheimer's and cardiovascular disease, and ApoE deficient mice do spontaneously develop atherosclerotic lesions which resemble human lesions[1]. This process can be accelerated by placing the mice on a high fat, high cholesterol diet. Another commonly used genetic knockout mouse model for atherosclerosis is the LDL receptor knockout (LDLR -/-)[3,4].

In this particular study a further adaptation is made to the ApoE model on high fat diet, where a cuff resulting in a stenosis of the vessel is placed on the left carotid artery of the mouse (figure 3.3). This gradual stenosis of the vessel over 1.5 mm results in an area of low shear stress upstream of the cuff, and oscillatory shear stress downstream of the cuff[5]. As discussed in the introduction, the role of wall shear stress in plaque formation governs the differentiation between stable and vulnerable plaque[6]. This model results in vulnerable plaque upstream of the cuff, and stable plaque forming downstream. This is invaluable for internal control studies, and also has the benefit of the unmodified right carotid artery for comparison purposes, resulting in the generation of a huge amount of data from one animal and embracing the spirit of the 3Rs of animal research: Replace, Reduce, Refine.

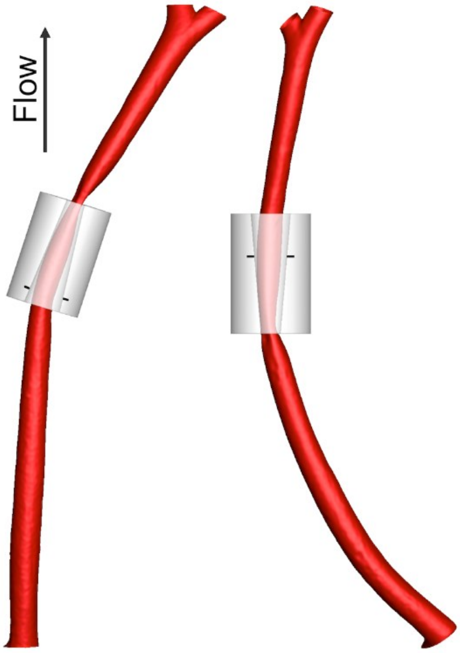

FIGURE 3.3: FIGURE TAKEN FROM MOHRI ET. AL.[7] ILLUSTRATING THE STENOSIS OF THE LEFT CAROTID ARTERY IN THE CUFF MODEL USED IN THIS STUDY.

3.1.2.2 LAPINE MODELS

The original model for atherosclerosis was a rabbit model on high-cholesterol diet[8], and many modern models are based on the New Zealand White rabbit, which has since given rise to two genetically altered variants (though unlike mice these are not transgenic knockouts) which present abnormal lipid metabolism[9]. Watanabe Heritable Hyper Lipidemic (WHHL) rabbits spontaneously develop hypercholesterolemia and atherosclerosis due to an abnormal LDL receptor, whereas St Thomas' Hospital rabbits have an overproduction of LDL and vLDL as a result of familial dysbetalipoproteinemia[1]. These models are usually kept on a chow diet, and their lesions tend to be more similar to early atherosclerotic lesions in humans, with foam cell-rich fatty streaks and little to no formation of advanced lesions or plaque rupture without intervention[10]. Phinikaridou et. al. described a rabbit model of atherosclerosis and atherothrombosis in New Zealand White rabbits with balloon injury and plaque rupture triggered through Russel's Viper Venom and histamine[11]. An excellent discussion of the uses of rabbit models in atherosclerosis can be found by Fan et. al.[8].

3.1.2.3 PORCINE MODELS

Moving from small animal models to large animal models, pigs have well-documented similarities to humans in terms of anatomy, size, and composition in terms of fat to muscle ratios[1,9]. Pig vasculature is virtually identical to human vasculature, and this is a huge advantage when studying a vascular disease like atherosclerosis. Pigs also have lipid profiles, lipid metabolism, and responses to hypercholesterolemia and platelet aggregation which are similar to humans[1,4,10], and this makes the pig a very appealing model for the preclinical study of atherosclerosis. Unlike small animal models, the development of atherosclerosis in pigs is a spontaneous process, and lesions closely resemble those found in the human disease[1,10].

Although pigs naturally develop atherosclerosis, some transgenic pig models have been developed[12], and there are also efforts to miniaturise models, breeding so-called mini- or micro-pigs[1].

3.1.2.4 ISSUES WITH ANIMAL MODELS FOR HUMAN ATHEROSCLEROSIS

Naturally, no animal model of a human condition is perfect. The closest it is possible to get in a preclinical setting is experimentation in non-human primates[2,4], but these models are very highly regulated and very expensive, making them impractical for the majority of research, particularly at its early stages or when trying to prove a principle.

Mouse models are naturally resistant to developing atherosclerosis, meaning that genetic manipulation is necessary. Although murine models are mammalian, the scale of a mouse presents certain challenges when it comes to monitoring disease progression, for example through blood draws, and a difference in blood lipid profile, the expression of proteins, and the behaviour and properties of monocytes[1,4]. In addition, although lesions in mouse models structurally resemble human atherosclerotic plaques, they do not spontaneously rupture[10] and generally occur in different locations of the circulatory system, again limiting the translatability of the model.

Rabbit models represent an improvement on murine models, particularly in the case of the Watanabe rabbit which is naturally hypercholesterolemic. A rabbit aorta also mimics the dimensions of a human coronary artery, and as a mammalian model this does increase the relevance to human atherosclerosis relative to murine models. With the increase in animal size, of course there is also a concomitant increase in the cost of setting up and maintaining the model. While the rabbit lipid profile more closely resembles humans[8], there are still some proteins expressed in human atherosclerosis and involved in lipid metabolism which are not expressed in rabbits[1,8]. As herbivorous creatures, rabbits are also not naturally prone to developing atherosclerosis with the exception of the WHHL model, and again there is a lack of spontaneous plaque rupture[10].

Pig models of atherosclerosis are a step up from mouse and rabbit models in terms of the data they produce, but also in terms of expense. Large animal models are, by necessity, more complex to manage and house, facilities and animals are also more expensive than mice, rat, or rabbit models. The pig model is also time-consuming to set up and run, as opposed to mouse experiments which often have a timeline in weeks as opposed to months or years[1,4,9].

Other animals which are susceptible to, or spontaneously develop atherosclerosis include pigeons and chickens[1,4], however these models have the disadvantage of being nonmammalian. Some useful comparisons of the advantages and disadvantages of various animal models of atherosclerosis can be found in publications by Millon et. al.[1] and Leong et. al.[4], and the American Heart Association has issued a very comprehensive and informative statement on the use and selection of animal models in atherosclerosis studies[2].

AIMS OF THE CHAPTER

This chapter addresses the third and fourth aims presented in section 1.4 of the thesis:

- To conjugate an anti-CX3CL1 antibody to the surface of the SPION which demonstrates the best properties for a long-circulating *in vivo* contrast agent.
- To test the contrast agent in a murine model of atherosclerosis and perform histological and *in vitro* studies to support the preclinical work.

It presents the carbodiimide coupling chemistry used to couple the antibody to the nanoparticle surface, the *in vitro* studies to validate the specificity and non-toxicity of the probe, and the *in vivo* imaging studies with concurrent histological verification. It presents the resulting data and uses these data to draw conclusions regarding the behaviour of the probe and its validity in terms of the project aims.

3.2 COUPLING OF TARGETING MOIETY

3.2.1 ANTIBODY COUPLING REACTION

The antibody coupling reaction was performed using carbodiimide chemistry (DCC coupling). Carbodiimides are molecules with the structure RN=C=NR, and the coupling chemistry is often abbreviated to DCC after N,N'-dicyclohexylcarbodiimide which was the first carbodiimide used synthetically for amide bond formation coupling reactions. In this case EDC or 1-Ethyl-3-(3-dimethylaminopropyl)carbodiimide was the coupling agent due to its easier handling and lower allergen risk. The role of the carbodiimide in amide bond formation is to activate the carboxylic acid group, which is unreactive particularly compared to anhydride or acid chloride alternatives. The reaction mechanism is illustrated in Figure 3.4.

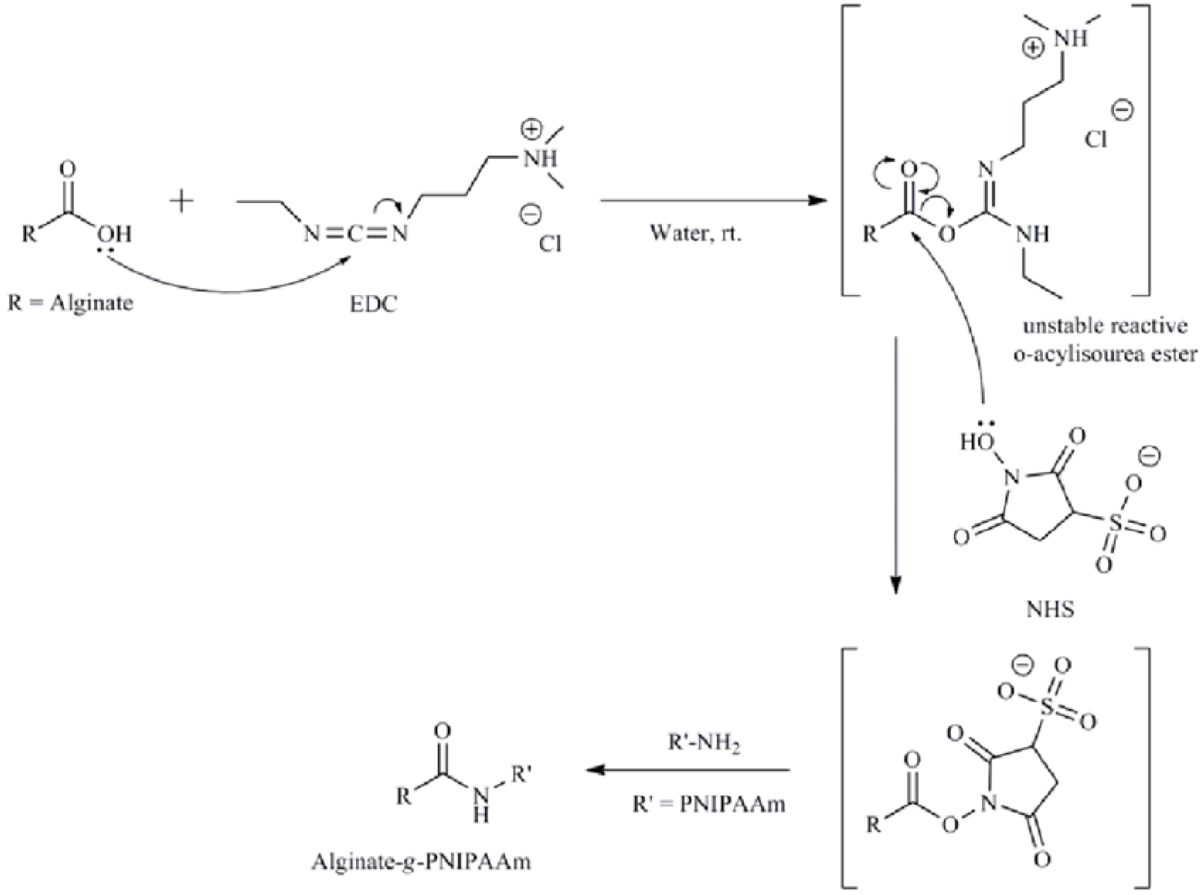

FIGURE 3.4: MECHANISM ILLUSTRATING THE COUPLING REACTION BETWEEN AN AMIDE AND CARBOXYLIC ACID THROUGH EDC-NHS COUPLING CHEMISTRY, USED WITH PERMISSION FROM BENTHAM SCIENCE, TAKEN FROM CHOPIN ET. AL.[13].

The intention of using DCC chemistry was to form an amide bond between the carboxylic acid present on the nanoparticle surface from the PMAO coating with a lysine side chain in the antibody. Lysine is an amino acid which is common in proteins, and as antibodies are large protein structures (approximately 150 kDa), there is a high probability of coupling to a lysine residue. Although there is no sequence data for the targeting antibody used here, previous work in the group isolated a single-chain variable fragment (scFv) from the Tomlinson I and J libraries against Fractalkine, and lysine was not present in high frequency there[14]. This increases the probability that, although the coupling reaction is not site-specific, the coupling will occur between the nanoparticle and a lysine side chain on the antibody heavy chain regions which are not involved in targeting. This is an advantage of using a whole antibody as opposed to a scFv, although there are also disadvantages such as potentially stimulating unwanted immune responses.

The reaction between the carbodiimide and the acid is illustrated in Figure 3.4, and results in the formation of an O-acylisourea, which is an activated leaving group. Although it is possible to couple directly to an amine or other cross-linking functional group from this intermediate, it is more common to add N-hydroxysuccinimide (NHS) to the reaction mixture which forms an NHS-ester. This is more stable than the O-acylisourea and also reacts more favourably at physiological pHs where the EDC leaving group prefers acidic conditions. Given the manipulation of a protein and an iron oxide nanoparticle in this situation, although mildly acidic conditions are appropriate for the installation of the EDC, the ability to use physiological/mildly basic conditions for the NHS-coupling and the final amide bond formation between the antibody and the nanoparticle is hugely preferable. The conditions of pH 4.5 which is needed for efficient coupling without the NHS-ester would likely result in digestion of both the protein and the nanoparticle to which it is being coupled.

Although these coupling conditions have a long history in synthetic chemistry, they can be difficult to optimise and are sensitive to changes in pH. In this case conditions which had been previously optimised by another member of the group were tested and shown to be successful. Potential alternatives to this approach could include the use of thiol-based click chemistry as described by McCarthy et. al.[15].

3.2.2 BCA ASSAY

It was necessary to confirm the coupling of the antibody to the nanoparticle, and to quantify the amount of protein present on the surface of the nanoparticle. The BCA assay is a useful tool for spectroscopic confirmation and quantification of protein in solutions, and is similar to the Biuret test for proteins. The Biuret test is the reduction of Cu^{2+} to Cu^{+} by proteins in an alkaline solution, and in the BCA assay, this aqueous Cu^{+} is then captured by bicinchoninic acid (BCA), forming a complex with a strong purple colour which allows for colorimetric measurement. Concentrations are measured with reference to solutions of a standard protein, often Bovine Serum Albumin (BSA) which is what was used in this case. Figure 3.5 illustrates an example plate from a run of this assay demonstrating the gradient in the standard curve and the detection of protein in experimental solutions.

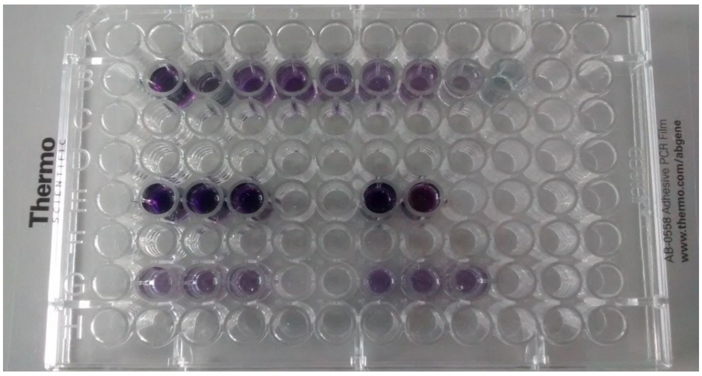

FIGURE 3.5: 96-WELL PLATE FOR THE BCA ASSAY SHOWING THE COLORIMETRIC GRADIENT RELATED TO PROTEIN CONCENTRATION.

The kit was used following instructions for the microplate procedure due to the small volume of contrast agent available to test. The colorimetric measurements were not performed on a microplate reader, but on a UV-Vis spectrometer after incubation for 1 hour at room temperature. This time period was important due to the lack of a fixed endpoint for this assay, and the absorption was measured at 562 nm within 10 minutes for all samples. The baseline absorbance was subtracted from standard and sample absorbance readings and a graph was plotted (Figure 3.6), allowing the determination of protein concentration in the solution to be 535.8 ug/ml, which equates to a percentage of nanoparticles with targeting moiety of around 2%. Although this is a low percentage, this might not be a hindrance due to the amount of contrast agent which is cleared by the immune system, through the RES, or which simply accumulates in other areas such as the injection site. If the majority of contrast agent is non-targeted, the majority which is cleared will also been untargeted, meaning that the proportion of targeted contrast agent reaching the site of interest is likely to be much higher, enhancing the specificity of the signal change. The absorbance measurements were also corrected for the absorbance of a solution of SPIONs at 562 nm, though this was negligible. The measurement of SPION control absorbance was performed separately.

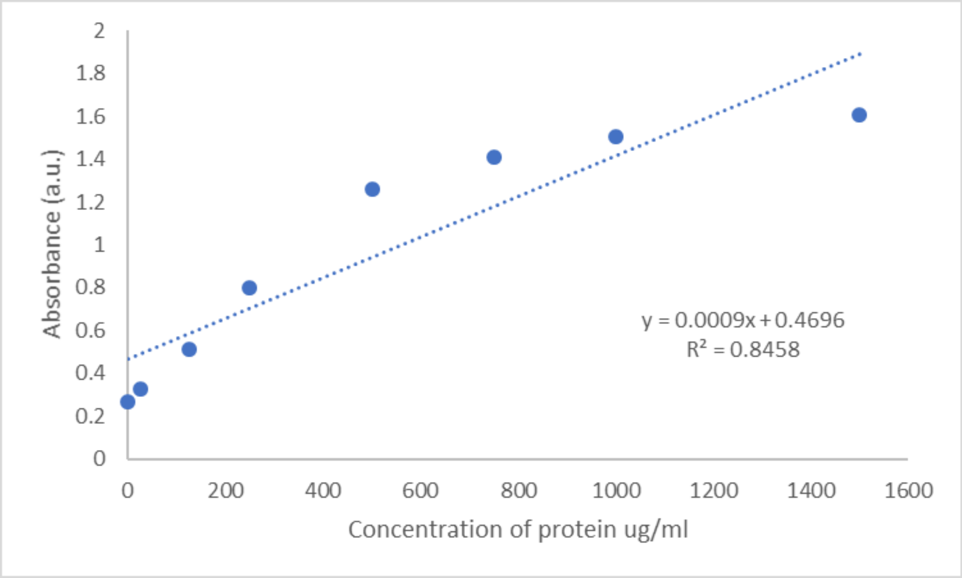

FIGURE 3.6: GRAPH SHOWING THE ABSORBANCE AT 562 NM VERSUS PROTEIN CONCENTRATION (UG/ML) AS A CALIBRATION CURVE FOR THE DETERMINATION OF PROTEIN CONCENTRATION AND CONFIRMATION OF ANTIBODY COUPLING TO SPION SURFACE USING THE BCA ASSAY.

Although the BCA assay is confirmation that the antibody was present in the resuspended nanoparticles, it gives no indication as to whether the antibody has retained its targeting properties or been denatured in the course of the coupling, or by unintentional coupling of the nanoparticle within the active site. This can only be confirmed by performing a binding study. It also does not differentiate between bond formation of physisorption of the antibody to the polymer which could potentially be reversible particularly under *in vivo* conditions. Further controls would be needed to clarify this.

3.2.3 BINDING

The lack of site-specificity in the coupling reaction between the SPIONs and the targeting antibody required subsequent confirmation that the antibody's ability to bind to the target protein had not been affected. Binding to the nanoparticle surface also had the potential to affect the ability of the antibody to interact with CX3CL1 through steric hindrance or other means. In order to confirm that the coupling conditions used did not denature or otherwise destroy the protein, and that coupling to the nanoparticle surface did not prevent binding to the target, a binding study was designed.

The binding assay was designed to be analogous to an ELISA assay, but with the use of Berlin Blue to detect iron as the read-out. An example of the general design of the assay can be seen in figure 3.7.

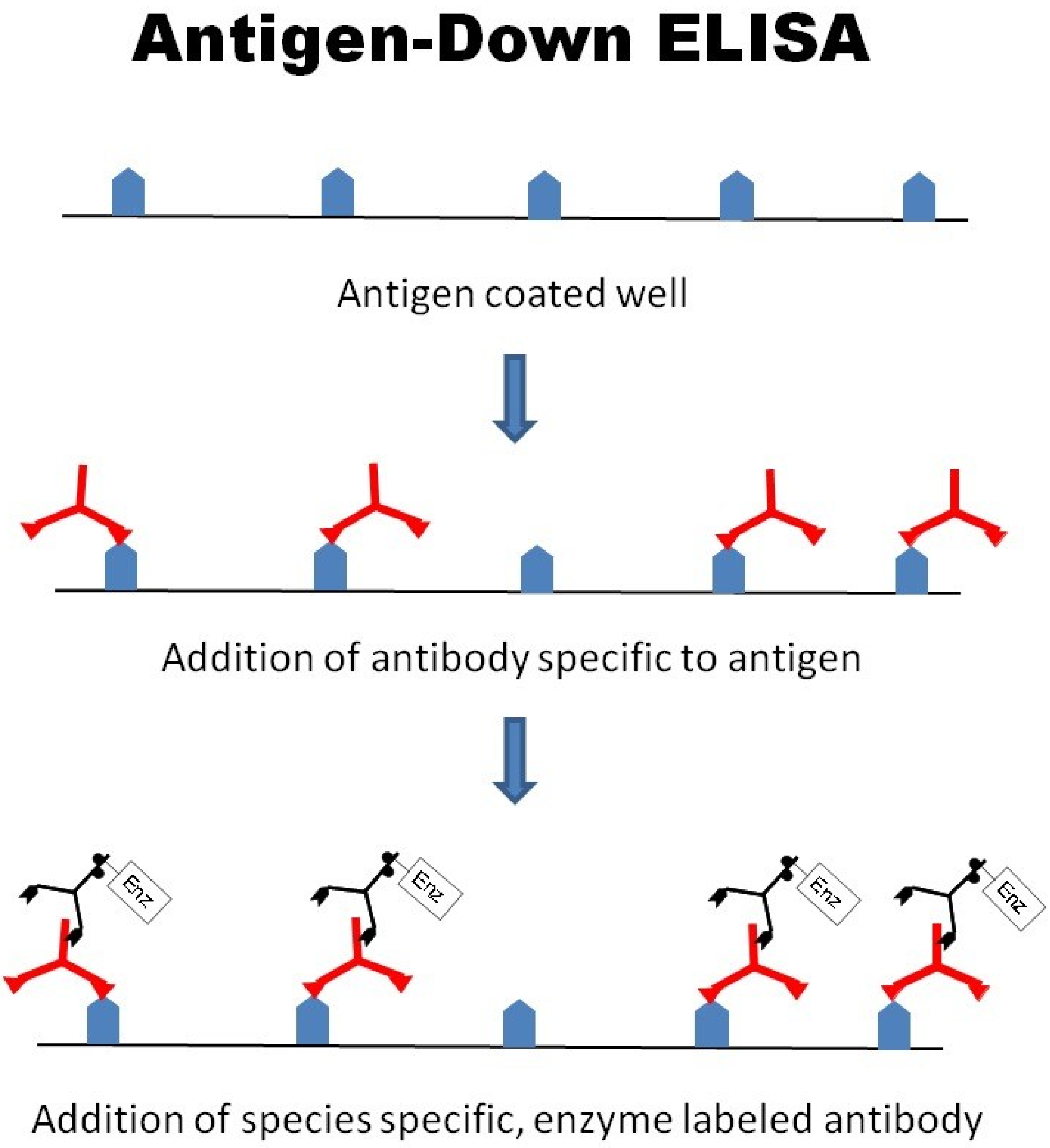

FIGURE 3.7: GENERAL ILLUSTRATION OF AN ANTIGEN-DOWN ELISA ASSAY, ANALOGOUS TO THE BINDING ASSAY PERFORMED HERE. IMAGE USED UNDER CC BY-NC-SA 3.0 TAKEN FROM IMMUNOASSAY METHODS[16].

A 96-well plate was prepared, coated with CX3CL1 and blocked with BSA to prevent non-specific binding. The plate was then incubated with both targeted and untargeted SPIONs, and treated with Berlin Blue to digest the SPIONs and allow the detection of iron through UV-Vis spectroscopy. Initially a time course was measured across wavelengths to determine the optimal incubation time and λ for the measurement, and this was set at three hours of incubation and 800 nm. Some signal was observed from BSA which is known to contain small amounts of iron and also validates the sensitivity of the assay itself. The results are presented in figure 3.8.

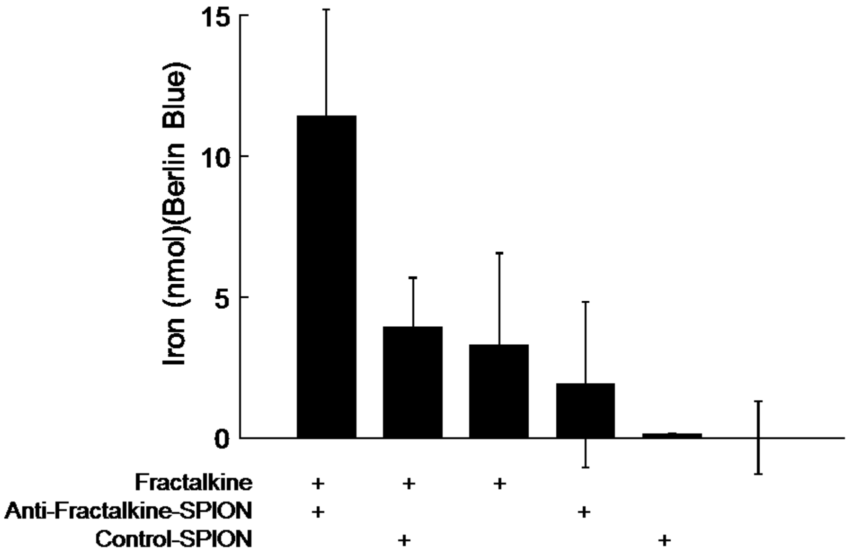

FIGURE 3.8: GRAPH ILLUSTRATING THE BINDING STUDY, SHOWING A HIGHER IRON CONCENTRATION DETECTED IN WELLS CONTAINING BOTH FRACTALKINE AND TARGETED SPIONS COMPARED TO CONTROLS. THE KEY BENEATH INDICATES THE CONTENTS OF EACH WELL, WHICH SPION WAS USED, AND WHETHER OR NOT THE TARGET PROTEIN WAS PRESENT. A SET OF CONTROL WELLS WITH NO FRACTALKINE AND NO SPIONS WERE USED TO INDICATE ABSORBANCE FROM THE STAIN AND THE PLATE IN THE ABSENCE OF PROTEIN AND SPIONS.

A higher absorbance, calibrated to a higher iron concentration through a standard curve run contemporaneously on the same plate demonstrates that after coupling to the surface of the nanoparticle, the antibody retains its binding ability and is still capable of targeting CX3CL1 expression. This validates that the probe can be moved forward into *in vitro* toxicity studies, and then potentially through to preclinical models, and confirms that the EDC coupling conditions are sufficiently mild to avoid denaturing the protein.

3.3 *IN VITRO* STUDIES

These studies were planned in conjunction with and supported by Dr Joseph Boyle, and undertaken by Eunice Wong at Hammersmith Hospital.

3.3.1 INVESTIGATION OF NANOPARTICLE TOXICITY

To confirm that the nanoparticles were non-toxic, *in vitro* studies on murine RAW 264.7 immortalised macrophages were used for viability testing with the XTT assay, with an eye to potential cell death arising from iron overload. The effect of SPIONs was compared to the effect of $FeCl_3$ at a range of concentrations of iron, and at 2 and 24 hours incubation with the metal treatment. Controls included untreated cells, and medium with SPIONs at similar concentrations to correct for the absorbance arising from both the SPIONs and cells, and to give a measure for cell survival in the absence of the metal. The absorbance was measured at 450 nm, and at both 2 and 24 hours of incubation with metal and XTT (which also has some cytotoxic effects).

After 2 hours the cells treated with SPIONs show no decrease in stability with measured survival rates of 120% (likely due to continued cell division) at all concentrations, whereas those treated with $FeCl_3$ show a decrease in cell viability at higher concentrations, with survival rates in the region of 75%.

After 24 hours the cells treated with SPIONs continue to show higher rates of survival than those treated with $FeCl_3$, and at higher concentrations of iron a particularly interesting phenomenon was observed whereby percentage survival jumped hugely. This is likely due to a mitochondrial effect, or perhaps the stimulus of an uncharacterised biological pathway leading to higher rates of cell division.

These results are illustrated in Figure 3.9 and 3.10 below.

Based on these studies it seems unlikely that the SPIONs would lead to iron overload related toxicity *in vivo*, possibly due to the restriction of iron within the crystal structure as opposed to the free iron of FeCl3. This might also reduce the internalisation of iron by proteins such as transferrin. These results were further supported by *in vivo* tests where animals injected with the contrast agent then continued to live with no observed complications or ill health for several weeks before sacrifice.

Further studies on this contrast agent performed by J.J. Boyle at Hammersmith Hospital suggest an atheroprotective effect from the SPIONs, in contrast to what might be expected from an agent with free iron which would generate reactive oxygen species and exacerbate the atherosclerotic feedback loop. Studies were performed in human blood-derived macrophages, and cell viability and oxidative stress measures both showed clear differences between targeted and untargeted SPIONs, suggesting that the anti-CX3CL1 targeting has an atheroprotective value, and also that labelling of the contrast agent with the antibody was at levels sufficient for a biological effect[17]. These findings are not presented here but are due to be published in Nanotheranostics[17].

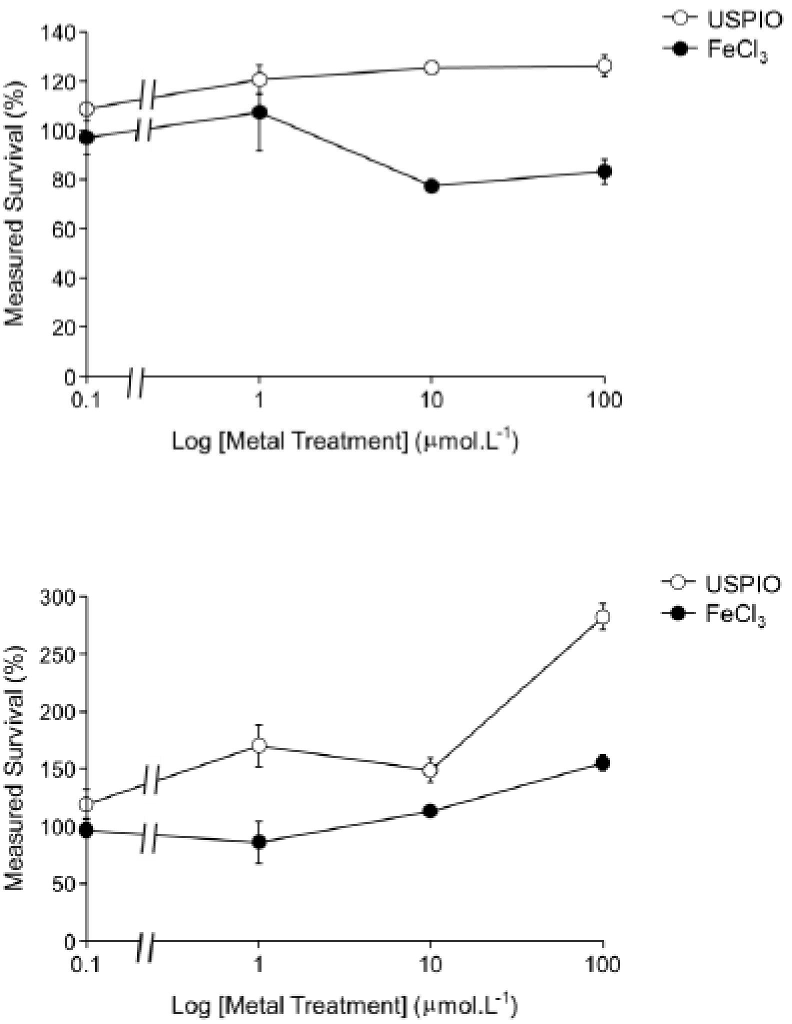

FIGURE 3.9: GRAPHS DISPLAYING THE MEASURED SURVIVAL OF RAW CELLS AT 2 HOURS (TOP) AND 24 HOURS (BOTTOM) AFTER EXPOSURE TO FECL3 OR SPIONS AS MEASURED BY XTT ABSORBANCE AT 450 NM

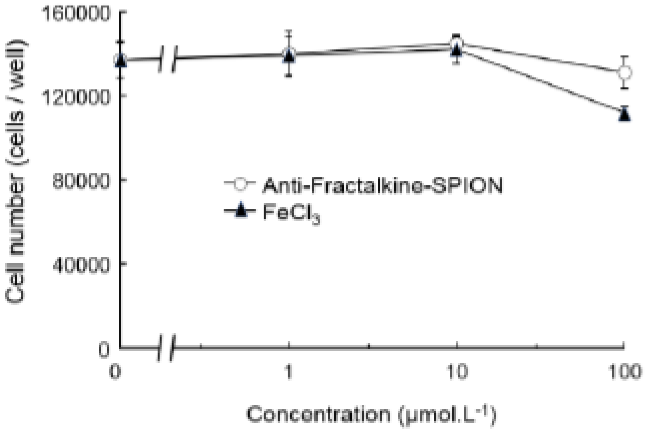

NS, ANOVA on ranks (Kruskal-Wallis)

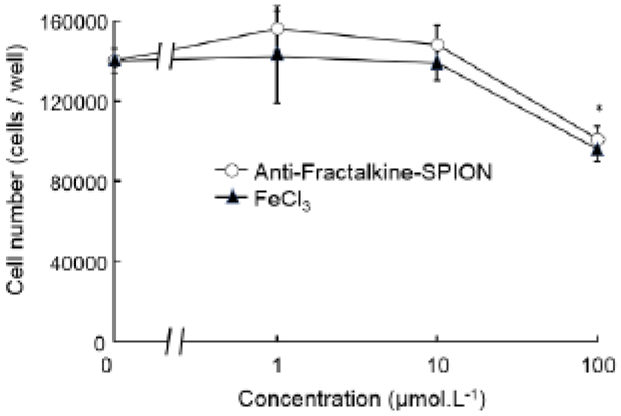

* $p<0.05$, ANOVA on ranks (Kruskal-Wallis)

FIGURE 3.10: GRAPHS ILLUSTRATING THE CELL COUNTS AT 2 HOURS (TOP) AND 24 HOURS (BOTTOM) SHOWING A SLIGHT IMPROVEMENT IN SURVIVAL AT 24 HOURS WITH SPIONS COMPARED TO $FECl_3$ AT THE HIGHEST CONCENTRATION OF IRON, HOWEVER THE REDUCTIONS ARE SIMILAR

3.4 *IN VIVO* STUDIES

3.4.1 PROOF-OF-CONCEPT

Two animals were used for proof-of-concept scans, comparing images before and after the administration of contrast agent. Both animals were ApoE-/- females with a cuff on the left carotid artery and on high fat diet, as detailed in the experimental section. These scans indicated that there was a difference in signal between the pre- and post-contrast images, and that there was uptake in the diseased vessel wall. The animals were not immediately euthanised after scanning, but several weeks after the scanning protocol, and in this time they showed no ill-effects or consequences from the contrast agent. The overall purpose of these scans was to develop the examination card for subsequent studies, and define scanning parameters, they also showed that the SPIONs were still in circulation 24 hours post-injection with no change in signal in the liver. This was particularly exciting given that SPION contrast agents which have previously received FDA approval have been used for liver imaging. This contrast agent was designed to be long-circulating, and the proof-of-concept scans demonstrated that this had been successfully achieved, the survival of the mice with no ill effects post-scanning also showed that the SPION agent was non-toxic. No quantitative analysis was performed on these scans, the purpose of them was to establish imaging protocols for the study reported in section 6.4.2, and to ensure the planned dose was detectable at the 24 hour time point.

3.4.2 SPIONs AND Gd-ESMA

Due to potential uncertainty regarding areas of signal void arising from the presence of contrast agent versus areas of signal void occurring naturally in the image, for example due to proximity to the trachea, the decision was made to scan the mice with an established elastin contrast agent[18] (Gd-ESMA) to identify plaque regions which could then be compared to the signal arising from the SPIONs as a confirmation of the presence of plaque. Gd-ESMA is a molecular species which binds to elastin with high specificity. It has been used for imaging atherosclerotic plaque burden and scar in myocardial infarction[18,19], and allows the identification of plaque areas in this study to compare to regions of signal void detected with SPIONs, to minimise the mis-identification of regions which are signal artefacts arising from proximity to the trachea or other artefacts as regions of plaque.

A time course of experiments to determine the optimal window for SPION:blood contrast would also be a useful study. Some work in the literature suggests 24, 48, and 72 hours. Unfortunately for this study limitations in access to equipment required the selection of a single time point, and 24 hours was selected because it reduced the possibility of missing the agent altogether if clearance was more rapid than expected. The proof-of-concept work had also demonstrated that the agent was still present after 24 hours.

The decision was also taken to use healthy ApoE-/- with targeted SPIONs for control purposes, as opposed to non-targeted SPIONs in diseased animals, in order to look at non-specific uptake that was unrelated to disease. SPIONs have already been used to image plaque, but not to differentiate between stable and vulnerable plaques, so it was already known that there would be uptake in the vessel wall irrespective of plaque phenotype and the question of non-disease-related non-specific uptake was more interesting from a control point of view. The study used 6 diseased and 6 control mice, the images were analysed in Osirix and statistical analysis was carried out in Graphpad Prism using multiple non-parametric t-tests with a Holm-Sidak correction for multiple comparisons.

3.4.2.1 Cuff Placement

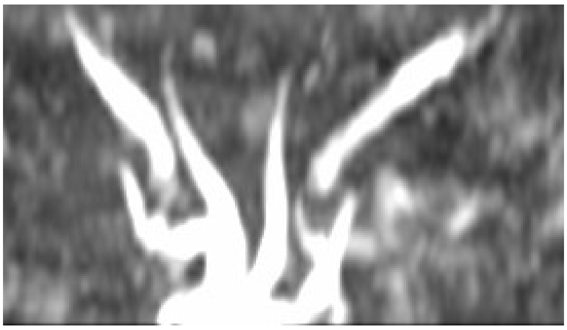

FIGURE 3.11: IMAGE FROM A STRUCTURAL MRI SCAN SHOWING THE AORTIC ARCH AND THE ANATOMY OF THE VESSELS BRANCHING FROM IT: THE BRACHIOCEPHALIC DVIDING INTO THE RIGHT SUBCLAVIAN AND RIGHT CAROTID ARTERIES, THE LEFT CAROTID, AND LEFT SUBCLAVIAN ARTERIES.

Given that the purpose of the cuff on the left carotid was to introduce stenosis of the vessel and therefore induce separate regions of vulnerable and stable plaque, upstream and downstream respectively, the first important question for analysing the imaging study and contrast agent behaviour was being able to identify the location of the cuff *in vivo* to compare uptake in vulnerable and stable plaque. Figure 3.11 is an image from a structural scan showing the aortic arch and the three vessels branching from it, to give context for the location of the cuff. The cuff location was identified by plotting the lumen area in mm^2 across slice numbers, with the slice number standardised to 1 being the first slice with three individually visible vessels above the aortic arch (Figure 3.12). During surgery the cuff was placed around the carotid and then tethered to the muscle to prevent motion along the vessel, particularly at retrieval. Slice thickness was 0.5 mm and cuff length was 1.5 mm, therefore a steady decrease in lumen area over three consecutive slices would be indicative of the cuff location.

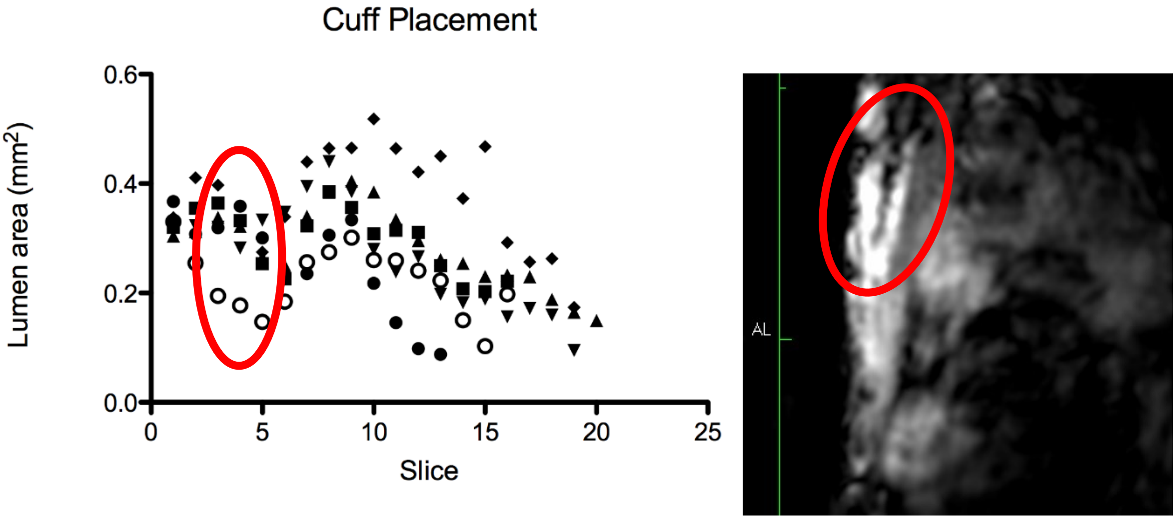

FIGURE 3.12: GRAPH SHOWING AREA OF LUMEN IN mm^2 VERSUS SLICE NUMBER FOR ALL SIX MICE, AND AN IMAGE FROM AN ANATOMICAL SCAN SHOWING THE STENOSIS OF THE VESSEL IN VIVO.

In all six animals it is possible to see a decrease in lumen area over three slices, beginning at slice 4 (slices standardised to slice 1 being the first slice with all three vessels visible and no trace of aortic arch). This is consistent across all the animals, as would be expected given the cuff being tethered in position to the adjacent muscle. This gives three slices containing vulnerable plaque upstream of the cuff, which is not a huge area but does allow some comparison between plaque regions proximal and distal of the cuff. It is challenging to make direct comparisons between animals without the use of an anatomical benchmark due to the positioning of the animal on the scanner bed which is very susceptible to inter-animal variation. This also means that it is not possible to be certain that slices are directly transverse through the vessel, which leads to further challenges in analysis of the signal variations.

3.4.2.2 VULNERABLE AND STABLE PLAQUE REGIONS

The hypothesis of this study was that targeting via an anti-CX3CL1 antibody would result in significantly higher uptake of nanoparticles in regions of vulnerable plaque. The animal model results in the formation of vulnerable plaque upstream of the cuff, and stable plaque downstream, allowing a direct comparison within the modified vessel, it also has the unmodified right carotid artery (RCA) which can serve as an internal control, although it cannot be ruled out that fatty streaks or other plaque precursors may be present due to the spontaneous development of plaque in ApoE-/- mice on high fat diet. Measurements were also taken in the brachiocephalic artery which is a known plaque site which is of particular interest to the Botnar group. Interestingly it was observed in the disease model that the brachiocephalic arteries of the cuffed animals were considerably enlarged compared to those of the healthy animals, or ApoE-/- mice on high fat diet without the cuff modification. This enlargement may well arise as a result of compensation for the flow restriction resulting from the stenosis. Images from these scans can be seen in figure 3.13.

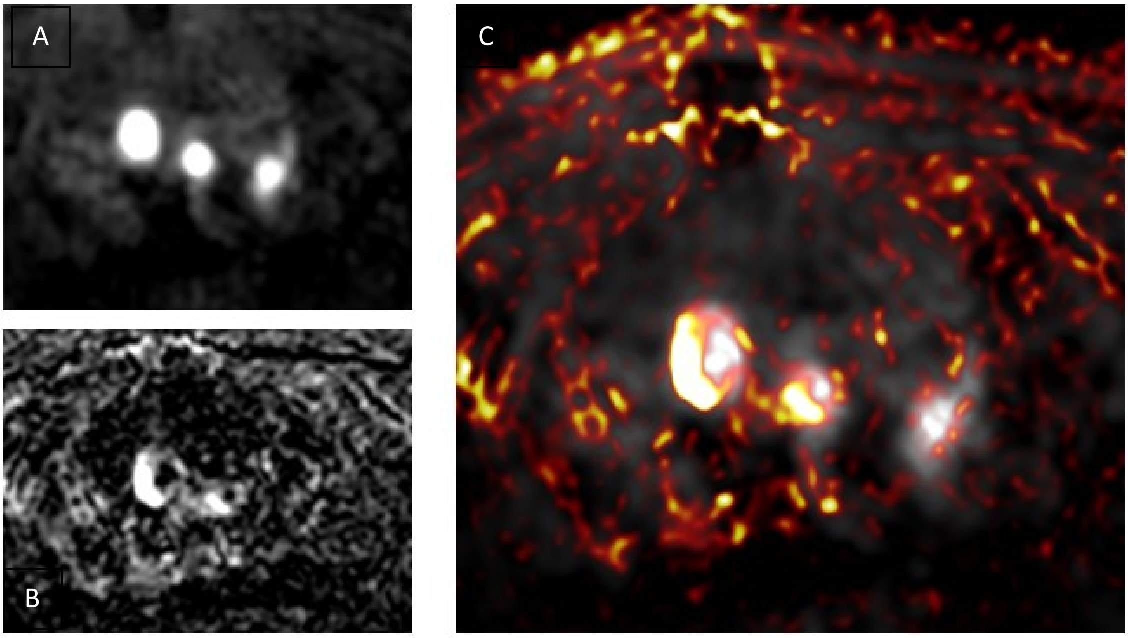

FIGURE 3.13: A) ANATOMICAL T1 SCAN SHOWING THE BRACHIOCEPHALIC ARTERY, LEFT CAROTID ARTERY, AND LEFT SUBCLAVIAN ARTERY (L-R), B): INVERSION RECOVERY IMAGE SHOWING AREAS OF LATE GADOLINIUM ENHANCEMENT FROM GD-ESMA IN THE VESSEL WALLS. C) IMAGE OVERLAY SHOWING THE AREAS OF ENHANCEMENT IN RELATION TO THE VESSELS. THE BRACHIOCEPHALIC ARTERY WAS OBSERVED TO BE ENLARGED RELATED TO OTHER MODELS, AND THIS IS LIKELY TO BE A RESULT OF COMPENSATION DUE TO THE RESTRICTION THE CUFF PLACES ON THE LEFT CAROTID.

The Gd-ESMA scans showed a significant difference between uptake in the cuffed vessel and the internal control vessel (p=0.018) and again a significant difference between the late gadolinium enhancement signal from Gd-ESMA in the cuffed disease vessel compared to both the left and right carotid arteries in the control animals (p=0.002, 0.000095) (Figure 3.15). The data was analysed using multiple non-parametric t-tests corrected for multiple comparisons by the Holm-Sidak method, and was found to be statistically significant. There was no notable difference in Gd-ESMA enhancement between the stable and vulnerable plaque regions, but it was not expected that elastin content would differ significantly, particularly given that Gd-ESMA binds to both the cross-linked mature form of elastin, and tropoelastin.

Pleasingly, the contrast in the SPION scans very much mirrored the Gd-ESMA enhancement, validating the novel contrast agent against a verified benchmark. Examples of the T2* images can be found in figure 3.14. This was a very important piece of evidence to support the design of the contrast agent, and provided a foundation which could be built on for further optimisation. Again, there was a significant difference between the modified vessel and the internal control vessel (p=0.018), and between the modified, diseased vessel and both vessels in the control animals (p=0.005, 0.002) (Figure 3.15). The data was analysed using multiple non-parametric t-tests corrected for multiple comparisons by the Holm-Sidak method, and was found to be statistically significant.

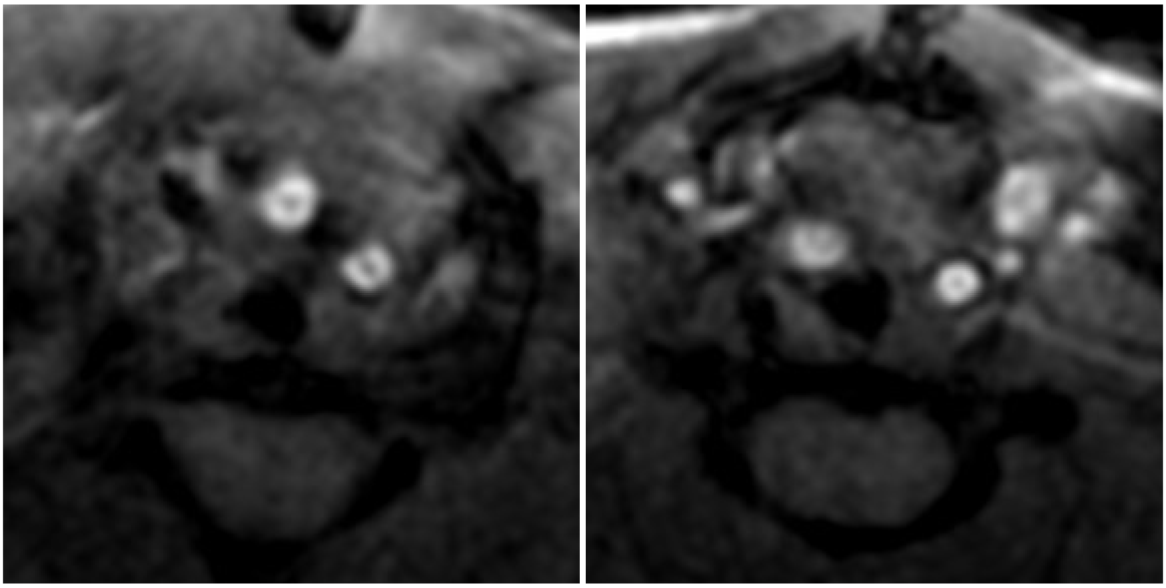

FIGURE 3.14: TWO EXAMPLES OF T2* ECHO SCANS BASED ON THE PROTOCOL FROM MAKOWSKI ET. AL.[20] SHOWING NEGATIVE CONTRAST AREAS IN THE VESSEL WALLS.

Unfortunately there was no significant difference between the uptake of either contrast agent between the vulnerable plaque upstream of the cuff, and the stable plaque downstream of the cuff (p=0.3225) (Figure 3.15). This may be as a result of the low proportion of contrast agent which was effectively labelled with the targeting antibody, potential loss of binding of the antibody, particularly given the non-site specific nature of the coupling, although it is statistically unlikely for the coupling to have taken place in the active site. It might also be that CX3CL1 expression was not sufficient to overcome the passive accumulation of the nanoparticles in plaque regions through phagocytosis by macrophages or even through the EPR effect. Further experiments using unlabelled nanoparticles as a control would be useful in clarifying this.

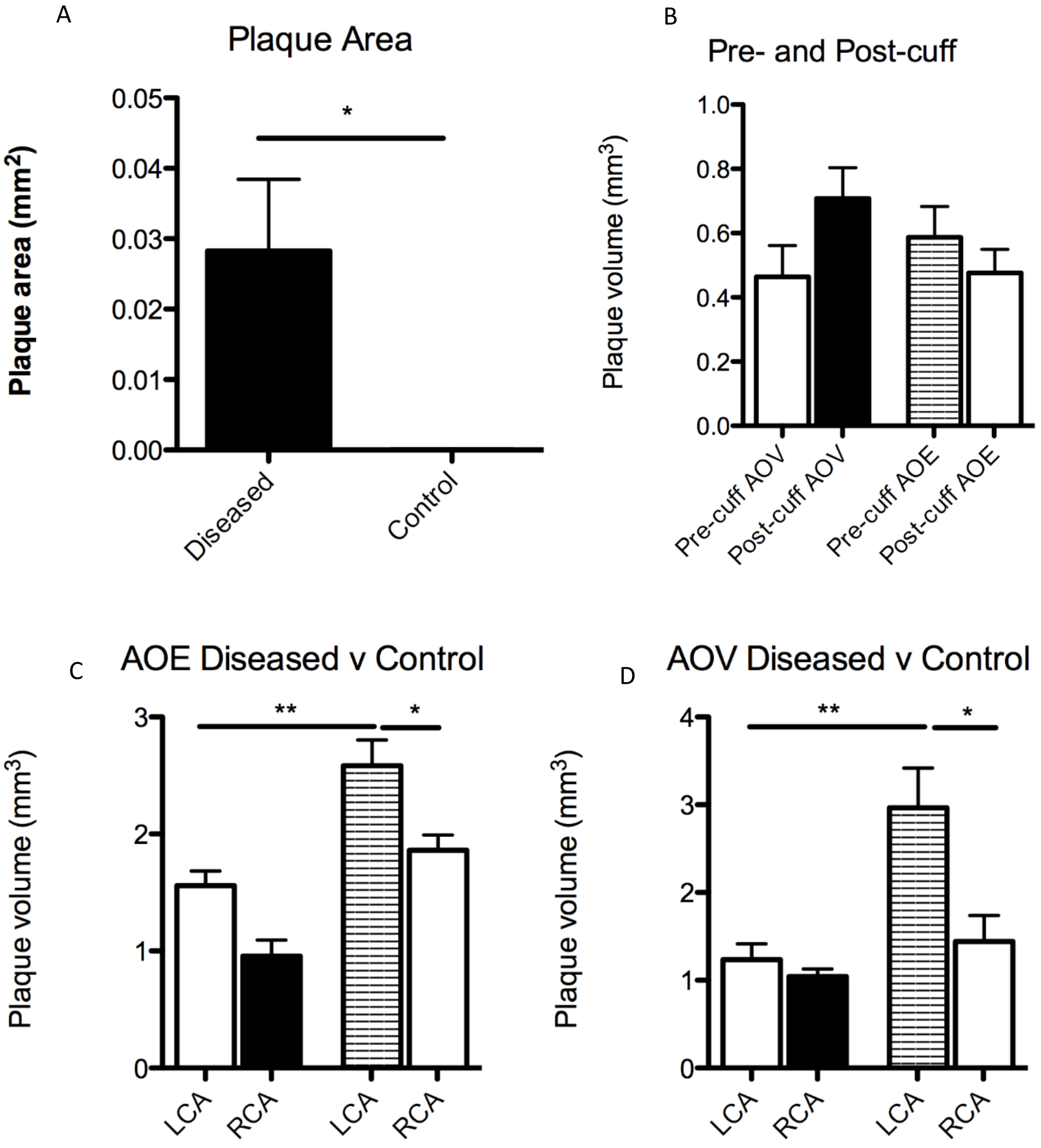

FIGURE 3.15: GRAPHS ILLUSTRATING A) THE PLAQUE AREA MEASURED IN THE DISEASED AND CONTROL ANIMALS, SHOWING THAT THE CONTROL ANIMALS HAD NO PLAQUE BURDEN. B) THE LACK OF SIGNIFICANT DIFFERENCE IN CONTRAST AGENT UPTAKE BETWEEN REGIONS ABOVE AND BELOW THE CUFF IN BOTH GD-ESMA AREA OF ENHANCEMENT (AOE) AND SPION SCANS AREA OF VOID (AOV). C) THE AREA OF LATE GADOLINIUM ENHANCEMENT MEASURED IN GD-ESMA SCANS BETWEEN CONTROL ANIMALS (LEFT) AND DISEASED ANIMALS (RIGHT), COMPARING THE LEFT AND RIGHT CAROTID ARTERIES (LCA AND RCA RESPECTIVELY) AND SHOWING A SIGNIFICANT DIFFERENCE BETWEEN THE MODIFIED DISEASED VESSEL AND BOTH SETS OF CONTROLS. D) THE AREA OF VOID MEASURED IN SPION SCANS BETWEEN CONTROL ANIMALS (LEFT) AND DISEASED ANIMALS (RIGHT) SHOWING A SIGNIFICANT DIFFERENCE BETWEEN THE MODIFIED DISEASED VESSEL AND BOTH SETS OF CONTROLS.

In summary, while there was no significant difference in SPION uptake in regions upstream or downstream of the cuff, there was a significant difference in regions of plaque between the LCA and RCA, and an increased significance compared to the control vessel. The areas of signal void arising from SPION uptake strongly correlate to the areas of positive signal from Gd-ESMA. Although unfortunately the SPIONs are not specific to vulnerable plaque, and the targeting of this probe at this time is not sufficient to give a delta difference in signal between stable and vulnerable plaque uptake. The SPION behaviour closely mimics that of a known, characterised, commercial contrast agent which is very exciting for a novel probe. This provides a foundation for further optimisation of the contrast agent, for example through the introduction of a secondary target or other functionality which would improve the specificity of the probe.

3.5 HISTOLOGY

3.5.1 TRICHROME STAINING

In order to identify plaque regions and areas of disease in the sections of vessel, sections were stained with trichrome staining which differentiates collagen from muscle tissue and cytoplasm. The protocol was based on Masson's trichrome stain, and was very useful in selecting sections for further staining. Examples of trichrome stained sections can be seen in figures 3.16 and 3.17.

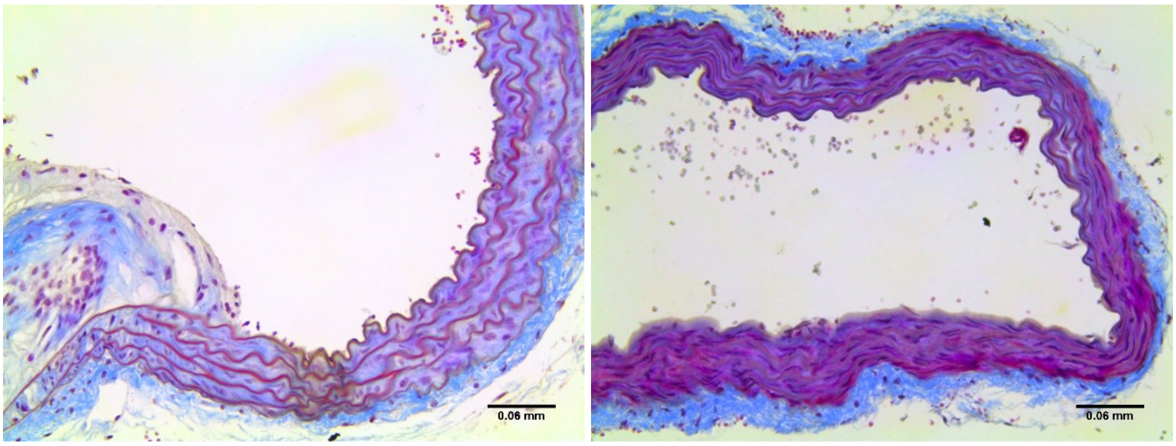

FIGURE 3.16: TWO EXAMPLES OF SECTIONS STAINED WITH TRICHROME STAINING, INCLUDING A PLAQUE REGION, AT 20X MAGNIFICATION.

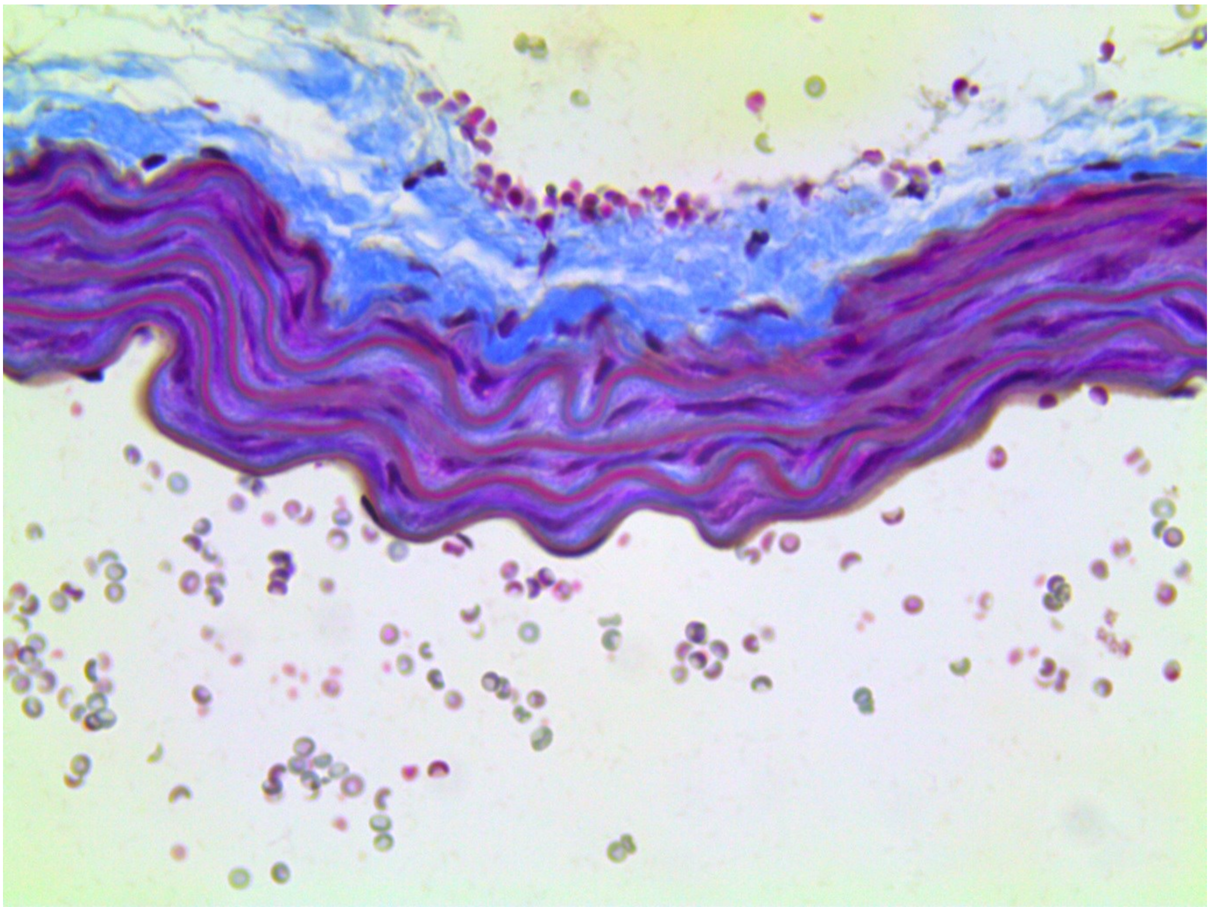

FIGURE 3.17: ANOTHER EXAMPLE OF TRICHROME STAINING AT 40X MAGNIFICATION, SHOWING THE DIFFERENTIATION BETWEEN COLLAGEN, MUSCLE FIBRES, CYTOPLASM, AND NUCLEI. ERYTHROCYTES ARE ALSO VISIBLE WITH THEIR CLASSIC CONCAVE SHAPE.

3.5.2 ELASTIN AND TROPOELASTIN STAINING

Tropoelastin is the immature, non-cross-linked form of elastin which is of particular interest to the Botnar group, and which is potentially relevant to vulnerable plaque imaging, particularly in detecting degradation of the extracellular matrix. Elastin is a major component of the vessel wall, alongside collagen, and is found in the non-cross-linked and cross-linked forms. Gd-ESMA is an elastin-targeted gadolinium contrast agent for MRI which has been well characterised. The relative proportions of elastin and tropoelastin in the plaque regions were of interest in further characterising and evaluating vulnerable plaque formation in the preclinical model.

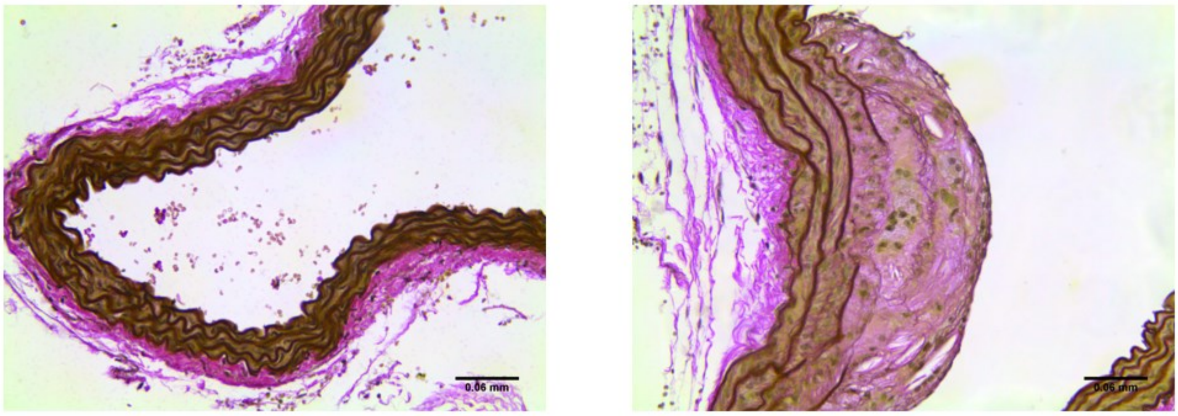

FIGURE 3.18: EXAMPLES OF SECTIONS STAINED FOR ELASTIN, SHOWING A SECTION OF CONTROL VESSEL ON THE LEFT, AND A PLAQUE REGION ON THE RIGHT WITH SOME ENDOTHELIAL DYSFUNCTION.

Staining for elastin and tropoelastin was intended to identify regions of plaque, confirm the presence of both proteins in plaques, and to measure whether there was a significant difference in the tropoelastin content of diseased vessels or sites of atherosclerosis compared to healthy vessels. Given that plaque, particularly vulnerable plaque, is associated with changes in the extracellular matrix, it was an interesting question regarding vessel wall composition, however it was not possible to determine with any confidence whether there was a difference between vulnerable and stable plaque in the ratio of elastin to tropoelastin in the vessel wall. This might be an interesting follow-up study, scanning with Gd-ESMA and Gd-TESMA[21] in order to measure differences in signal in the known stable and vulnerable plaques arising as a result of the cuff model. Examples of sections stained for elastin and tropoelastin can be seen in figures 3.18 and 3.19 respectively.

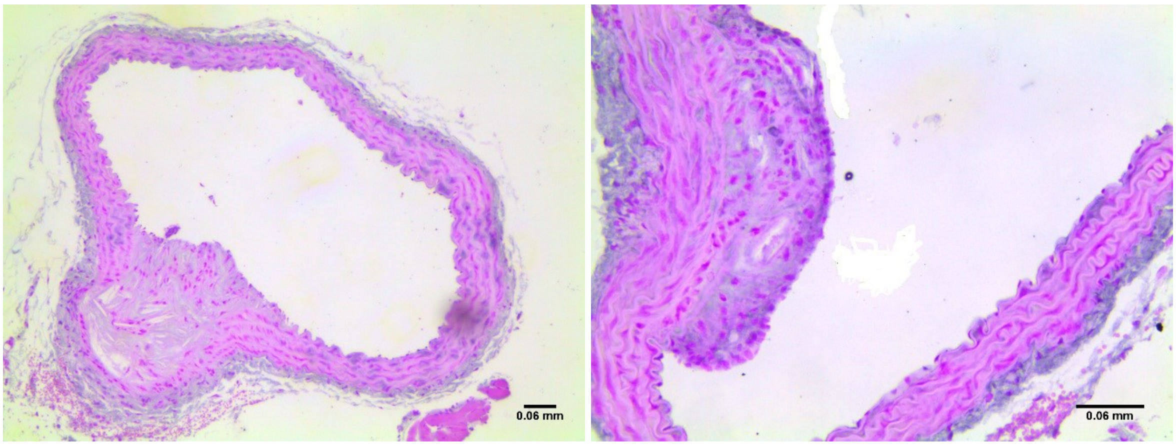

FIGURE 3.19: EXAMPLE IMAGES OF SECTIONS FROM DIFFERENT ANIMALS STAINED FOR TROPOELASTIN WITH IMMUNOHISTOCHEMISTRY, AT 10X AND 20X MAGNIFICATION RESPECTIVELY.

Analysis showed there was no significant difference between tropoelastin area in diseased and control animals, although mean signal was higher in the diseased vessels (figure 3.20).

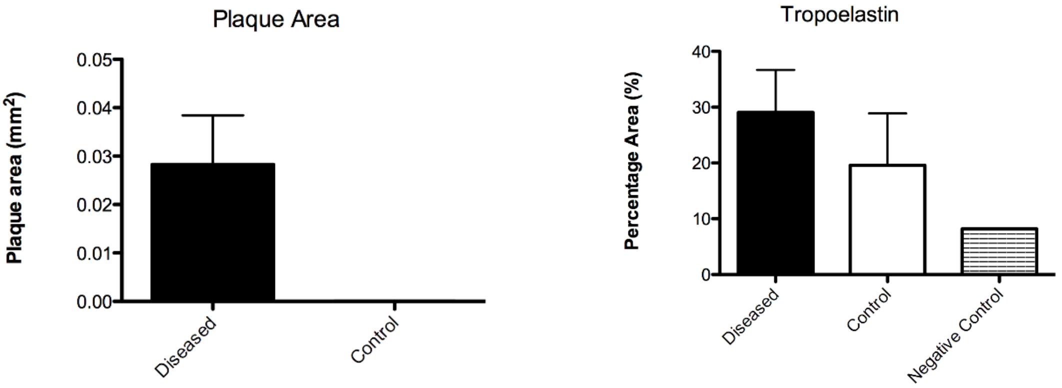

FIGURE 3.20: GRAPHS SHOWING 1) THE PLAQUE AREA IN MM^2 IN DISEASED VS CONTROL VESSELS AS MEASURED IN SECTIONS STAINED FOR ELASTIN 2) THE PERCENTAGE AREA OF SIGNAL CORRESPONDING TO TROPOELASTIN IN DISEASED VS CONTROL SECTIONS

3.5.3 MACROPHAGE STAINING

Cluster of Differentiation 68 (CD68) is a protein which is highly expressed by macrophages and monocytes, and other monocytic cells. It is generally used as a marker for macrophages and in immunohistochemistry can be used for differentiating between similar diseases. In this case, CD68 was used as a marker for macrophages irrespective of their M1 or M2 status, with the expectation that plaque would contain macrophages. The lack of specificity as a marker of class, inasmuch as it is possible to classify macrophages, means that it does not differentiate between the classically-activated macrophages which would be predominantly associated with a vulnerable plaque, and non-classically activated macrophages which would be expected in a stable plaque.

Given the propensity of macrophages to phagocytose SPIONs, it was also of interest to have an idea of the presence of macrophages in the plaques.

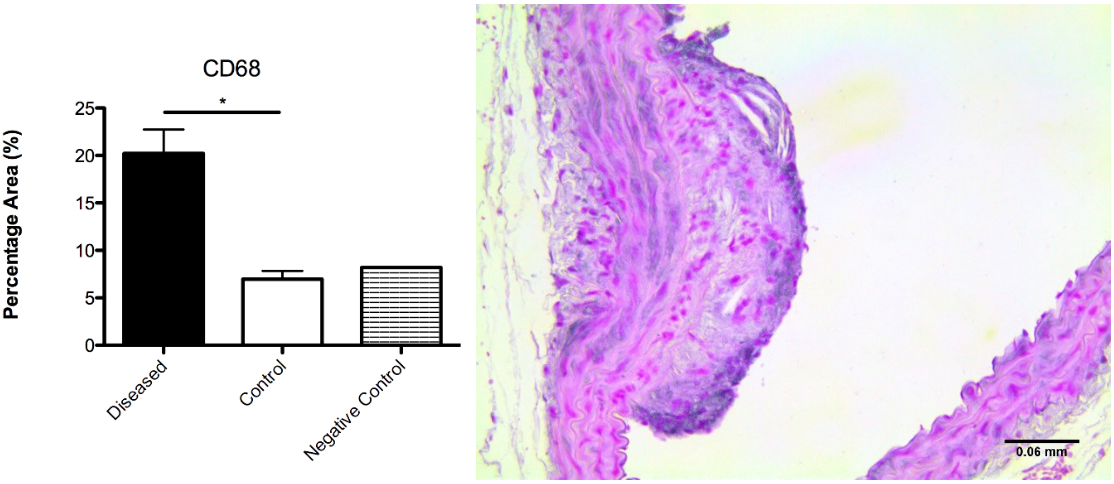

FIGURE 3.21: GRAPH SHOWING THE RELATIVE PERCENTAGE AREA OF VESSEL WITH CD68 SIGNAL IN DISEASED AND CONTROL VESSELS. AND A PLAQUE REGION STAINED FOR CD68 SHOWING MACROPHAGES IN THE PLAQUE REGION, PARTICULARLY IN THE CAP OF THE PLAQUE.

Analysis of the area of signal showed there was a significant difference between the level of CD68 expression in the diseased vessel sections compared to the control sections (p=0.0357) (Figure 3.21). The level of signal in the control vessels was comparable to the negative control, where there was no secondary antibody. This corresponds to increased macrophage activity in the diseased vessels, which is expected in plaque regions, both in the plaque itself and in surrounding endothelium where it is likely to be associated with the formation of new fatty streaks or areas of endothelial dysfunction.

3.5.4 FRACTALKINE (CX3CL1) STAINING

Although the literature indicated that CX3CL1 was a promising target for identifying vulnerable plaque due to the levels of expression identified by previous work by Cheng et. al.[22], staining for CX3CL1 to confirm expression was performed to confirm the presence of fractalkine. Analysis of the area of signal showed a significant difference between the level of fractalkine expression in the diseased vessel sections compared to control sections (p=0.0110) (figure 3.22). It also confirmed the presence of the protein and the potential validity of fractalkine as a target for atherosclerosis imaging, although it remains unclear from this work whether fractalkine expression alone is sufficient for differentiating between vulnerable and stable plaques. Examples of sections stained for CX3CL1 can be seen in figure 3.23.

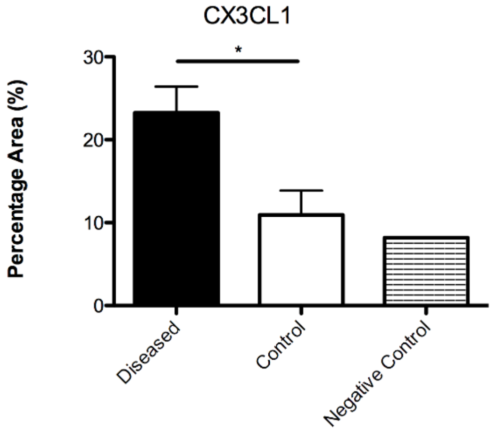

FIGURE 3.22: GRAPH SHOWING THE PERCENTAGE AREA OF SIGNAL CORRESPONDING TO CX3CL1 EXPRESSION IN DISEASED AND CONTROL VESSELS

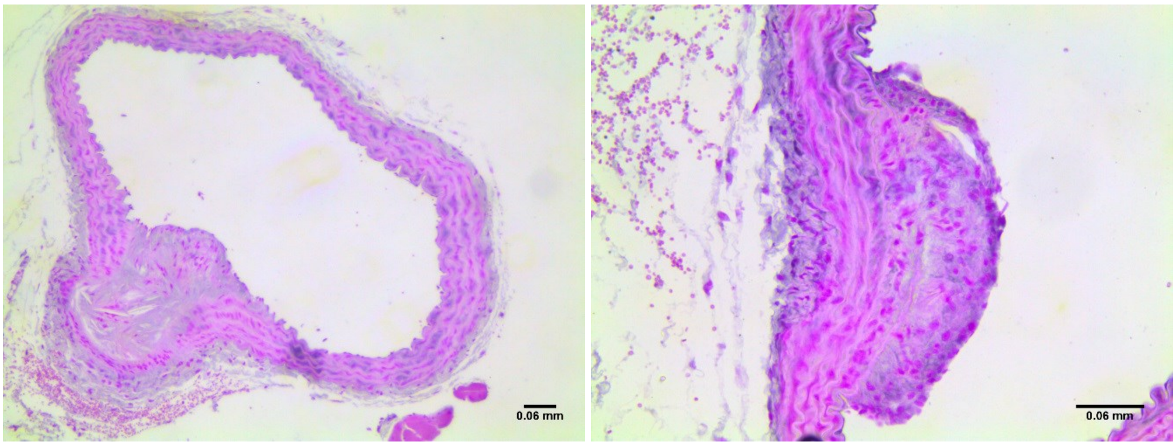

FIGURE 3.23: EXAMPLES OF SECTIONS FROM DIFFERENT ANIMALS IMMUNOHISTOCHEMICALLY STAINED FOR CX3CL1 AT 10X AND 20X MAGNIFICATION, SHOWING THE PRESENCE OF CX3CL1 IN THE AREAS OF PLAQUE.

3.5.5 Iron Staining

Staining for iron was performed using the classical Prussian Blue stain counterstained with nuclear fast red. The analysis of these images was qualitative, and where no iron was detected in the control vessels, sections of diseased vessel showed areas of Prussian blue in plaques, which may be as a result of passive targeting through the EPR effect, phagocytosis by macrophages, or active targeting through the anti-CX3CL1 antibody. Iron deposits within plaque may also be as a result of intra-plaque haemorrhage, and co-localisation with a macrophage stain might allow the differentiation from phagocytosed nanoparticles. Examples of sections stained with Prussian blue and counterstained with nuclear fast red can be seen in figure 3.24, with the blue deposits highlighted.

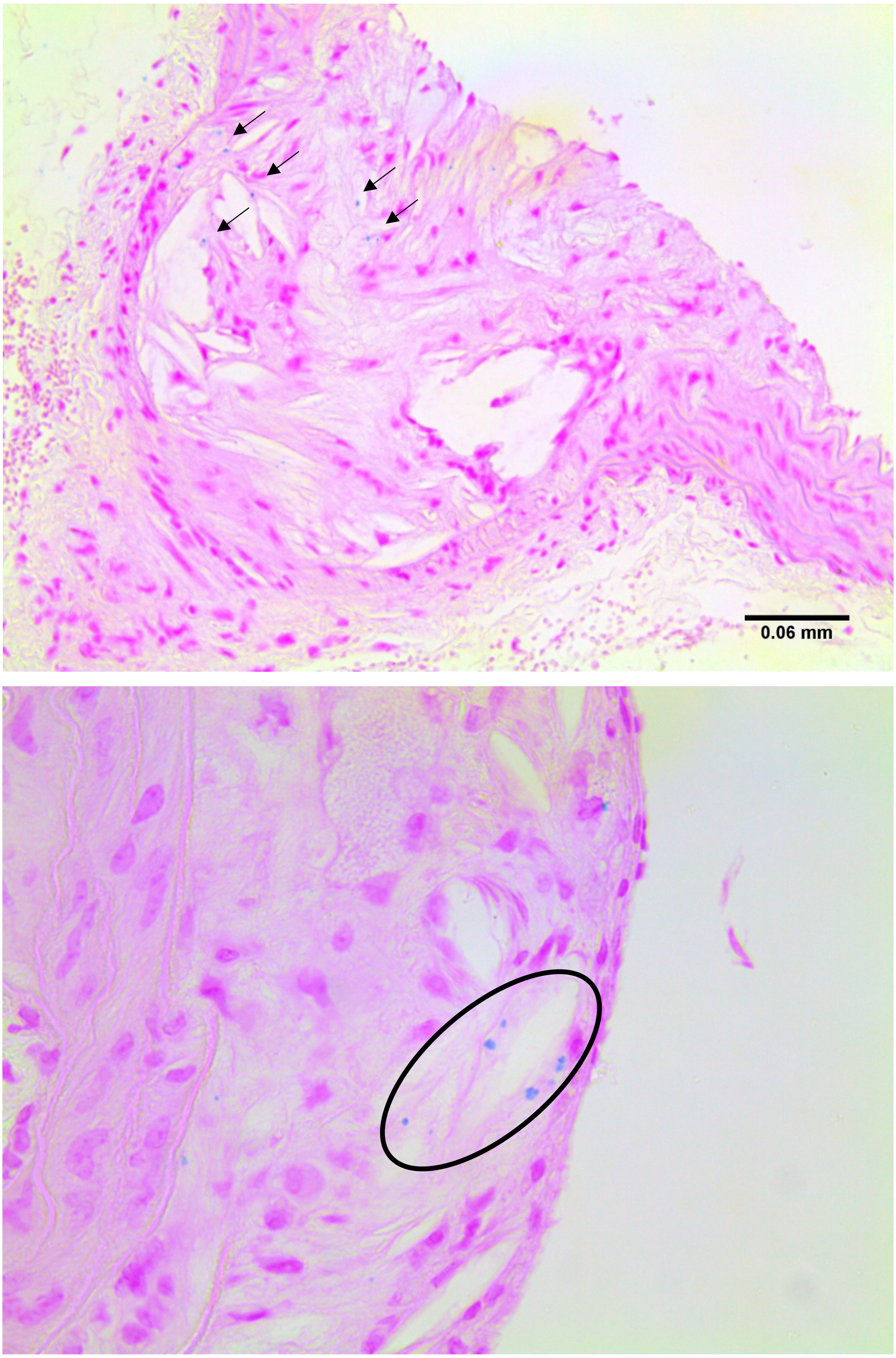

FIGURE 3.24: EXAMPLES OF SECTIONS FROM DIFFERENT PLAQUES STAINED WITH PRUSSIAN BLUE AND COUNTERSTAINED WITH NUCLEAR FAST RED, SHOWING DISTINCT BLUE DEPOSITS WITHIN THE PLAQUE, MEANING THAT IRON IS PRESENT IN THE PLAQUE REGION, EITHER AS A RESULT OF PHAGOCYTOSIS OR INTRAPLAQUE HAEMHORRAGE. THE TOP IS 20X AND THE BOTTOM IS 40X MAGNIFICATION.

3.6 CONCLUSIONS

In conclusion, the novel contrast agent designed in phase 1 demonstrated promising results *in vivo*.

The targeting antibody was coupled to the nanoparticle surface, and the presence of the protein was confirmed through the BCA assay though it was not possible to confirm whether this was through physisorption or the formation of a chemical bond. A binding study demonstrated that the targeted nanoparticles retained the ability to bind to CX3CL1 after the coupling reaction, and cell viability assays confirmed the nanoparticles to be non-toxic compared to the same concentration of free iron, even at higher concentrations of iron than would be encountered *in vivo*.

The MR imaging study was very promising, demonstrating that the uptake of SPIONs *in vivo* closely resembled that of Gd-ESMA, a commercially produced elastin-targeted gadolinium-based contrast agent which was used as a benchmark to identify regions of atherosclerotic plaque. There were significant differences in signal measured between the modified and unmodified vessels in the diseased animal model, and between the modified diseased vessel and vessels in a control animal. Unfortunately there was no significant difference between uptake above and below the plaque, so the agent was determined to be unspecific for vulnerable plaque.

The imaging results were confirmed through histology, staining for fractalkine, CD68 and iron. The iron staining did identify the presence of iron deposits in the plaque but it was not possible to determine whether these were as a result of intra-plaque haemorrhage or the phagocytosis of nanoparticles. Immunohistochemistry did confirm the presence of CX3CL1 in the plaque regions.

There are several potential explanations for the lack of specificity, but the low targeting efficiency is likely to play an important role despite the retention of the binding ability by the targeted SPIONs. This would be a valuable avenue to pursue for the further refinement of the contrast agent, in the search for greater specificity and differentiation of plaques, although this first round of studies does show that the agent has potential for plaque imaging more generally.

It is also valuable to consider whether further study in an alternative animal model may provide useful data, because although the cuff model is generally accepted, and it provides valuable certainty in differentiating plaque sites and allowing a high degree of internal control, the study might be further improved by the use of control animals which undergo sham surgeries to allow for any effects potentially arising from the procedure, and also using a disease model which is free of the cuff, even potentially the use of a non-tapered cuff. The value of a more simple animal model such as ApoE-/- on high fat diet is in the lack of cuff, where there are questions about the potential effects, both local and systemic, of placing a relatively large piece of Perspex around a vessel and what this might lead to in terms of remodelling. Some systemic effects were observed in the enlargement of the BCA which has not been seen in a comparable disease model without the cuff. This would, however, pose difficulties in differentiating between vulnerable and stable plaque when imaging *in vivo* for evaluating the contrast agent, with plaques needing to be identified and analysed post-mortem for macrophage content and other structural features in order to classify them as vulnerable or stable *ex vivo* and compare them to the MR images. This additional complexity means that while further study in a less specialised model would be an important and interesting next step, the advantage of the cuff model for this preliminary preclinical work is that it provides two known and comparable plaque areas which are vulnerable and stable respectively, and which can be confidently identified while scanning *in vivo* to assess the behaviour of a contrast agent and its ability to differentiate.

3.7 EXPERIMENTAL

3.7.1 ANTIBODY COUPLING

10 nm PMAO coated SPIONs (2 mM, 800 µl in PBS at pH 6.5) and 1-Ethyl-3-(3-dimethylaminopropyl)carbodiimide (17.5 mM, 800 µl in PBS at pH 6.5) were suspended in Phosphate Buffered Saline (pH 6.5, 1600 µl) and stirred for one hour at room temperature. N-hydroxysuccinimide (35 mM, 800µl in PBS at pH 8.7), antibody (1.8 mM, 550 µl in PBS at pH 8.7) were added to the solution along with 2 ml of PBS at pH 8.7. The solution was stirred overnight, then concentrated on a 300k mW filter in the microcentrifuge. Nanoparticles were resuspended in 250 µl of sterile saline prior to administration.

The BCA assay was performed following the protocol supplied with the kit, on the microplate scale, with incubation for an hour at room temperature. Three repeats of both the resuspended nanoparticles and the filtrate were analysed and compared to the calibration curve. Measurements were taken on a UV spectrometer.

3.7.2 BINDING STUDIES

1 µl per well of the fractalkine [RND Systems 485-MF Lot BMR31501 25 µg total dissolved in 250 µl (FW = 10,000)] added to 96-wellNunc immunobind plate and incubated in 50 µl PBS for 96h. Then blocked with 5% Bovine Serum Albumin (A2153-100G Sigma-Aldrich) in PBS (D8537-500mL Sigma-Aldrich ready-made tissue culture grade) 1 hour. Then incubated with 4 µl / well of anti-FK-SPION made up from 1 vial in 800 µl PBS, or 4 µl /well of control SPION for 48h. Then gently washed by decanting fluid and adding 100 µl of PBS. Then incubated with fresh Berlin Blue reagent [composed of a 1:1 mix of saturated potassium ferrocyanide (P9387-100G Sigma-Aldrich) and 2% hydrochloric acid (H1758-100mL Sigma-Aldrich, molecular biology grade) and absorbance read in 10nm spectrum mode from 400-1000nm on a Beckman Coulter Paradigm multi-well spectrophotometer / fluorimeter.

The optimal parameters determined from this time course were 3 hours incubation with Berlin Blue and measurement at 800 nm.

3.7.3 XTT ASSAY

Preparation of XTT working reagent:

5ml of PBS (Phosphate Buffered Saline) and 50 µl of XTT (25mg/ml) and 0.5 µl PMS (Phenazine methosulfate, 50mg/ml) was added into a clean 15ml conical centrifuge tube.

Determining Optimal Cell Density:

In a 96 well plate, 200 μl of different concentrations of RAW 264.7 cells were prepared: 20,000 10,000, 8000, 6000, 5000, 2000, 1000 and 0 cells in 10% FBS and colourless IMDM (Iscove's Modified Dulbecco's Medium). The plate was incubated overnight, and 20 μl of XTT working reagent added to the wells.

The plate was placed back into the incubator and checked every hour for colour changes. After 2 hours a change from light yellow to orange was observed, and the absorbances of each well measured on the plate reader at 450 and 540 nm.

The plate was then placed back into the incubator overnight. At 24 hours after the initial treatment with XTT, the colour had changed to an intense orange, and absorbance was again measured at 450 and 540 nm.

Cell density calibration curve was calculated and 10k cells was shown to be the optimal cell density per well.

Cell Toxicity with Metal Treatment using XTT:

In a 96 well plate each well was seeded with 200 μl of 10k RAW 264.7 cells in IMDM with 10% FBS. The plate was incubated overnight, and then treated with SPIONs at different concentrations: 0 μM, 1 μM, 10 μM and 100 μM. The plate was incubated overnight, and 20 μl of XTT reagent as prepared above was added to the wells and incubated. The absorbance was measured at 2 and 24 hours post-addition of XTT at 450 and 540 nm.

3.7.4 ANIMAL MODEL

All animal experiments complied with the Animals (Scientific Procedures) Act 1986 and were carried out under PPL 70/8482 at King's College London.

Homozygous female ApoE-/- mice (C57BL/6J background) were acquired from Charles Rivers Laboratories (Edinburgh, UK) and bred within the Behavioural Sciences Unit of the Rayne Institute. The housing and care of the animals, and all procedures in this study were performed in accordance with the guidelines and regulations of the UK home office.

At 11 weeks of age the mice were placed on high fat diet (HFD) (21% fat, 0.15% cholesterol wt/wt from LBS-Biotech) for two weeks prior to surgery. Two weeks after commencement of HFD the mice underwent surgery for the placement of a rigid polyether ketone perivascular cuff (Promolding, The Netherlands) around the left carotid. The cuff was supplied in two pieces and when assembled the lumen narrowed from 500 μm to 250 μm over 1.5 mm. The animals were kept under anaesthesia at

1.5-2.5% isoflurane and 2% O_2, with anaesthetic depth being assessed from respiratory rate, hind limb muscle tone, and pedal withdrawal reflex as previously described[5,7].

The animals then remained on HFD for a further 9 weeks before scanning and sacrifice. Animals were euthanised under Schedule 1 with an overdose of anaesthetic followed by exsanguination and flushing of the vasculature with saline before the vessel was collected.

Healthy ApoE-/- mice with no cuff and on a chow diet were used as controls.

3.7.5 IMAGING STUDIES: Gd-ESMA

Based on previous studies carried out by Makowski et. al.[18] animals were injected with 0.2 mmol/kg Gd-ESMA in 150 µl sterile saline through the tail vein. The animals were then scanned 1 hour post-injection.

In vivo vessel wall imaging was performed using a Philips Achieva MR scanner (Philips Healthcare, Best, The Netherlands) equipped with a clinical gradient system (30 mT m−1, 200 mT m−1 ms−1).

The brachiocephalic artery (BCA) and left and right carotids were imaged using a single-loop surface coil (diameter=23 mm). Mice were placed in prone position after intravenous administration of 0.2 mmol/kg Gd-ESMA (Lantheus Medical Imaging, North Billerica, MA). Anesthesia was induced with 5% and maintained with 1% to 2% isoflurane during the MRI experiments.

After a 3-dimensional gradient recalled echo scout scan, contrast-enhanced angiography images were acquired with a field of view (FOV)=30×30×8 mm, matrix=200×200, in-plane resolution=0.15×0.15x0.5 mm (reconstructed=0.10×0.10 mm), repetition time/echo time=15/6.1 ms, and flip angle=40°. The maximum intensity projection images were used to plan the subsequent delayed-enhancement (DE) and T1 mapping scans. A 2-dimensional Look-Locker sequence was acquired using the following parameters: FOV=30×30 mm, matrix=80×80, in-plane resolution=0.38×0.38x2 mm, repetition time/echo time=19/8.6 ms, repetition time between subsequent inversion recovery pulses=1000 ms, and flip angle=10°. An inversion recovery 3-dimensional fast gradient echo sequence was acquired with FOV=30×30×8 mm, matrix=304×304, in-plane resolution=0.1×0.1x0.5 mm, repetition time/echo time=28/8 ms, repetition time between subsequent inversion recovery pulses=1000 ms, and flip angle=30°. T1 mapping was performed with the same sequence employed for the aorta. The acquisition parameters were as follows: FOV=36×22×8 mm, matrix=192×102, in-plane resolution=0.18×0.22x0.5 mm, slices=16, repetition time/echo time=9.6/4.9 ms, flip angle=10°.

3.7.6 IMAGING STUDIES: SPIONS

Animals were injected with 150 μl 6 mM [Fe] SPIONs in sterile saline through the tail vein. The animals were then scanned 24 hours post-injection.

The imaging protocols were based on previous experiments by Makowski et. al.[20] and were carried out on a Phillips 3T Achieva scanner (Philips Healthcare, Best, The Netherlands) equipped with a clinical gradient system (30 mT m−1, 200 mT m−1 ms−1) as before.

The brachiocephalic artery (BCA) and left and right carotids were imaged using a single-loop surface coil (diameter=23 mm). Mice were placed in prone position. Anesthesia was induced with 5% and maintained with 1% to 2% isoflurane during the MRI experiments.

After a 3-dimensional gradient recalled echo scout scan, contrast-enhanced angiography images were acquired with a field of view (FOV)=30×30×8 mm, matrix=200×200, in-plane resolution=0.15×0.15x0.5 mm (reconstructed=0.10×0.10 mm), repetition time/echo time=15/6.1 ms, and flip angle=40°. The maximum intensity projection images were used to plan the subsequent T2*-weighted 3D gradient echo scan. ECG-triggering was not used, and a T2*-weighted 3D gradient echo data set was acquired with FOV=16x16x8 ; matrix= 176x176; in-plane spatial resolution=0.12x0.12 mm ; slice thickness=0.5 mm; TR/TE= 37.88/7.32 ms ;and flip angle=25˚.

3.7.7 EMBEDDING OF TISSUE IN PARAFFIN

Tissue was embedded in paraffin using the following method:

- Tissue was placed in 70% ethanol for 1 hour
- Tissue was placed in 96% ethanol for 2 hours
- Tissue was placed in 100% ethanol for 2 hours
- Tissue was placed in xylene for 1.5 hours
- Tissue was placed in paraffin for 1.5 hours and then embedded in a block

3.7.8 DEPARAFFINISATION OF SLIDES

Slides were deparaffinised for all stainings by passing through a gradient as follows:

- 10 minutes in xylene
- 10 minutes in 100% ethanol
- 5 minutes in 96% ethanol
- 5 minutes in 70% ethanol
- 5 minutes in deionised water

3.7.9 TRICHROME STAINING

Deparaffinised slides were incubated in Bouin's solution in an oven at 60 ˚C for 15 minutes. Slides were then washed under running water to cool and remove excess yellow staining. Slides were incubated in Weigert's Iron Haematoxylin Solution for 5 minutes. Slides were washed under running water for 5 minutes and rinsed in deionized water. Slides were incubated in Biebrich Scarlet-Acid Fucshin for 5 minutes and then rinsed in deionised water. Slides were placed in working phosphotungstic/phosphomolybdic acid for 5 minutes, and then into aniline blue solution for 5 minutes. Slides were placed in 1% acetic acid for 2 minutes and then finally dehydrated through gradient of ethanol, cleared in xylene, and mounted.

3.7.10 ELASTIN STAINING

Deparaffinised slides were incubated in working elastic stain solution for 10 minutes and rinsed in deionized water. Slides were then placed in ferric chloride solution for 22 seconds, rinsed under running water and checked under the microscope. Slides were rinsed in 96% ethanol to remove excess iodine, then rinsed in deionized water. Slides were incubated in van Gieson solution for 1-3 minutes. Finally, slides were dehydrated through a gradient of ethanol, cleared in xylene, and mounted.

3.7.11 PRUSSIAN BLUE STAINING

20% aqueous solution of hydrochloric acid (20 ml conc. HCl, 80 ml water) and 10% potassium cyanoferrate (10 g, 100 ml water) were prepared and mixed fresh before staining. Slides were immersed in the solution for 20 minutes, then washed in deionized water three times before counterstaining with nuclear fast red for 5 minutes. Finally, slides were dehydrated through a gradient of ethanol, cleared in xylene, and mounted.

3.7.12 TROPOELASTIN STAINING

Endogenous peroxidase was inhibited by incubation of the slides in 3% oxygenated water and methanol for 10 minutes. Slides were then washed in deionized water for 10 minutes. Antigen retrieval was performed by boiling the samples for 2 minutes at 110 ˚C in citrate buffer in a pressurized antigen retrieval unit and then allowed to cool. Samples were washed with PBS for 3 minutes, and blocking was performed for 1 hour at room temperature with 10% donkey serum in PBS. Incubation with the primary antibody was carried out overnight at 4 ˚C with anti-tropoelastin diluted 1:100 in PBS 2% normal donkey serum. Samples were allowed to temper at room temperature for 1 hour, then slides were washed twice in PBS for 20 minutes. Slides were incubated with anti-rabbit HRP polymer for 45 minutes at room temperature, then washed 3 times in PBS for 5 minutes.

Slides were revealed with Vector SG Peroxidase substrate for 10 minutes at room temperature
PBS (5 ml), Chromogen (75 µl), Hydrogen peroxide (120 µl).

Samples were washed twice in PBS for 5 minutes, before counterstaining with nuclear fast red for 5 minutes. Slides were washed with deionized water, then finally dehydrated through a gradient of ethanol, cleared in xylene, and mounted.

3.7.13 MACROPHAGE STAINING

Endogenous peroxidase was inhibited by incubation of the slides in 3% oxygenated water and methanol for 10 minutes. Slides were then washed in deionized water for 10 minutes. Antigen retrieval was performed by boiling the samples for 2 minutes at 110 ˚C in citrate buffer in a pressurized antigen retrieval unit and then allowed to cool. Samples were washed with PBS for 3 minutes, and blocking was performed for 1 hour at room temperature with 10% donkey serum in PBS. Incubation with the primary antibody was carried out overnight at 4 ˚C with anti-CD68 diluted 1:100 in PBS 2% normal donkey serum. Samples were allowed to temper at room temperature for 1 hour, then slides were washed twice in PBS for 20 minutes. Slides were incubated with anti-rabbit HRP polymer for 45 minutes at room temperature, then washed 3 times in PBS for 5 minutes.

Slides were revealed with Vector SG Peroxidase substrate for 10 minutes at room temperature
PBS (5 ml), Chromogen (75 µl), Hydrogen peroxide (120 µl).

Samples were washed twice in PBS for 5 minutes, before counterstaining with nuclear fast red for 5 minutes. Slides were washed with deionized water, then finally dehydrated through a gradient of ethanol, cleared in xylene, and mounted.

3.7.14 CX3CL1 STAINING

Endogenous peroxidase was inhibited by incubation of the slides in 3% oxygenated water and methanol for 10 minutes. Slides were then washed in deionized water for 10 minutes. Antigen retrieval was performed by boiling the samples for 2 minutes at 110 ˚C in citrate buffer in a pressurized antigen retrieval unit and then allowed to cool. Samples were washed with PBS for 3 minutes, and blocking was performed for 1 hour at room temperature with 10% donkey serum in PBS. Incubation with the primary antibody was carried out overnight at 4 ˚C with anti-CX3CL1 diluted 1:100 in PBS 2% normal donkey serum. Samples were allowed to temper at room temperature for 1 hour, then slides were washed twice in PBS for 20 minutes. Slides were incubated with anti-rabbit HRP polymer for 45 minutes at room temperature, then washed 3 times in PBS for 5 minutes.

Slides were revealed with Vector SG Peroxidase substrate for 10 minutes at room temperature
PBS (5 ml), Chromogen (75 µl), Hydrogen peroxide (120 µl).

Samples were washed twice in PBS for 5 minutes, before counterstaining with nuclear fast red for 5 minutes. Slides were washed with deionized water, then finally dehydrated through a gradient of ethanol, cleared in xylene, and mounted.

3.8 REFERENCES

1 A. Millon, E. Canet-Soulas, L. Boussel, Z. Fayad and P. Douek, *Vascular*, 2014, **22**, 221–237.

2 A. Daugherty, A. R. Tall, M. J. A. P. Daemen, E. Falk, E. A. Fisher, G. García-Cardeña, A. J. Lusis, A. P. Owens, M. E. Rosenfeld and R. Virmani, *Circ. Res.*, 2017, **121**, e53–e79.

3 G. Lo Sasso, W. K. Schlage, S. Boué, E. Veljkovic, M. C. Peitsch and J. Hoeng, *J. Transl. Med.*, 2016, **14**, 146.

4 X.-F. Leong, C.-Y. Ng and K. Jaarin, *Biomed Res. Int.*, 2015, **2015**, 1–11.

5 R. Krams, M. T. Kuhlmann, P. C. Evans, K. Nicolay, M. Schäfers, S. Hermann, G. J. Strijkers, S. Cuhlmann and I. Hoppe, *J. Vis. Exp.*, 2012, 1–6.

6 R. M. Pedrigi, R. De Silva, S. M. Bovens, V. V. Mehta, E. Petretto and R. Krams, *Arterioscler. Thromb. Vasc. Biol.*, 2014, **34**, 2224–2231.

7 Z. Mohri, E. M. Rowland, L. A. Clarke, A. De Luca, V. Peiffer, R. Krams, S. J. Sherwin and P. D. Weinberg, *PLoS One*, 2014, **9**, 1–22.

8 J. Fan, S. Kitajima, T. Watanabe, J. Xu, J. Zhang, E. Liu and Y. E. Chen, *Pharmacol. Ther.*, 2015, **0**, 104–119.

9 Y. Lee, V. Laxton, H. Lin, Y. Chan, S. Fitzgerald‐Smith, T. L. O. To, B. Yan, T. Liu and G. Tse, *Biomed. Reports*, 2017, 259–266.

10 K. Van Der Heiden, A. Hoogendoorn, M. J. Daemen and F. J. H. Gijsen, *Thromb Haemost*, 2016, **115**, 501–508.

11 A. Phinikaridou, K. J. Hallock, Y. Qiao and J. A. Hamilton, *J. Lipid Res.*, 2009, **50**, 787–797.

12 C. B. Poulsen, R. M. Pedrigi, V. V. Mehta, A. Post, N. Pareek, N. R. Holm, D. Kilic, M. El-Bahnasawi, M. M. Bjørklund, N. P. Andersen, A. K. Grøndal, A. Nachiappan, N. Foin, J. E. R. Davies, C. Di Mario, H. E. Bøtker, J. F. Bentzon, E. Falk, R. Krams and R. de Silva, *J. Am. Coll. Cardiol.*, 2015, **65**, A1927.

13 N. Chopin, X. Guillory, P. Weiss, J. Bideau and S. Colliec-Jouault, *Curr. Org. Chem.*, 2014, **18**, 867–895.

14 E. Lambidis, T. Homma, N. Long and R. Krams, 2013.

15 S. A. McCarthy, G. L. Davies and Y. K. Gun’ko, *Nat. Protoc.*, 2012, **7**, 1677–1693.

16 K. L. Cox, V. Devanarayan, A. Kriauciunas, J. Manetta, C. Montrose and S. Sittampalam, *Immunoassay Methods*, Eli Lilly & Company and the National Center for Advancing Translational Sciences, Bethesda (MD).

17 R. J. Evans, B. Lavin, A. Phinikaridou, K. Y. Chooi, Z. Mohri, E. Wong, J. J. Boyle, R. Krams, R. Botnar and N. J. Long, *Nanotheranostics*, 2020, **4**, 184–194.18

18 M. R. Makowski, A. J. Wiethoff, U. Blume, F. Cuello, A. Warley, C. H. P. Jansen, E. Nagel, R. Razavi, D. C. Onthank, R. R. Cesati, M. S. Marber, T. Schaeffter, A. Smith, S. P. Robinson and R. M. Botnar, *Nat. Med.*, 2011, **17**, 383–389.

19 M. Wildgruber, I. Bielicki, M. Aichler, K. Kosanke, A. Feuchtinger, M. Settles, D. C. Onthank, R. R. Cesati, S. P. Robinson, A. M. Huber, E. J. Rummeny, A. K. Walch and R. M. Botnar, *Circ. Cardiovasc. Imaging*, 2014, **7**, 321–329.

20 M. R. Makowski, G. Varma, A. J. Wiethoff, A. Smith, K. Mattock, C. H. P. Jansen, A. Warley, M. Taupitz, T. Schaeffter and R. M. Botnar, *Circ. Cardiovasc. Imaging*, 2011, **4**, 295–303.

21 A. Phinikaridou, S. Lacerda, B. Lavin, M. E. Andia, A. Smith, P. Saha and R. M. Botnar, *Circ. Cardiovasc. Imaging*, 2018, **11**, 1–15.

22 C. Cheng, D. Tempel, R. van Haperen, H. C. de Boer, D. Segers, M. Huisman, A. J. van Zonneveld, P. J. M. Leenen, A. van der Steen, P. W. Serruys, R. de Crom and R. Krams, *J. Clin. Invest.*, 2007, **117**, 616–626.

Chapter 4

Development of Multi-Modal Imaging Probes

4.1 INTRODUCTION

4.1.1 CORE-SHELL NANOPARTICLES

Core-shell structures in nanoparticles are a well-established way to combine and enhance material properties. Core-shell structures can be synthesised through top-down or bottom-up approaches, and can involve multiple materials including iron oxide, gold, silica, and other metals or metallic materials for upconversion in fluorescence or quantum dots. A very comprehensive review of core-shell nanoparticles by Ghosh et. al. is an exhaustive list of the many and varied combinations of core-shell materials which have been documented in the literature[1].

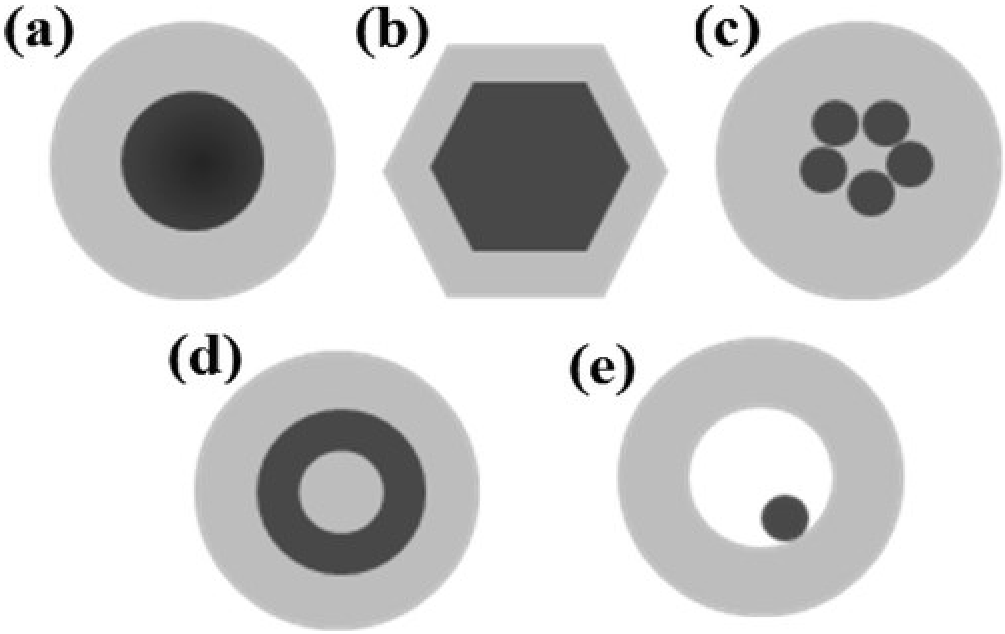

FIGURE 4.1: AN ILLUSTRATION OF THE RANGE OF CORE-SHELL NANOPARTICLE STRUCTURES WHICH CAN BE SYNTHESISED, TAKEN FROM GHOSH ET. AL.[1] A) SPHERICAL CORE-SHELL NANOPARTICLES; B) HEXAGONAL CORE-SHELL NANOPARTICLES; C) MULTIPLE SMALL CORE MATERIALS IN SINGLE SHELL; D) NANOMATRYUSHKA MATERIAL; E) MOVABLE CORE WITHIN HOLLOW SHELL MATERIAL.

There has been a lot of interest in the development of Fe_3O_4@Au core-shell nanoparticles for biomedical applications. Both iron and gold are biocompatible metals with valuable properties for biotechnology, and the combination of the two can be very powerful, particularly in the area of medical imaging[2–4].

Gold is a dense element which can generate contrast in CT and OCT by attenuating X-rays or reflecting coherent light respectively. It also has a surface plasmon resonance which can enhance optical imaging. The introduction of a gold shell on the surface of iron oxide also opens up other potential ligand libraries based on the strong affinity between gold and sulfur. There have also been studies showing that gold-coated iron oxide nanoparticles display both T_1 and T_2 relaxivity[5].

The value of Fe_3O_4@Au core-shell nanoparticles, particularly in the context of this project, is several-fold. OCT is the current gold standard for imaging atherosclerosis in a clinical context, and the addition of a gold shell to the contrast agent designed in phase 1 would allow its validation through OCT. This would be particularly useful in trying to translate the probe into the clinic, as well as providing valuable data regarding the probe design and behaviour. The ability of Fe_3O_4@Au core-shell nanoparticles to affect both T_1 and T_2 relaxivity would also be an asset in the path towards clinical translation. T_2-weighted probes have not achieved widespread use in the clinic, and this is primarily due to the negative contrast which is much harder to detect. If the introduction of a gold shell changes the ratio of T_1 to T_2 relaxivity to enable the probe to behave as a dual-modal agent, the T_1 contrast would make it more appealing. Gold also further widens the library of potential surface ligands for the further optimisation of the probe, and may well improve the longevity of the probe *in vivo* due to its biocompatibility and inert nature. Where iron is a bioessential element, gold is not, and this may slow the break down of the nanoparticles, whilst also not posing any concerns around toxicity. The applications of gold in biomedical technologies are further discussed in section 4.1.2.

4.1.1.1 JANUS NANOPARTICLES

Janus particles are so named after the two-faced Roman god who supposedly looked back at the old year and forward to the new year at the same time. The term refers to nanomaterials with two faces of opposing or otherwise different properties or materials. Most commonly the faces are polar and apolar, or hydrophilic and hydrophobic, giving the nanoparticles interesting surfactant properties. Janus particles are still very much an emerging field but they show tremendous potential across a whole range of areas, including theranostics and drug delivery[6], particularly through their applications in Pickering emulsions[7].

Janus particles can be separated using various classification methods, but are most usually grouped by their synthetic approach: bottom-up, masking, and controlled phase separation. Some excellent reviews of Janus materials which go into the field in more depth can be found from Yong and Chen[8], Lattauda and Hatton[9], and Tran et. al.[6]. An illustration of the approaches for synthesising Janus nanoparticles can be found below in figure 4.2, taken from Lattauda and Hatton[9].

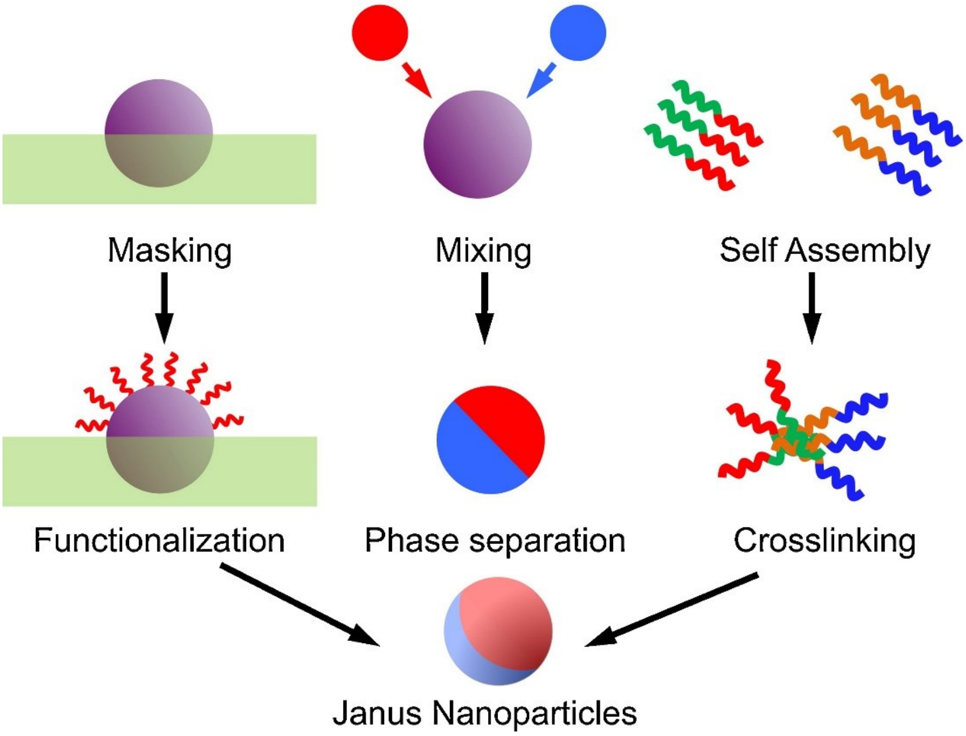

FIGURE 4.2: SYNTHETIC APPROACHES TO THE SYNTHESIS OF JANUS NANOPARTICLES, TAKEN FROM LATTUADA AND HATTON[9].

4.1.2 THE USE OF GOLD IN BIOMEDICAL APPLICATIONS

Gold has many biomedical applications, including use as implants, particularly in dentistry[10]. Gold nanoparticles have theranostic potential, and are particularly useful as imaging probes across multiple imaging modalities. Their applications in CT and OCT were discussed in the introduction, and their uses in optical imaging are further discussed here. Gold nanoparticles can be functionalised with targeting moieties, drugs, antibodies and other constructs much like any other nanoparticle, and they also have photothermal applications which are particularly valuable in cancer treatment. An excellent review of the applications of gold nanoparticles in biology and medicine was produced by Giljohann et. al.[11].

4.1.2.1 SURFACE PLASMON RESONANCE AND OPTICAL IMAGING

Quantum dots, including gold nanoparticles, behave much like multi-electron artificial atoms, giving them unique optical and chemical properties. Surface plasmon resonance is a small particle effect which is not observed in bulk material or individual atoms, and results from the interaction of the electrons in the conduction band with an electromagnetic field. Many metals have spectrally-selective resonances but most lie towards the ultraviolet. However, the noble metals, particularly gold and silver, but also to a certain extent, copper, have a strong surface plasmon resonance which falls in the visible spectrum. The resonance frequency of the surface plasmon resonance is affected by the size, shape, and environment of the nanoparticle among other things. An excellent explanation of the theory and applications of surface plasmon resonance can be found by Ghosh and Pal[12]. The surface plasmon resonance itself is the interaction of an oscillating electromagnetic field with the conduction band electrons of the small particle, resulting in the induction of a dipole which then continues to oscillate in phase with the light. This is illustrated in figure 4.3.

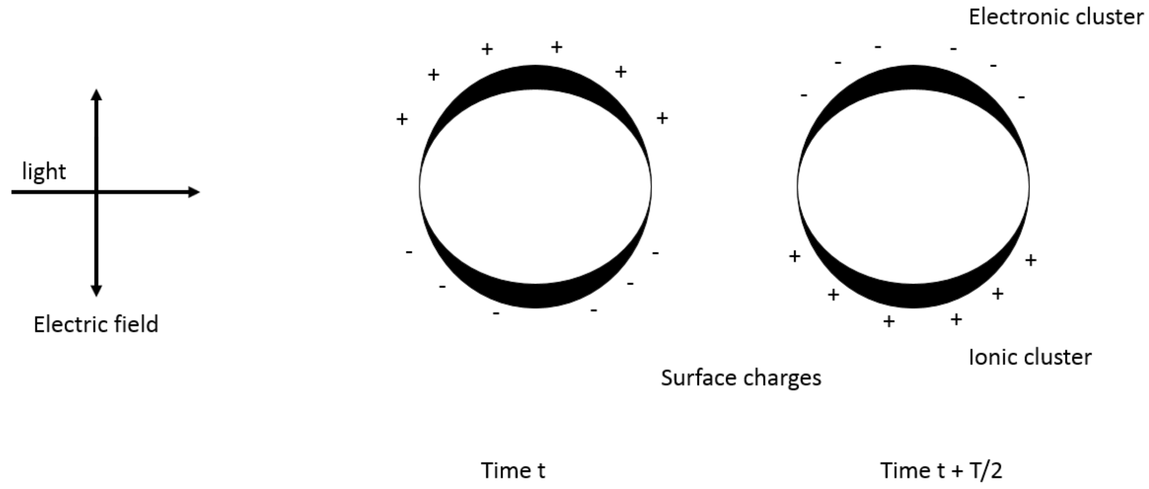

FIGURE 4.3: AN ILLUSTRATION OF THE CREATION OF THE SURFACE PLASMON THROUGH INTRODUCTION OF ELECTROMAGNETIC RADIATION WITH THE METAL PARTICLE, INDUCING A DIPOLE WHICH OSCILLATES IN PHASE WITH THE ONCOMING LIGHT. MODIFIED WITH PERMISSION FROM GHOSH AND PAL, CHEM. REV. 2007, 107, 11, 4797-4862. COPYRIGHT 2007, AMERICAN CHEMICAL SOCIETY.

The resonance frequency is determined largely by the relationship of the particle radius to the wavelength of light. This is illustrated below in figure 4.4, showing a range of particle sizes and the resultant colours of gold particles in solution.

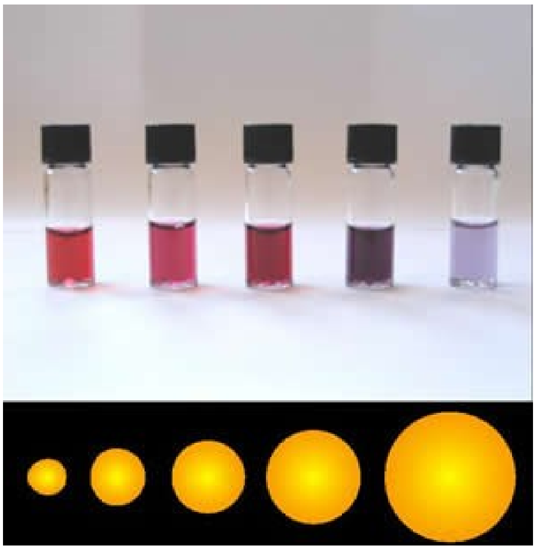

FIGURE 4.4: A SELECTION OF GOLD NANOPARTICLES AT DIFFERENT SIZES SHOWING SURFACE PLASMON RESONANCE AT DIFFERENT WAVELENGTHS (ALEKSANDER KONDINSKI, WIKIMEDIA COMMONS, CC BY-SA 4.0).

This behaviour can be particularly useful for optical imaging. Optical imaging is, for the most part, not practical *in vivo* due to the absorbance of wavelengths by tissue, however there is a window in the near infrared region which allows for light to pass through tissue. Optical imaging is still primarily used for superficial applications, for example during surgery to detect cancer cells, or in *ex vivo* samples. The well-defined wavelengths of gold nanoparticle quantum dots, and their lack of photobleaching means that they have advantages over many organic fluorophores. Gold is also a biocompatible metal, particularly compared to other materials often used in more traditional quantum dots such as cadmium, which is toxic, or zinc which is bioessential.

Surface plasmon resonance can also be exploited to enhance organic fluorophores for purposes such as Förster Resonance Energy Transfer (FRET) which acts as a molecular sensor[13], or even a molecular ruler in some cases. It is also responsible for the photothermal applications mentioned briefly in 4.1.2, where excitation with defined wavelengths causes local heating of tissue by exciting gold nanoparticles *in situ*[2,14,15]. This is particularly applicable in cancer treatment and has parallels with magnetic hyperthermia treatments with SPIONs which use radio waves for excitation.

Gold nanoparticles are therefore very useful in optical imaging, both in their own right as quantum dots, and as enhancers for more traditional fluorophores.

AIMS OF THE CHAPTER

This chapter addresses the final aim presented in section 1.4 of the thesis:

- To carry out a second phase of nanoparticle development, building on the lead candidate identified in phase one, moving towards the synthesis of a multi-modal nanoparticle contrast agent.

It discusses different approaches for the introduction of a gold shell on the surface of the iron oxide probe, and the selection of a range of surface ligands. It also presents the characterisation data and uses these data to draw conclusions about the potential of the probe and further development.

4.2 COMPARISON OF DIFFERENT SYNTHETIC ROUTES

The majority of methods to introduce a gold metallic shell onto iron oxide nanoparticles use the reduction of hydrogen tetrachloroaurate either through thermal or chemical means. The decision was made to test both reduction methods and compare their efficacy in introducing a gold shell onto the surface of the iron oxide. The thermal reduction was performed by boiling a solution of hydrogen tetrachloroaurate and adding a solution of 10 nm iron oxide nanoparticles coated in oleic acid and oleylamine, encapsulated in PMAO (see chapter 2). Although the initial method used uncoated iron oxide synthesised by co-precipitation, the decision was made to take forward a solution of nanoparticles as prepared in chapter 2 to build on the previous work.

Although a range of reducing agents are discussed in the literature, hydroxylamine hydrochloride[16] was selected primarily due to its easier handling and compatibility with aqueous chemistry compared to sodium borohydride[17,18].

In the thermal reduction approach, the solution of hydrogen tetrachloroaurate was pale yellow. Upon addition of the SPIONs the solution took on a pale brown tinge, but within the space of five minutes turned wine red. In the subsequent reaction with homocysteine, the solution instead turned purple. Upon extraction, filtration, and storage, the citrate and homocysteine coated particles were purple and blue respectively. The literature had indicated that a colour change would be expected, and that brown or black to red was indicative of a successful gold-coating reaction, see figures 4.5 and 4.7.

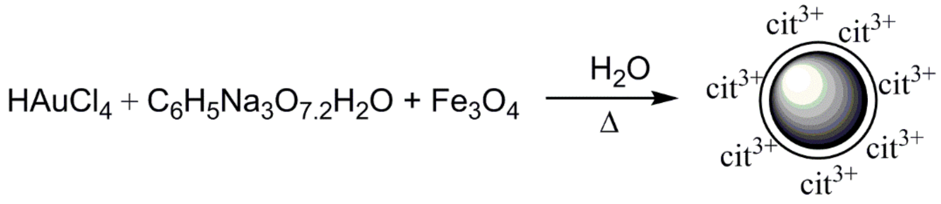

FIGURE 4.5: SCHEME SHOWING THE THERMAL REDUCTION APPROACH FOR THE SYNTHESIS OF CITRATE COATED Fe_3O_4@Au.

The initial conditions for chemical reduction were based on research into the literature which indicated that hydroxylamine hydrochloride was an appropriate reducing agent for hydrogen tetrachloroaurate[19,20], but that it might have longer reduction times than other potential reducing agents[20]. The first attempt also did not include any surface ligands in the solution, and although a colour change was observed from pale yellow to pale pink, which might have indicated at least partial success in the introduction of the gold shell it was not as marked as the thermal reduction and given that the product was expected to be identical, a return to the literature was made to research potential alternative conditions. A second attempt was made using the initial conditions but with the addition of sodium citrate solution (similarly to the thermal reduction conditions) to provide stabilising surface ligands for the gold coated particles. After stirring overnight it became evident that this reaction was unsuccessful despite an initial promising colour change from pale yellow to black (as observed in the thermal reduction, subsequently followed by shifting from black to red). After 20 hours the solution was pale yellow and the iron had crashed out of solution and was instead magnetically attracted to the stirrer bar.

Several papers which discussed the use of hydroxylamine hydrochloride used it in tandem with tetramethylammonium hydroxide as a base[21,22]. There had been no mention of base in the previous paper used for determining the potential reaction conditions, and thus on the basis of a second literature search, an alternative set of conditions was identified which also included citrate in the reaction mixture for stabilisation of the particles. This second set of conditions involving a dilute base solution was much more successful and did result in a colour change of the solution overnight to blue, suggesting that there was a difference in the thickness of the gold shell deposited compared to that resulting from the thermal approach. The ligand exchange was carried out under thermal conditions, and where the thermally coated particles changed from purple to blue on the addition of cysteine, there was no colour change in the chemically reduced solution, see figures 4.6 and 4.7.

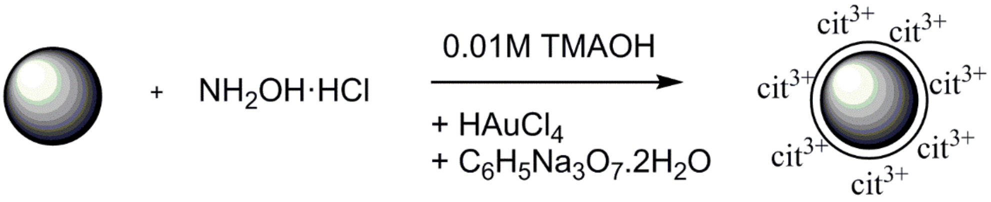

FIGURE 4.6: SCHEME SHOWING THE CHEMICAL REDUCTION OF HYDROGEN TETRACHLOROAURATE ONTO THE SURFACE OF SPIONS FOR CITRATE STABILISED Fe_3O_4@Au.

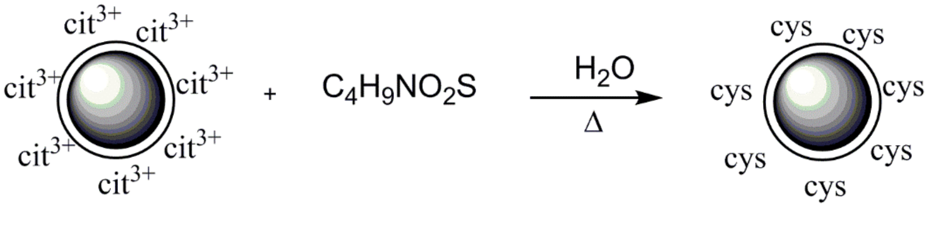

FIGURE 4.7: SCHEME SHOWING THE LIGAND EXCHANGE BETWEEN CITRATE AND HOMOCYSTEINE ON THE SURFACE OF Fe_3O_4@Au.

The approach for the synthesis of the hydrophobic gold-coated particles which could in turn be encapsulated in PMAO to provide a counterpoint to the contrast agent synthesised in chapter 2 was, by necessity, different to those used for the hydrophilic particles above. There were several approaches which used oleylamine to chemically reduce the hydrogen tetrachloroaurate *in situ*[23], however several attempts were made with oleylamine as the reducing agent which proved unsuccessful, even with oleylamine in excess. Instead, a procedure was used which was very similar to that used for the initial synthesis of the iron oxide nanoparticles in chapter 2, where the reduction was through a combination of 1,2-hexadecanediol, oleylamine, and thermal reduction[24–26]. This proved successful, with a wine red solution being achieved after 1.5 hours heating. The particles were cooled, precipitated with ethanol and centrifugation much like chapter 2, and dried under vacuum. Approximately 2 mg were then taken forward into the encapsulation with PMAO, in a direct parallel to the approach documented in chapter 2. The encapsulated particles were hydrolysed and then recovered through filteration. The filtration resulted in the removal of many large aggregates, however a pale pink-purple solution was recovered which seemed to remain stable on bench top where precipitation was observed in the chemically-reduced particles coated with citrate or homocysteine as discussed above. See figure 4.8 for the reaction scheme.

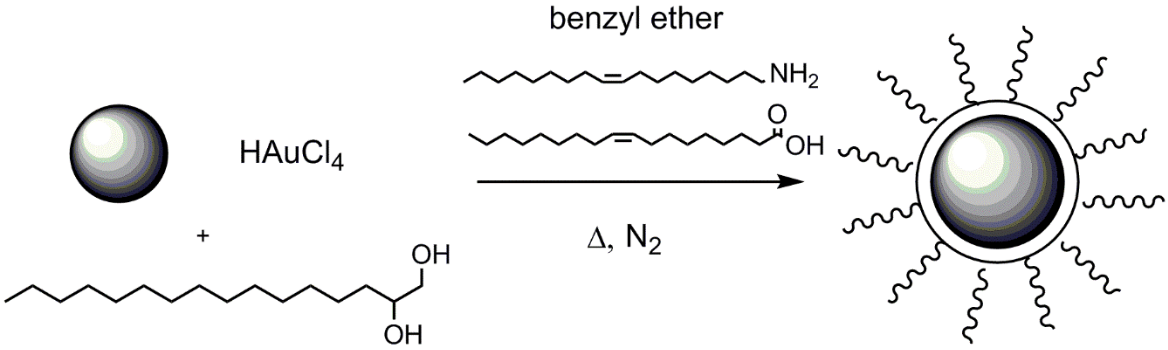

FIGURE 4.8: SCHEME SHOWING THE SYNTHESIS OF HYDROPHOBIC GOLD-COATED IRON OXIDE NANOPARTICLES, WITH HYDROGEN TETRACHLOROAURATE, 1,2-HEXADECANEDIOL, OLEYLAMINE AND OLEIC ACID.

4.3 EVALUATION OF TEM DATA

TEM was an invaluable tool for evaluating the introduction of the gold shell. Visual inspection of the solutions suggested that the thermal reduction approach had been more successful than the chemical approach. The TEM images support this, with large flower-shaped aggregates visible in the chemically-reduced samples, and limited-to-no aggregation visible in the thermally-reduced samples. The aggregation associated with the chemical reduction approach would need to be overcome in future development of this method. On the whole the TEM measurements showed a narrow size distribution, even after ligand exchange. This is an important consideration for potential clinical applications, since licensing requires probes to conform to narrow standards of characterisation for safety reasons. The particles also retain some degree of the irregular faceting from the original synthesis of the SPIONs, which will enhance T_2 relaxivity.

4.3.1 THERMAL REDUCTION

Both the citrate- and cysteine-stabilised thermally-reduced particles show similar diameters to the iron oxide cores which were used in the synthesis, with an increase between the citrate-coated and cysteine-coated particles (see figures 4.9-4.11) which is likely due to the slightly longer reaction time resulting in the reduction of more gold *in situ* and a thicker gold layer. The colour of the solution was likely also affected by the change in surface ligand affecting the wavelength of the surface plasmon resonance, however the colour change also confirmed the ligand exchange. No corresponding colour change was observed in the ligand exchange of the chemically-reduced particles. It is possible that the colour change observed in the thermally-reduced particles arises from the formation of gold nanoparticles in solution alongside the iron oxide rather than the reduction of the gold onto the surface. It is difficult to characterise this with any certainty, though the increase in diameter for the thermally-reduced particles coated with homocysteine relative to the parent particles. might support the formation of a shell. The similarity in diameter to the parent particles for the citrate-coated ones makes it difficult to conclude that a shell is likely to have formed (figure 4.9).

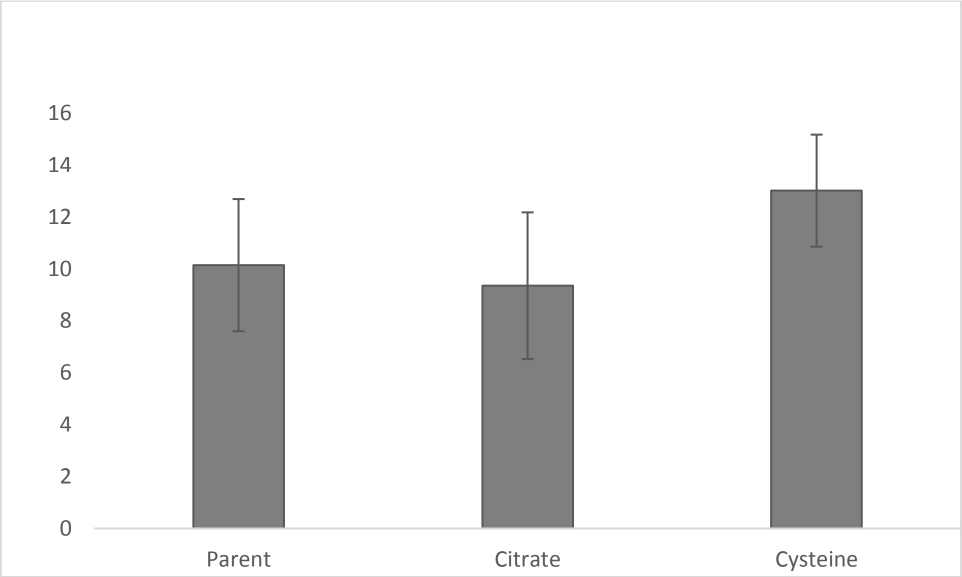

FIGURE 4.9: GRAPH SHOWING THE MEAN DIAMETERS OF GOLD-COATED IRON OXIDE NANOPARTICLES STABILISED WITH CITRATE OR HOMOCYSTEINE COMPARED TO THE PARENT PARTICLE. THE ERROR BARS SHOW THE STANDARD DEVIATION OF DIAMETERS MEASURED IN EACH POPULATION (n=147 FOR GOLD COATED PARTICLES, 10 NM DATA AS IN CHAPTER 2). THE STANDARD DEVIATIONS ARE 2.82 AND 2.15 RESPECTIVELY. THERE IS A NOTABLE INCREASE IN MEAN DIAMETER FOR PARTICLES COATED WITH HOMOCYSTEINE WHICH MIGHT SUPPORT THE INTRODUCTION OF A GOLD SHELL ON THE SURFACE OF THE IRON OXIDE, HOWEVER THIS SEEMS UNLIKELY FOR THE CITRATE-COATED PARTICLES.

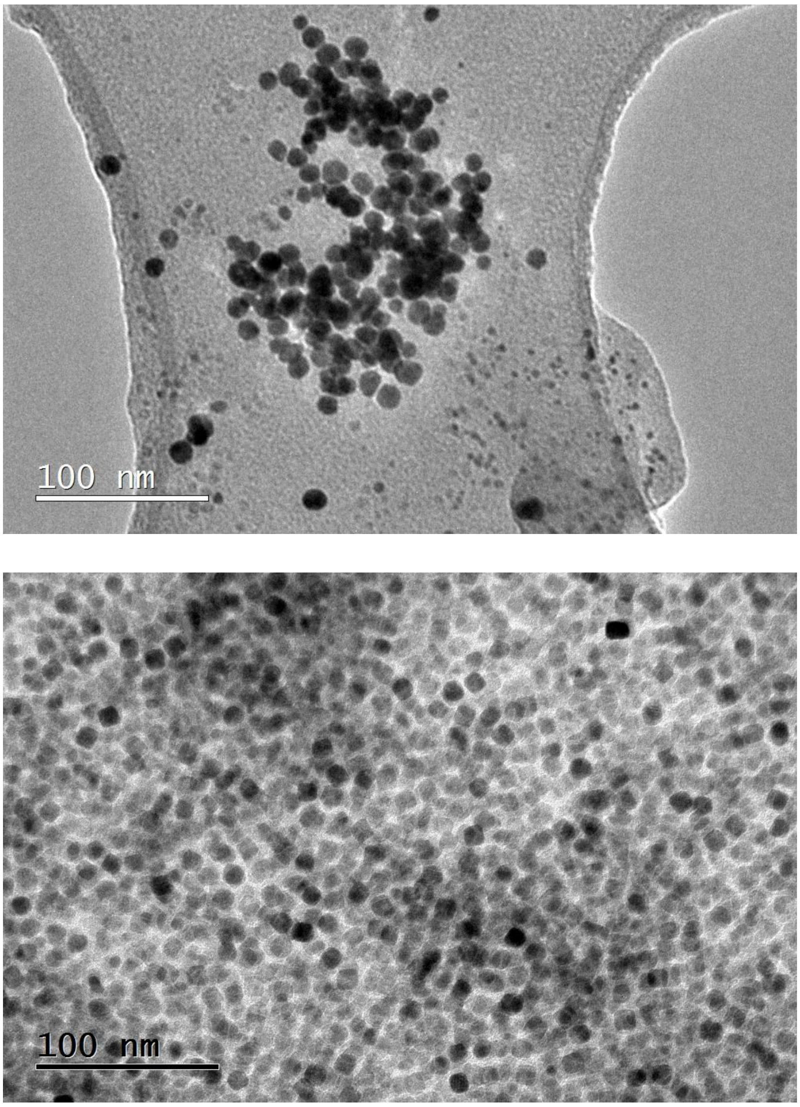

FIGURE 4.10: EXAMPLE OF TEM IMAGE SHOWING GOLD-COATED IRON OXIDE NANOPARTICLES FUNCTIONALISED WITH CITRATE, SHOWING SPHERICAL PARTICLES WITH IRREGULAR FACETING AND NARROW SIZE DISPERSIONS OF POPULATIONS (TOP) AND PARENT IRON OXIDE NANOPARTICLE CORES (BOTTOM).

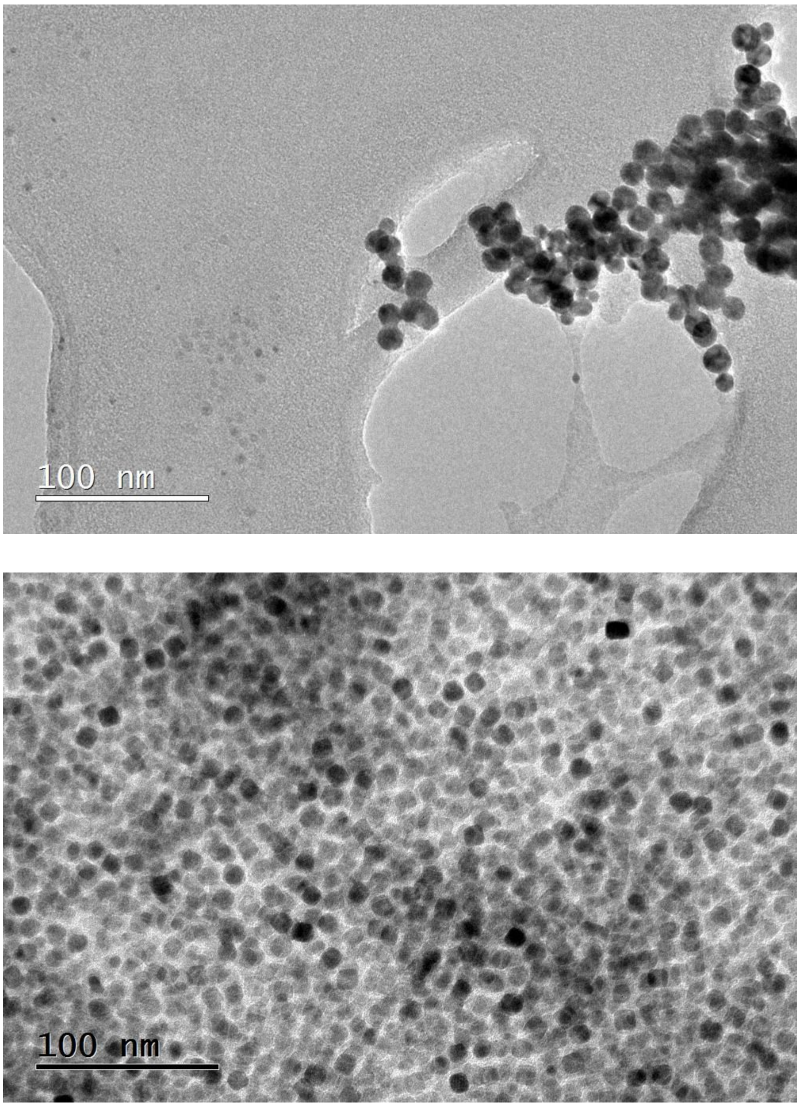

FIGURE 4.11: EXAMPLE OF TEM IMAGE SHOWING GOLD-COATED IRON OXIDE NANOPARTICLES FUNCTIONALISED WITH HOMOCYSTEINE, SHOWING SPHERICAL PARTICLES WITH IRREGULAR FACETING AND NARROW SIZE DISPERSIONS OF POPULATIONS (TOP) AND PARENT IRON OXIDE NANOPARTICLE CORES (BOTTOM).

4.3.2 CHEMICAL REDUCTION

Although some particles are visible in the TEM images of the chemically-reduced nanoparticles, the most prominent feature is the presence of large, flower-shaped aggregates around 50-100 nm in size. These explain the blue colour of the solution as observed during the synthesis, and the formation of the aggregates and subsequent change of the frequency of the plasmon resonance. The ligand exchange had no effect on the colour of the solution, and that is to be expected given the aggregation visible here. These aggregates are more suggestive of the formation of a gold shell around multiple iron cores than the individual particles observed in the thermal reduction.

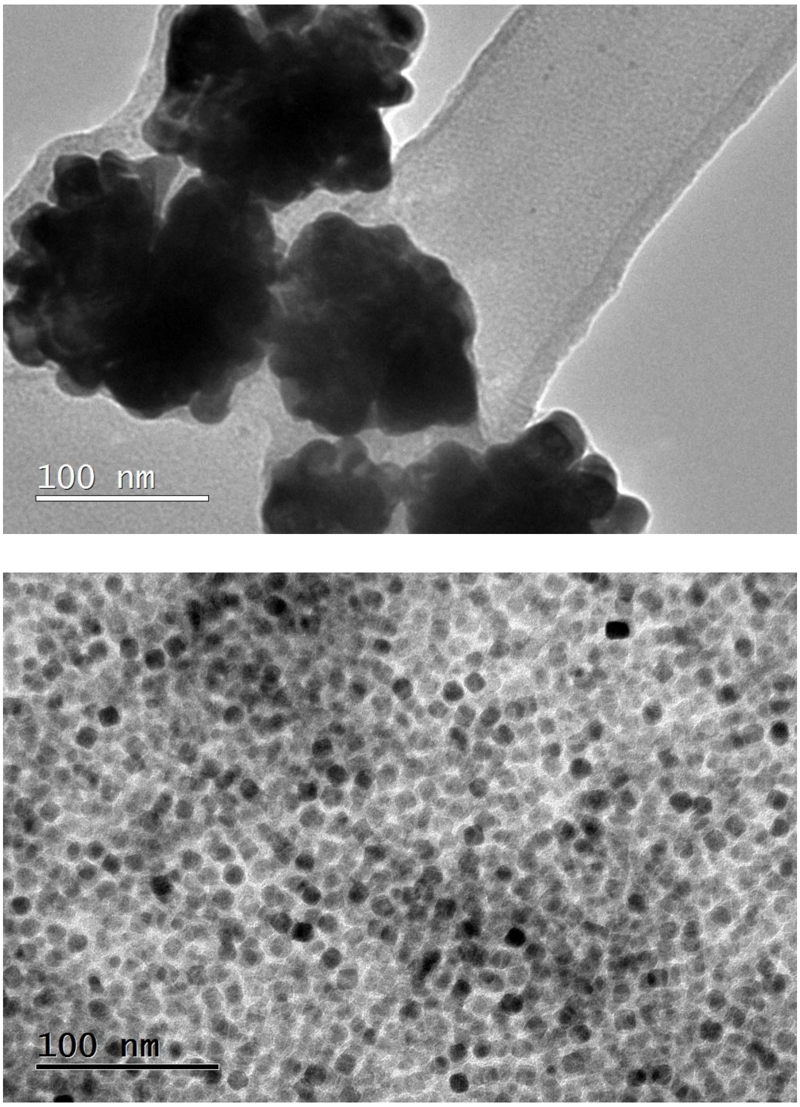

FIGURE 4.12: EXAMPLE OF TEM IMAGE OF CHEMICALLY-REDUCED GOLD-COATED IRON OXIDE FUNCTIONALISED WITH CITRATE, SHOWING LARGE FLOWER-SHAPED AGGREGATES (TOP) AND PARENT IRON OXIDE NANOPARTICLE CORES (BOTTOM).

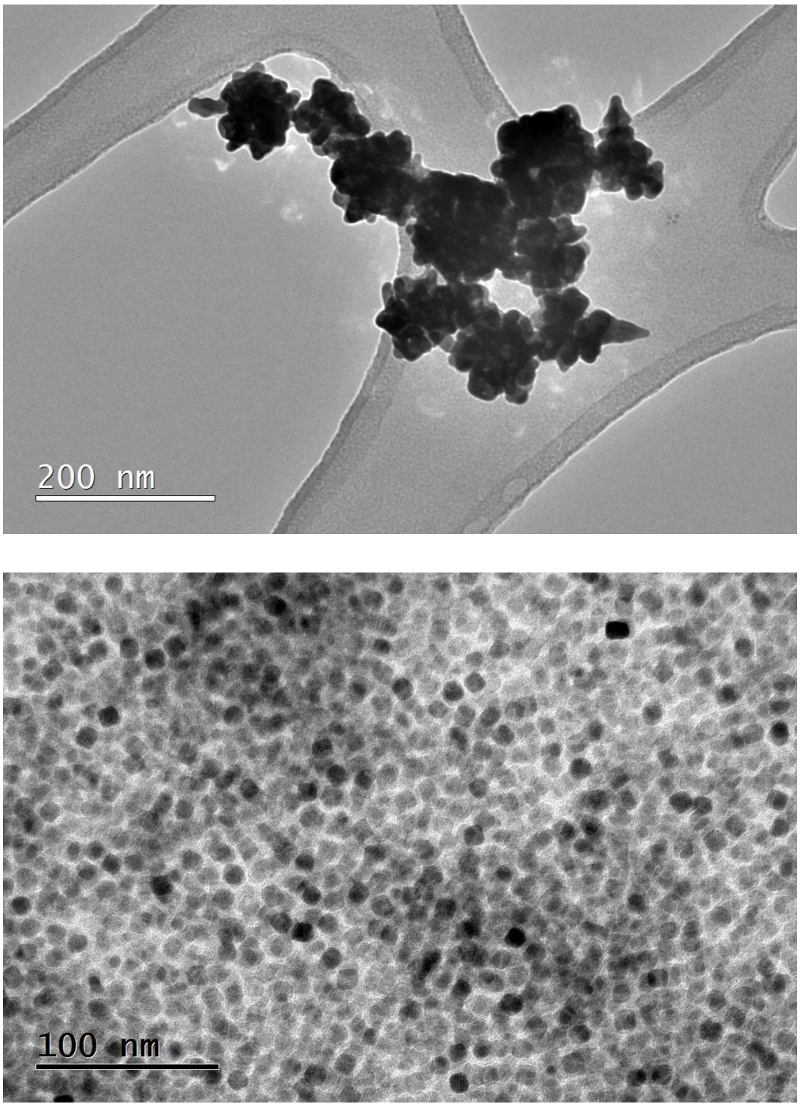

FIGURE 4.13: EXAMPLE OF TEM IMAGE SHOWING THE CHEMICALLY-REDUCED GOLD-COATED IRON OXIDE NANOPARTICLES FUNCTIONALISED WITH HOMOCYSTEINE, SHOWING LARGE, FLOWER-SHAPED AGGREGATES (TOP) AND PARENT IRON OXIDE NANOPARTICLE CORES (BOTTOM).

4.3.3 Hydrophobic Reduction

The hydrophobic nanoparticles subsequently encapsulated with PMAO can be seen in figures 4.14 and 4.15. There is a range of core sizes visible, although they are less well-defined than the previous images of the thermal and chemical routes (figures 4.10-4.13). The range of sizes might suggest that multiple cores have, in some cases, been encapsulated by the polymer. The lack of resolution of the images might also suggest a higher degree of organic contamination, perhaps coming from the polymer, perhaps simply due to the fact that there is a much higher amount of organic ligands in this sample, containing oleylamine, oleic acid, and PMAO. The particles are difficult to measure with any precision compared to other samples, and the low concentration of the suspension recovered after the removal of the aggregates suggests that, although a small number of particles remain stable (as seen here), the synthetic route requires further improvement because of the loss of material.

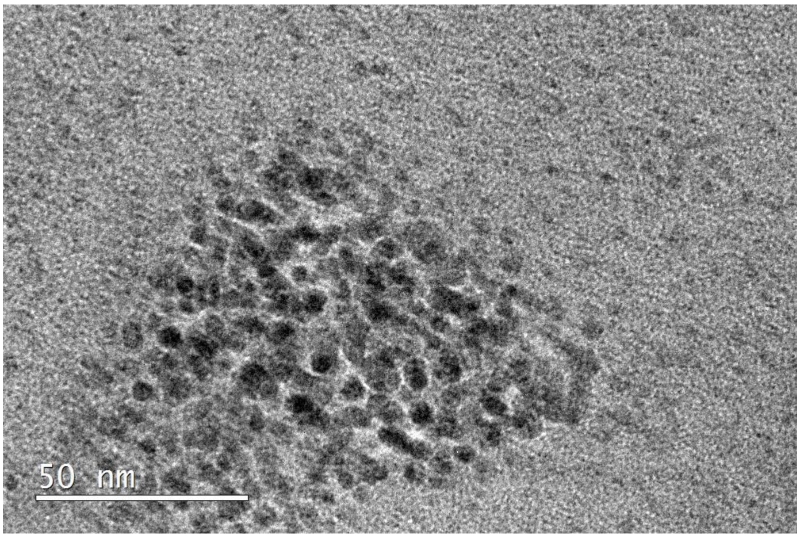

FIGURE 4.14: EXAMPLE OF TEM IMAGE AT 60X MAGNIFICATION SHOWING GOLD-COATED IRON OXIDE NANOPARTICLES RESULTING FROM THE THERMAL REDUCTION OF HYDROGEN TETRACHLOROAURATE IN HYDROPHOBIC CONDITIONS AND SUBSEQUENT ENCAPSULATION WITH PMAO.

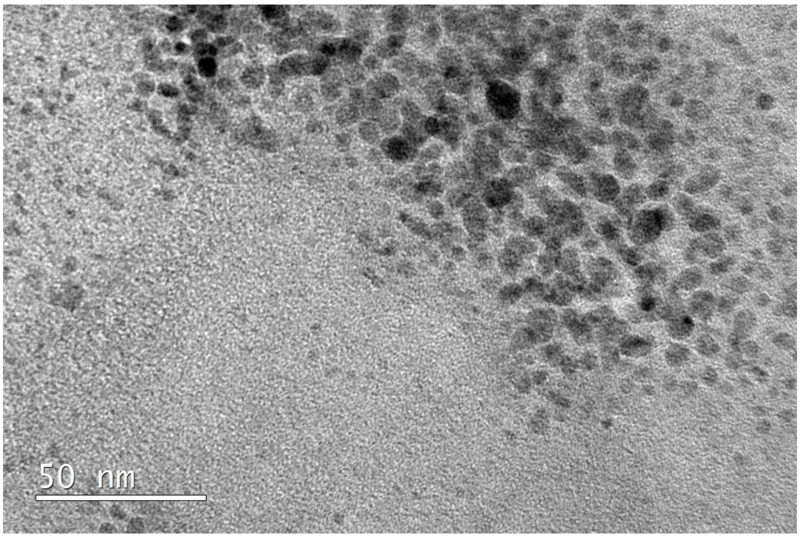

FIGURE 4.15: EXAMPLE OF TEM IMAGE AT 100X MAGNIFICATION SHOWING GOLD-COATED IRON OXIDE NANOPARTICLES RESULTING FROM THE THERMAL REDUCTION OF HYDROGEN TETRACHLOROAURATE IN HYDROPHOBIC CONDITIONS AND SUBSEQUENT ENCAPSULATION WITH PMAO.

4.4 DISCUSSION OF POTENTIAL SURFACE LIGANDS

4.4.1 CITRATE

Citrate is widely documented as a surface ligand for both gold and iron oxide and thus seemed an obvious choice for stabilising the Fe_3O_4@Au particles. Citrate is of particular interest in gold chemistry because of its applications in the Turkevich reaction which is the primary approach for the synthesis of colloidal gold[27]. Gold nanoparticles were first documented in 1857 as synthesised by Faraday, and although gold was long thought to be catalytically inert, the field has become an active frontier of chemical research. Citrate is a versatile ligand for a whole range of materials, including both iron and gold, which has multiple potential binding modes through the carboxylate arms. In the case of citrate on gold nanoparticles, three potential surface binding modes have been identified by Al-Johani et. al. and determined to be dependent upon the surface coverage of the ligand, or the proportion of citrate anions to the gold surface[28].

4.4.2 HOMOCYSTEINE

Given the well-documented affinity of gold surfaces for sulfur-containing groups it would have been remiss to neglect the inclusion of a sulfur-containing ligand for consideration in this library. Homocysteine is an amino acid which is related to cysteine, structurally similar with the introduction of an extra methylene bridge. It is commercially available, although perhaps a modification with the introduction of a longer chain might improve the stability observed in this study, analogous to what was seen with alendronate in chapter 2. Interestingly, homocysteine is also associated with inflammation in the blood vessels and may be a trigger for atherogenesis[29]. Homocysteine was also selected for this study because of the ease with which it could be exchanged for citrate in the synthetic pathway[30].

4.4.3 PMAO

The discussion of hydrophobic gold and gold-iron nanoparticles in the literature opened the door to making a link with the initial promising results of the first phase of contrast agent design and nanoparticle synthesis. There are some methods for the synthesis of gold nanoparticles or Fe_3O_4@Au through thermal decomposition which mimic the initial synthesis[31,32], but in order to be consistent with the other gold-coating attempts it was decided to use 6 nm Fe_3O_4 hydrophobic seeds as synthesised per Sun et. al.[31] in Chapter 2 for reduction and hydrophobic coating. Although the original intention was to experiment with both thermal and chemical reduction approaches for the hydrophobic synthesis, and several papers used oleylamine as a reducing agent for hydrogen tetrachloroaurate, multiple attempts to chemically reduce the gold precursor to metallic gold *in situ* on the surface of the iron oxide proved unsuccessful, and a combination of thermally reducing conditions, oleylamine and oleic acid was required.

4.5 EVALUATION OF DLS DATA

The hydrodynamic sizes as measured by DLS are reasonably consistent with each other, and are similar to the sizes of the SPIONs synthesised in Chapter 2. Both the parent and core@shell data is included on the graphs in figures 4.16-4.20. Similarly to what was observed in TEM, the difference in hydrodynamic size is greater for the core@shell particles coated in homocysteine than with citrate. This is observed with both reduction approaches for the creation of the gold shell (figures 4.16 and 4.17 for the thermal reduction, and 4.18 and 4.19 for the chemical reduction). The decrease observed in diameter between the citrate-coated and homocysteine-coated nanoparticles in both synthetic routes may be due to a change in ligand coverage, a difference in ligand affinity, ligand size or perhaps in binding mode.

Both DLS and visual inspection of the solutions seem to confirm that those nanoparticles synthesised through the thermal reduction route are more stable than those synthesised through chemical reduction. They are also comparatively smaller than the particles synthesised through chemical reduction. The thermally reduced samples show two different colours which support both the gold-coating and the ligand exchange processes, whereas the chemically reduced particles were consistent in colour through the ligand exchange process. The initial synthesis of citrate-coated particles through thermal reduction turned a wine-red colour as indicated in the literature, whereas the chemically reduced solution turned blue, which may suggest a difference in the thickness of the gold layer on the nanoparticle surface or the formation of large aggregates which are visible in the TEM images. Both citrate and homocysteine-coated particles resulting from the chemical reduction route have a tendency to precipitate out of suspension, a behaviour which has not been observed with the comparable thermally reduced suspensions and may also result from the aggregation visible in the TEM images.

An alternative explanation is that the thermal reduction approach resulted in co-mingled populations of gold and iron oxide nanoparticles in suspension, and that the extra reaction time for the homocysteine-coated particles resulted in the formation of larger gold particles which would change the surface plasmon resonance and optical behaviour. The large aggregates observed in the TEM as a result of the chemical reduction are more likely to be gold-coated core@shell systems where gold has encapsulated multiple iron oxide cores, and these resultant large particles would require a higher amount of ligand to suspend them, which might explain the precipitation.

The distinct overlap of populations in figure 4.20 also supports the questions raised by the TEM data for the hydrophobic reduction method, where it is unclear as to whether a shell was deposited on the surface of the iron oxide, or simply a population of gold nanoparticles was formed and co-mingled in suspension with the iron oxide. The weight of evidence is in favour of the co-mingled population, however without further data such as EDX or elemental mapping, it is very difficult to make a definitive statement.

The PMAO-coated particles have not been observed to precipitate, indicating they are reasonably stable, however they are also at a much lower concentration than the citrate or homocysteine-coated particles from either synthetic route, and this may be due to the formation of large aggregates or other synthetic issues with the hydrophobic reduction approach. The hydrophobic gold-coated particles were a similar colour to the citrate-coated thermally reduced suspension, which might suggest the thickness of the gold layer could be similar between the two samples. An alternative is that there are co-mingled populations of gold and iron oxide nanoparticles in the sample.

The relative decrease in hydrodynamic diameter for all samples relative to the parent, seen in table 4.1 is likely due to the relative ligand size – where PMAO encapsulated the parent particle and is likely to have formed a relatively thick layer or polymer shell, both citrate and homocysteine are small single molecules. The PDI measurements for all core@shell samples are lower than those measured in section 2.5 for the iron oxide systems, however interestingly there are again low PDI for the chemically-reduced suspensions which were observed to precipitate. This parallels the PEI-coated particles in section 2.5. The PDI for the hydrophobically-reduced particles is similar to those measured for the thermally-reduced particles, and this also suggests that two populations of co-mingled particles are more likely than a core@shell system in these cases, although there was no evidence of this on the TEM for the hydrophobic system (figure 4.15).

All of the sizes measured would be too large to clear renally, and thus might potentially be sufficiently long-circulating for an antibody-targeted contrast agent.

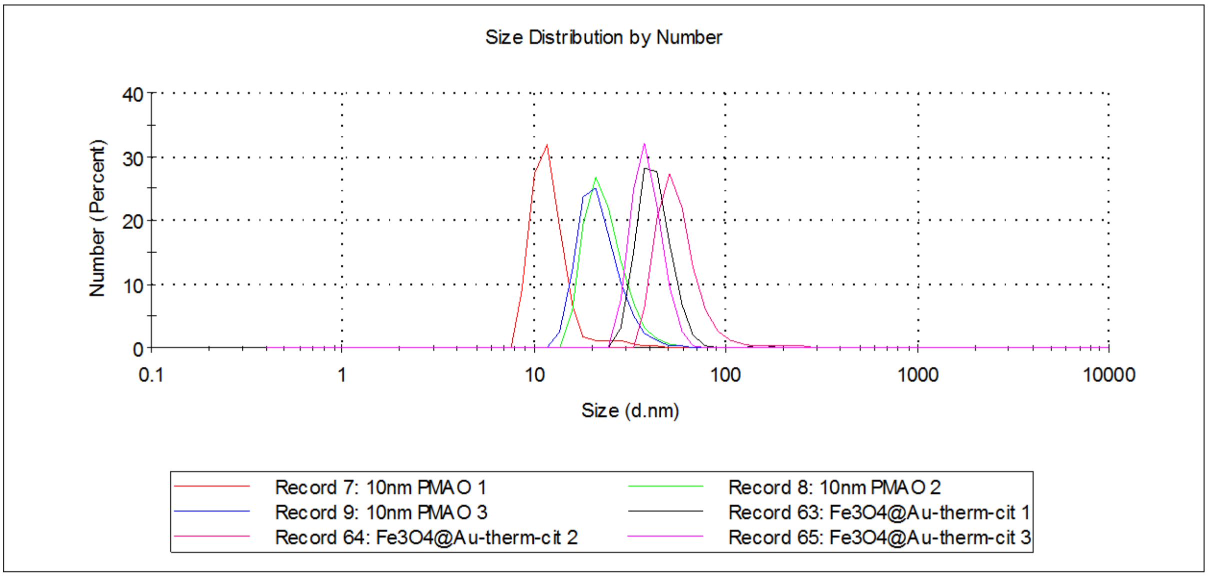

FIGURE 4.16: DLS PLOTS OF SIZE DISTRIBUTION BY NUMBER FOR THERMALLY-REDUCED GOLD-COATED IRON OXIDE NANOPARTICLES FUNCTIONALISED WITH CITRATE AND 10 NM PMAO-COATED PARTICLES, SHOWING THAT THERE IS AN INCREASE IN THE HYDRODYNAMIC SIZE OF THOSE WHICH HAVE BEEN FUNCTIONALISED WITH GOLD.

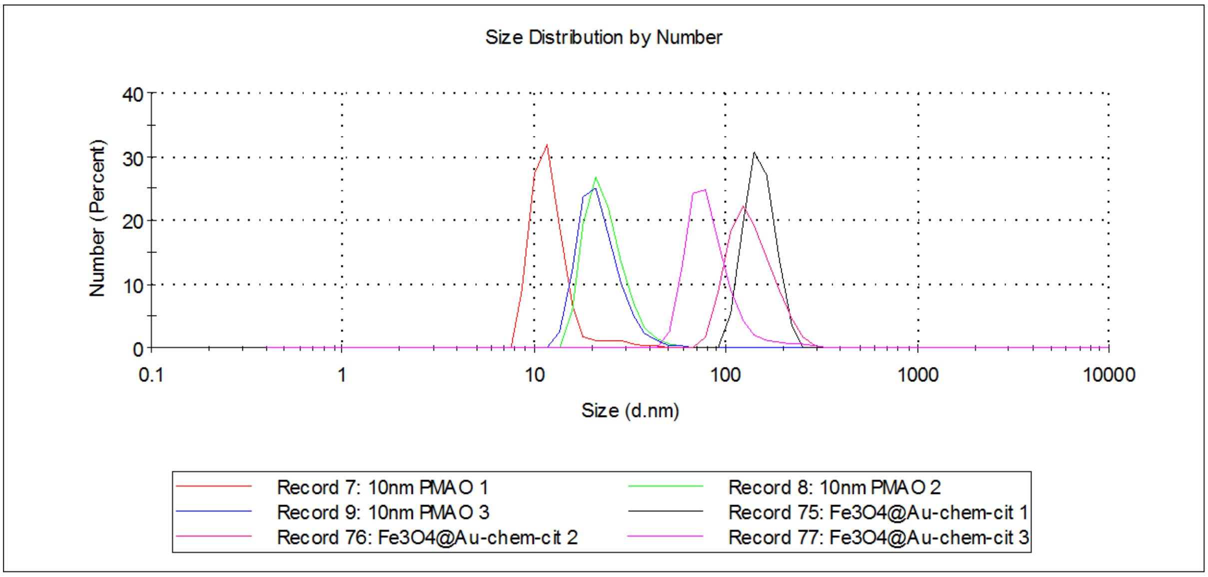

FIGURE 4.17: DLS PLOTS OF SIZE DISTRIBUTION BY NUMBER FOR CHEMICALLY-REDUCED GOLD-COATED IRON OXIDE NANOPARTICLES FUNCTIONALISED WITH CITRATE AND 10 NM PMAO-COATED PARTICLES, SHOWING AN INCREASE IN THE HYDRODYNAMIC SIZE OF THOSE WHICH HAVE BEEN FUNCTIONALISED WITH GOLD.

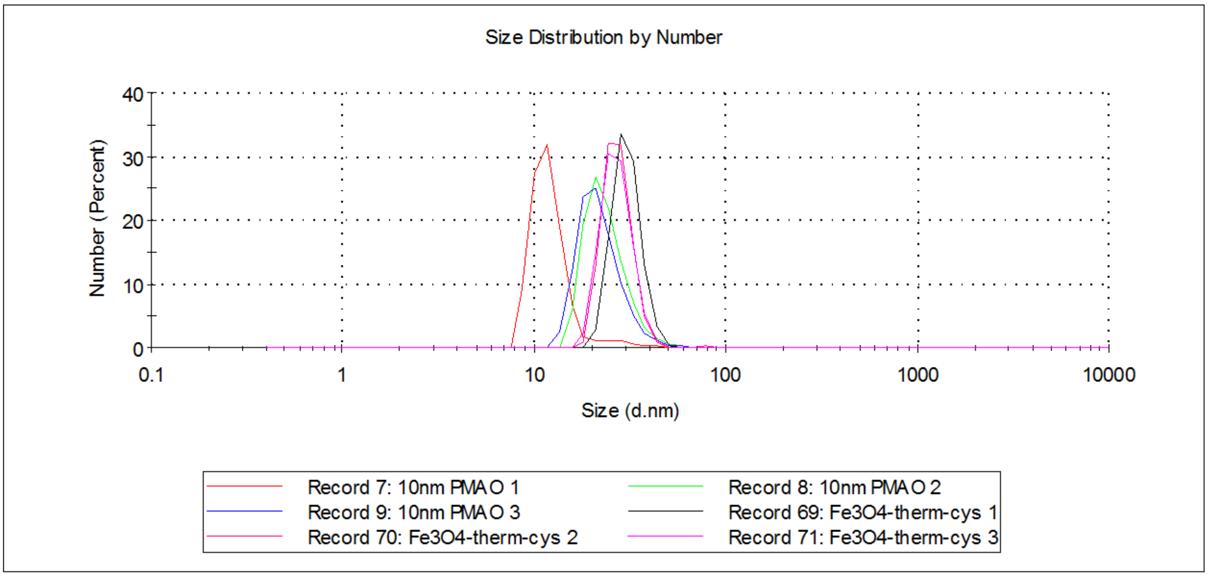

FIGURE 4.18: DLS PLOTS OF SIZE DISTRIBUTION BY NUMBER FOR THERMALLY-REDUCED GOLD-COATED IRON OXIDE NANOPARTICLES FUNCTIONALISED WITH HOMOCYSTEINE AND 10 NM PMAO-COATED PARTICLES, SHOWING MORE OF AN OVERLAP IN SIZES WHICH MAY ARISE FROM LIGAND EFFECTS.

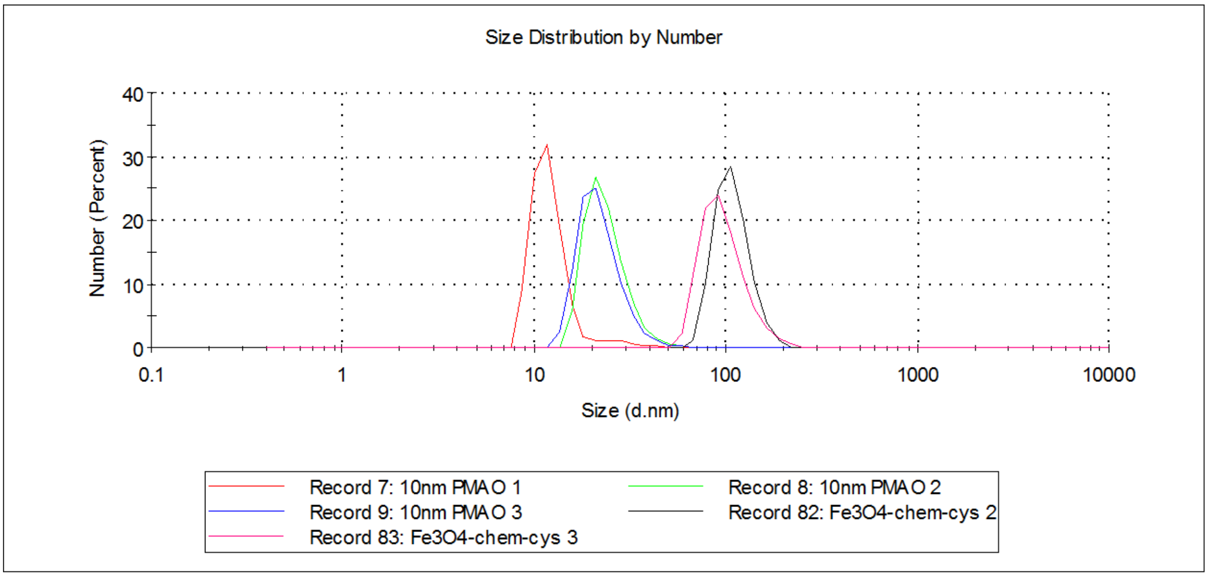

FIGURE 4.19: DLS PLOTS OF SIZE DISTRIBUTION BY NUMBER SHOWING CHEMICALLY-REDUCED GOLD-COATED IRON OXIDE COATED FUNCTIONALISED WITH HOMOCYSTEINE AND 10 NM PMAO-COATED PARTICLES, SHOWING AN INCREASE IN HYDRODYNAMIC SIZE FOR THOSE FUNCTIONALISED WITH GOLD.

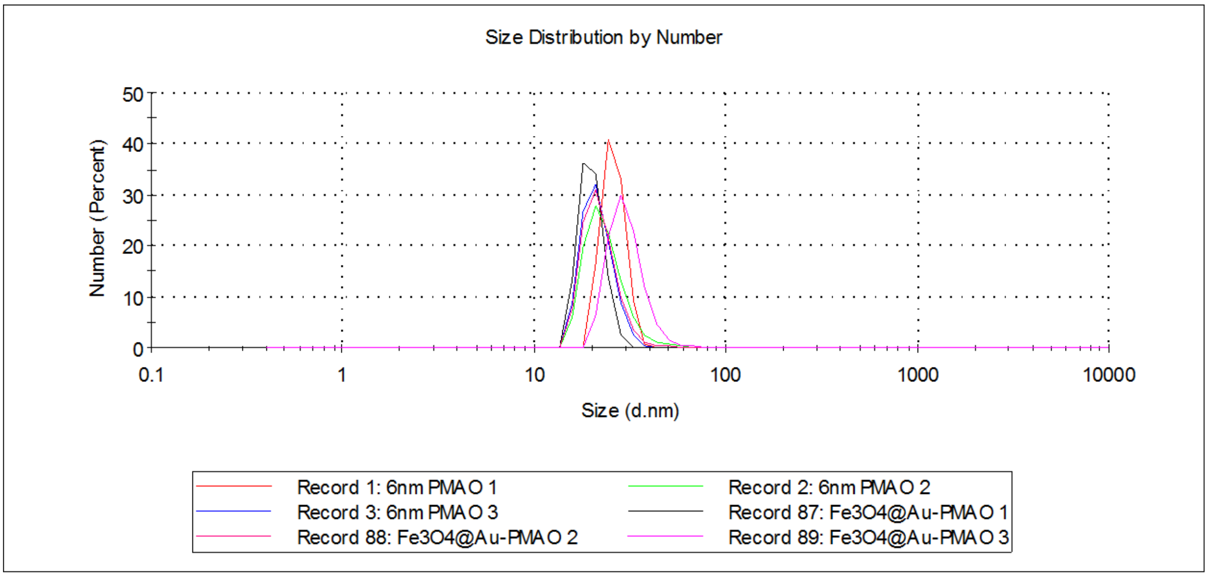

FIGURE 4.20: DLS PLOT OF SIZE DISTRIBUTION BY NUMBER FOR HYDROPHOBICALLY-REDUCED GOLD-COATED IRON OXIDE COATED WITH PMAO AND 10 NM IRON OXIDE NANOPARTICLES ALSO COATED IN PMAO, SHOWING AN OVERLAP IN POPULATION SIZE, WHICH MAY BE RELATED TO THE THICKNESS OF THE ENCAPSULATING LIGAND OR POTENTIALLY DUE TO A LACK OF GOLD ON THE SURFACE OF THE NANOPARTICLES AND INSTEAD THE FORMATION OF TWO CO-MINGLED POPULATIONS OF PARTICLES.

The z-average diameters and standard deviations associated with measurements in triplicate of each sample can be found in table 4.1.

TABLE 4.1: TABLE OF DLS DATA MEASURED ON A MALVERN μV SHOWING Z-AVERAGE AND STANDARD DEVIATION ACROSS THREE MEASUREMENTS.

Sample	Parent diameter (nm)	Parent Standard Deviation	Diameter (nm)	Standard deviation	PDI
Fe3O4@Au-Δ-cit	194.6	4.73	131.6	1.834	0.33
Fe3O4@Au-Δ-cys	194.6	4.73	92.3	1.947	0.27
Fe3O4@Au-chem-cit	194.6	4.73	143.1	3.024	0.16
Fe3O4@Au-chem-cys	194.6	4.73	109.3	2.587	0.17
Fe3O4@Au-PMAO	194.6	4.73	111.3	6.124	0.39

4.6 EVALUATION OF ZETA POTENTIAL DATA

The zeta potential data is an important factor in the potential application of a novel probe. In this context, the project is predicated on the use of antibody-targeting for a vulnerable plaque-specific protein, and antibody-targeting requires long circulation times. There is the advantage in this context that the target protein is in the vascular wall, rather than requiring the antibody targeting moiety or the probe itself to extravasate and slowly accumulate in a target region. Neutral molecules demonstrate the longest circulation times, however negatively-charged surfaces tend to result in longer circulation times than positively-charged probes, and thus in this context a negative charge is advantageous[33].

The measured surface potentials can be seen in table 4.2.

As expected, both novel ligand systems show a negative surface charge which would be advantageous for a long-circulating contrast agent and reduce cellular uptake, as discussed in Chapter 2. The comparatively lower surface potentials of the suspensions synthesised through thermal reduction suggests perhaps better surface ligand coverage than those synthesised through chemical reduction, which may explain the poorer stability observed in those suspensions.

The surface charge measured for the PMAO-coated particles is comparable to that measured for the iron oxide nanoparticles in Chapter 2 (table 2.3), which is encouraging and seems to confirm that the encapsulation approach has been successfully applied in this novel context.

Overall there is very little difference between the measured surface potentials, making it difficult to discriminate between probes to select a potential lead candidate to move forward to antibody coupling and biological verification in this case. When the TEM and DLS data are also taken into consideration, there is a stronger case for the probes synthesised through thermal reduction, however the zeta potential data alone is not sufficient to discriminate between those functionalised with citrate and cysteine. Further work would be needed in order to select a lead candidate from this round of probe development, and the final decision would likely be based on the measured relaxivity values and potential for multi-modal imaging.

TABLE 4.2: TABLE OF ZETA POTENTIAL DATA MEASURED ON A MALVERN μV

Sample	Potential in mV	Standard Dev.
Fe3O4@Au-Δ-cit	-36.0	0.70
Fe3O4@Au-Δ-cys	-34.0	0.55
Fe3O4@Au-chem-cit	-25.0	1.76
Fe3O4@Au-chem-cys	-31.0	0.29
Fe3O4@Au-PMAO	-33.0	0.82

4.8 CONCLUSIONS

In conclusion, this chapter presents an attempted method for the introduction of a gold-shell onto the surface of pre-synthesised hydrophobic iron oxide nanoparticles, through the thermal reduction of hydrogen tetrachloroaurate and subsequent stabilisation by citrate anions. It also presents the development of approaches for the chemical reduction of hydrogen tetrachloroaurate onto the surface of pre-synthesised iron oxide nanoparticles, and the synthesis of hydrophobic gold-coated iron oxide, although both of these approaches may need further optimisation in future.

The resulting nanoparticles are based on previous work undertaken here in chapter 2, and on examples found in the literature, and are designed to further improve upon the probe from chapter 2 by introducing potential multimodality to the imaging, including potential use with OCT as the current gold standard of atherosclerosis imaging to potentially validate the probe's behaviour *in vivo*. The gold shell might also facilitate *ex vivo* confirmation of the probe's location through optical imaging, and if, as documented in the literature, dual-modal T_1/T_2 MRI behaviour is observed, this further increases the utility of the probe and the likelihood of its uptake in clinical settings by enhancing the positive T_1 contrast.

These nanoparticles were characterised through TEM for core size, showing much more disperse nanoparticle cores with both surface ligand systems for thermally-reduced hydrophilic particles, compared to those synthesised through chemical reduction. Fortunately the irregular faceting resulting from the initial iron oxide nanoparticle synthesis by Sun et. al.[26] seemed to be maintained after the introduction of the gold coating, which should result in enhanced T_2 relaxivity in comparison to more perfectly spherical probes. A lack of significant difference in average diameter may suggest the formation of two co-mingled populations of particles, one gold and one iron, however it is difficult to tell with any certainty. Interestingly, the hydrophobic synthetic route which bore most resemblance to the initial iron oxide nanoparticle synthesis did seem to result in comparatively more spherical particles.

DLS data was used to measure hydrodynamic size, and to give an idea of nanoparticle stability in suspension. Narrow size dispersions were measured for all samples, but standard deviations were smallest for the thermally-reduced nanoparticles again. DLS also confirmed that all probes are too big for renal excretion, which is an important consideration in the design of long-circulating probes, such as those designed to be targeted using antibodies, and for some populations showed an increase in hydrodynamic size compared to the parent particles.

The zeta potential data was as expected for all three surface ligands which were used in this study, showing negative surface charges across the board. Long-circulating contrast agents benefit from a neutral or negative surface charge, and therefore any of these surface ligands might be valid to take forward into *in vitro* and potential *in vivo* studies with a targeted probe.

The next steps for this work would be to refine the hydrophobic synthetic method and the chemical reduction route, to take some relaxivity measurements of the probes at different concentrations to evaluate whether the expected enhancement of T_1 is visible, and to take the probes into *in vitro* studies before then replicating the antibody coupling and perhaps moving into an *in vivo* study. There may also be some value in further expanding the library of ligands under consideration, perhaps introducing a co-ligand alongside citrate in the chemical reduction to enhance probe stability[23]. Further analysis using XRD or EDX to confirm the formation of core-shell systems rather than two separate populations of nanoparticles should be a priority, as this is unclear from currently available data.

4.9 EXPERIMENTAL

4.9.1 THERMAL REDUCTION FOR GOLD COATING[3]

An aqueous solution of hydrogen tetrachloroaurate (7.5 ml, 2.0 mg/ml) was added to distilled water (52 ml) and boiled for 20 minutes. 2.5 ml of Fe_3O_4-PMAO nanoparticles were added, followed by sodium citrate trihydrate (2.5 ml, 80 mM). The mixture was boiled for 5 minutes at 500 rpm and allowed to cool. The nanoparticles were isolated by filtration and resuspended in water.

4.9.2 CHEMICAL REDUCTION FOR GOLD COATING[16,21,22]

Method 1: Fe_3O_4-PMAO nanoparticles (2.5 ml) were added to a solution of hydrogen tetrachloroaurate (15 mg/60ml as above) and stirred. A solution of hydroxylamine hydrochloride (2.5 ml, 80 mM) was added and the solution was stirred overnight. The nanoparticles were recovered by filtration and washed.

Fe_3O_4@Au (2.5 ml) prepared as above was added to deionised water (60 ml) and sodium citrate trihydrate (2.5 ml, 80 mM) was also added. The solution was stirred overnight and the nanoparticles recovered through filtration and then resuspended in water.

Method 2: 2.5 mL Fe_3O_4 NPs and 1 mL 0.2 mM $NH_2OH \cdot HCl$ was diluted with 75 mL 0.01M TMAOH, $HAuCl_4$ (7.5 ml, 2.0 mg/ml) was added dropwise into the solution under vigorous stirring and then, 50 mL 15 mM sodium citrate was added incrementally within 2 h. The mixture was stirred overnight after the addition.

4.9.3 COATING WITH HOMOCYSTEINE[3]

Homocysteine (0.125 g) was added to 65 ml of boiling Fe_3O_4@Au-citrate solution and boiled for 5 minutes at 500 rpm before being allowed to cool. The nanoparticles were isolated by filtration and resuspended in water.

4.9.4 COATING WITH HYDROPHOBIC LIGANDS AND PMAO[23–25,34]

Method 1: Hydrogen tetrachloroaurate (0.04 g) was dissolved in chloroform (10 ml) and 1 mmol oleylamine, then added dropwise to a solution of hydrophobic Fe_3O_4 (2 mg, 10 ml chloroform, 2 mmol oleylamine) and stirred for 20 hours. The nanoparticles were precipitated by washing with ethanol and centrifugation, and dried.

Method 2:

6 nm hydrophobic SPIONs (6 mg), hydrogen tetrachloroaurate (83 mg), 1,2-hexadecanediol (0.65 g), oleic acid (0.5 ml), and oleylamine (3 ml) were added to benzyl ether (40 ml) and heated under

nitrogen to 200 ˚C for 1.5 hours. The reaction mixture was cooled, then precipitated with ethanol and centrifugation.

Coating with PMAO:

Poly(maleic anhydride-alt-1-octadecene) (PMAO) (45 mg) was dissolved in $CHCl_3$ (20 ml). The SPIONs (2 mg) were added and mixture was stirred for 30 minutes. Chloroform was removed, and residue re-dissolved in a small amount of $CHCl_3$. NaOH (aq) (0.05 M) was added and mixture was heated at 60 °C until SPIONs transferred to the aqueous phase.

The solution was filtered using on a 0.45 µm filter, and then concentrated by centrifugation with a filter of 30k Mw. Particles were re-suspended in water and stored.

4.10 REFERENCES

1 R. Ghosh Chaudhuri and S. Paria, *Chem. Rev.*, 2012, **112**, 2373–2433.

2 W. Wang, C. Hao, M. Sun, L. Xu, C. Xu and H. Kuang, *Adv. Funct. Mater.*, 2018, **28**, 1–8.

3 T. Ahmad, H. Bae, I. Rhee, Y. Chang, S.-U. Jin and S. Hong, *J. Nanosci. Nanotechnol.*, 2012, **12**, 5132–7.

4 V. Dugandžić, D. Drikermann, O. Ryabchykov, A. Undisz, I. Vilotijević, S. Lorkowski, T. W. Bocklitz, C. Matthäus, K. Weber, D. Cialla-May and J. Popp, *J. Biophotonics*, 2018, **11**, 1–12.

5 S. J. Cho, B. R. Jarrett, A. Y. Louie and S. M. Kauzlarich, *Nanotechnology*, 2006, **17**, 640–644.

6 L.-T.-C. Tran, S. Lesieur and V. Faivre, *Expert Opin. Drug Deliv.*, 2014, **5247**, 1–14.

7 C. L. G. Harman, M. A. Patel, S. Guldin and G. L. Davies, *Curr. Opin. Colloid Interface Sci.*, 2019, **39**, 173–189.

8 Y. Song and S. Chen, *Chem. - An Asian J.*, 2014, **9**, 418–430.

9 M. Lattuada and T. A. Hatton, *Nano Today*, 2011, **6**, 286–308.

10 E. T. K. Demann, P. S. Stein and J. E. Haubenreich, *J. Long. Term. Eff. Med. Implants*, 2005, **15**, 687–698.

11 D. A. Giljohann, D. S. Seferos, W. L. Daniel, M. D. Massich, P. C. Patel and C. A. Mirkin, *Angew. Chemie - Int. Ed.*, 2010, **49**, 3280–3294.

12 S. K. Ghosh and T. Pal, *Chem. Rev.*, 2007, **107**, 4797–4862.

13 S. X., A. K.M.M., L. S. and B. Liu, in *Estrogen Receptors, Methods in Molecular Biology, vol 1366*, ed. K. . Eyster, Humana Press, New York, 2016.

14 L. Dykman and N. Khlebtsov, *Chem. Soc. Rev.*, 2012, **41**, 2256–2282.

15 T. Nann, *Nano Biomed. Eng.*, 2011, **3**, 137–143.

16 Y. Cui, Y. Wang, W. Hui, Z. Zhang, X. Xin and C. Chen, *Biomed. Microdevices*, 2005, **7**, 153–156.

17 A. Y. Solovieva, Y. V. Ioni, A. O. Baskakov, S. S. Starchikov, A. S. Avilov, I. S. Lyubutin and S. P. Gubin, *Russ. J. Inorg. Chem.*, 2017, **62**, 711–714.

18 A. O. Baskakov, A. Y. Solov'eva, Y. V. Ioni, S. S. Starchikov, I. S. Lyubutin, I. I. Khodos, A. S. Avilov and S. P. Gubin, *Appl. Surf. Sci.*, 2017, **422**, 638–644.

19 J. Turkevich, P. C. Stevenson and J. Hillier, *J. Phys. Chem.*, 1953, **57**, 670–673.

20 S. V. Salihov, Y. A. Ivanenkov, S. P. Krechetov, M. S. Veselov, N. V. Sviridenkova, A. G. Savchenko, N. L. Klyachko, Y. I. Golovin, N. V. Chufarova, E. K. Beloglazkina and A. G. Majouga, *J. Magn. Magn. Mater.*, 2015, **394**, 173–178.

21 L. L. Pang, J. S. Li, J. H. Jiang, Y. Le, G. L. Shen and R. Q. Yu, *Sensors Actuators, B Chem.*, 2007, **127**, 311–316.

22 X. Zhao, Y. Cai, T. Wang, Y. Shi and G. Jiang, *Anal. Chem.*, 2008, **80**, 9091–9096.

23 Z. Xu, Y. Hou and S. Sun, *J. Am. Chem. Soc.*, 2007, **129**, 8698–8699.

24 J. Choi, S. Park, Z. Stojanović, H. S. Han, J. Lee, H. K. Seok, D. Uskoković and K. H. Lee, *Langmuir*, 2013, **29**, 15698–15703.

25 F. Delpech, G. Viau, R. Poteau, E. A. Baquero, E. S. A. Nouh and L.-M. Lacroix, *Langmuir*, 2017, **33**, 5456–5463.

26 S. Sun, H. Zeng, D. B. Robinson, S. Raoux, P. M. Rice, S. X. Wang, G. Li, S. X. Wand and G. Li, *J. Am. Chem. Soc.*, 2004, **126**, 273–279.

27 L. Shi, E. Buhler, F. Boué and F. Carn, *J. Colloid Interface Sci.*, 2017, **492**, 191–198.

28 H. Al-Johani, E. Abou-Hamad, A. Jedidi, C. M. Widdifield, J. Viger-Gravel, S. S. Sangaru, D. Gajan, D. H. Anjum, S. Ould-Chikh, M. N. Hedhili, A. Gurinov, M. J. Kelly, M. El Eter, L. Cavallo, L. Emsley and J. M. Basset, *Nat. Chem.*, 2017, **9**, 890–895.

29 S. Guthikonda and W. G. Haynes, *Curr. Atheroscler. Rep.*, 2006, **8**, 100–106.

30 C. K. Lo, D. Xiao and M. M. F. Choi, *J. Mater. Chem.*, 2007, **17**, 2418–2427.

31 S. Sun, H. Zeng, D. B. Robinson, S. Raoux, P. M. Rice, S. X. Wang and G. Li, *J. Am. Chem. Soc.*, 2004, **126**, 273–279.

32 Q. Fan, Wang, C.-J. Zhong, J. Luo, I. S. Suzuki, N. Kim, Y. Lin, M. Suzuki, M. H. Engelhard and J. Q. Wang, *J. Phys. Chem. B*, 2005, **109**, 21593–21601.

33 K. Hola, Z. Markova, G. Zoppellaro, J. Tucek and R. Zboril, *Biotechnol. Adv.*, 2015, **33**, 1162–1176.

34 M. Moros, B. Pelaz, P. López-Larrubia, M. L. García-Martin, V. Grazú and J. M. de la Fuente, *Nanoscale*, 2010, **2**, 1746–1755.

Chapter 5

Conclusions and future work

5.1 GENERAL CONCLUSIONS

Superparamagnetic iron oxide nanoparticles are well-established as potential MRI contrast agents, to the extent that several have been approved by the FDA although they have subsequently been withdrawn from sale for commercial reasons. SPIONs offer several advantages over gadolinium-containing contrast agents for MR, most notably high relaxivities, and the customisability of the platform, as well as their comparatively low toxicity. Iron is an endogenous metal, and thus poses a much lower risk to patients than gadolinium, particularly at the doses required for MRI contrast. This project has examined SPIONs within the more traditional size range, as opposed to the ultra-small range (< 5 nm) which would yield positive contrast agents which might see higher uptake in clinical practice.

In the course of this project, a series of novel SPION-based contrast agents were synthesised through thermal decomposition, underwent phase transfer in a selection of ligand systems, and were characterised with respect to their core size, hydrodynamic size, surface potential, and relaxivity, with some consideration also given to their long-term stability. Where target particles proved challenging to synthesise, attempts were made to optimise reaction conditions (Chapter 2).

On the basis of this work, a lead contrast agent candidate was selected, and an anti-CX3CL1 antibody was coupled to the nanoparticle surface through classical EDC-coupling chemistry and the formation of an amide bond. This agent then underwent tests including the confirmation of antibody coupling through the BCA assay, and an assay to ensure the targeting antibody retained the ability to bind and had not been denatured. The BCA assay confirmed the presence of the antibody in the resuspended nanoparticle preparation but it was not possible to differentiate between chemically bonded antibody and physisorbed protein which might dissociate *in vivo.* Cells were also treated with untargeted SPIONs in order to determine whether or not the novel contrast agent was toxic to a level which might preclude further study, but in a comparison with $FeCl_3$ at high concentrations which would far exceed those encountered *in vivo*, the SPIONs proved to be less toxic than free iron(iii) chloride.

The contrast agent was then taken into preclinical studies in an ApoE-/- mouse model on high fat diet with a cuff placed on the left carotid artery, a modification to a model which is widely understood to be a workhorse of preclinical atherosclerosis studies which allowed the direct comparison of a known stable and a known vulnerable plaque site. The SPION agent was compared with a commercially available gadolinium-based elastin-targeting contrast agent (Gd-ESMA), which provided a baseline for scans and increased the confidence in plaque detection. The novel agent mimicked the behaviour of the commercially available agent, showing comparable areas of void to the areas of enhancement detected by Gd-ESMA, indicating comparable plaque volume detection; however the agent was not specific to vulnerable plaque with no significant difference in uptake above or below the carotid cuff.

The results of the imaging study were confirmed through histology, indicating that both CX3CL1 and CD68 (a macrophage marker) were present in the plaques. Iron deposits were identified in the plaques (confirmed through staining with Prussian Blue) but a lack of co-localisation staining precluded the differentiation between accumulation of the nanoparticles in macrophages, and sites of intra-plaque haemhorrage. (Chapter 3).

Using this initial round of contrast agent design as a foundation, a second round of synthesis was performed towards the development of a multi-modal probe by introducing a gold shell onto the surface of the SPION. This required the investigation of alternative surface ligands, although a route was developed which allowed the application of the lead surface ligand identified in phase 1 in this second round of design. The nanoparticles were once more characterised in terms of core size, hydrodynamic size, and surface potential, with an additional consideration of their long-term stability. Although no EDX was performed allowing the differentiation of core@shell systems from a co-mingled population of gold and iron nanoparticles, comparison of the DLS and TEM data with that of the parent nanoparticles was performed. It was not possible to use this to draw a categorical conclusion, but it did suggest that in some cases a core@shell system could be present, whereas in others it is unlikely or impossible to conclude without EDX or elemental mapping.

5.2 FUTURE WORK

The complex and interdisciplinary nature of this project provides many opportunities for future work which could build upon the foundations presented here. For ease of interpretation, the potential avenues for future work will be divided into chemistry and biology for further discussion.

5.2.1 CHEMISTRY

Although nanoparticle chemistry is well-established, there is a great deal more work which might add value to the foundations presented here. A comparison between different synthetic approaches for the nanoparticle cores, for example between thermal decomposition, co-precipitation, and solvothermal approaches might give a greater degree of control over size dispersion and allow further refinement, in addition to which there are some approaches such as those presented by Park et. al.[1] which allow for the bulk synthesis of nanoparticles which might make this a more appealing approach for potential commercial development (figure 5.1). There would also be the potential to synthesise and compare a wider range of core sizes in order to further elucidate the relationship between core size and relaxivity, allowing for variance in magnetic field strength and temperature.

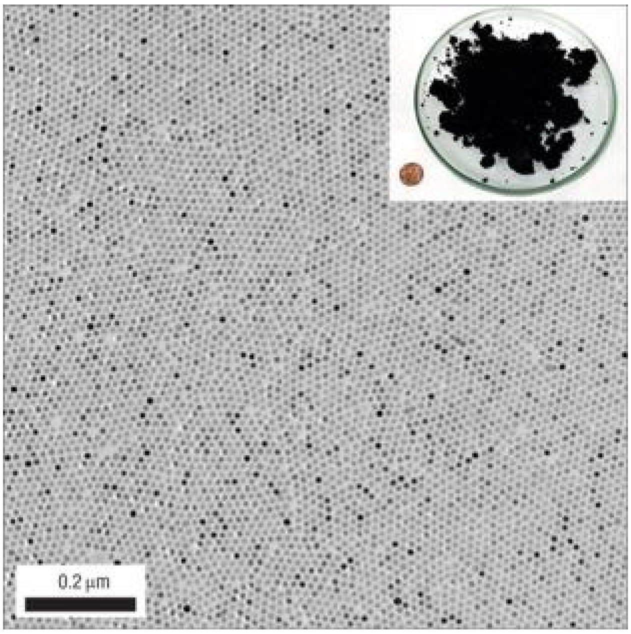

FIGURE 5.1: AN EXAMPLE OF THE LARGE-SCALE BULK SYNTHESIS OF IDENTICAL SPIONS PRESENTED BY PARK ET. AL.[1] INCLUDING A PETRI DISH INSET OF 40 G OF NANOPARTICLES WITH A PENNY FOR SCALE.

Another interesting opportunity for further research might be the introduction of other ions into the crystal structure of the nanoparticles, such as manganese, and the potential development of a dual-modal T_1/T_2 contrast agent, or with a view to further enhancing the magnetic anisotropy and thus the relaxivity of the nanoparticles.

There is an almost inexhaustible range of surface ligands that can be used to render SPIONs compatible with aqueous and biological systems, however due to time constraints only a limited range were examined here. An obvious additional candidate which might further elevate the work is PEG, a ligand which is ubiquitous in nanoparticle and biomedical applications and which would provide a counterpoint to the ligands already examined here. The testing of PEI with co-ligands as presented in the literature might allow for a more effective comparison of its behaviour versus alendronate or PMAO. Some examination of perhaps dopamine as an endogenous ligand, or alendronate/PEG derivatives as synthesised by Sandiford et. al.[2] would also be valuable additions to the range examined here. Dextran, carboxydextran, alginate, and citrate would be valuable to consider, particularly with the use of citrate as a stabiliser for the gold-coated particles in later work, and as some of the more widely documented ligands in literature to further explore the value and potential of PMAO as a relative newcomer to imaging chemistry.

Although the preliminary work on gold-coating presented in chapter 4 was promising, both the chemical reduction approach and the hydrophobic gold-coated particle synthetic routes would benefit from further optimisation. It would also be valuable to compare a range of surface ligands exceeding citrate and homocysteine for the stabilisation of gold, particularly given some discussion in the literature as to whether citrate is capable of solubilising gold without the use of a co-ligand. EDX or other elemental mapping techniques should be used to confirm the presence of core@shell particles as opposed to two co-mingled populations of gold and iron.

To further build on this work and to improve the targeting aspects of the probe for vulnerable plaque, a priority would be the further optimisation of antibody coupling conditions to increase the labelling efficiency, perhaps by varying concentrations, reaction times or conditions, and considering alternative bases such as HATU or HBTU which might improve efficiency compared to EDC (figure 5.2). Further consideration of the expected antibody loading and the possibility of confirming the formation of amide bonds as opposed to other kinds of potentially reversible absorption of the antibody to the polymer would be important.

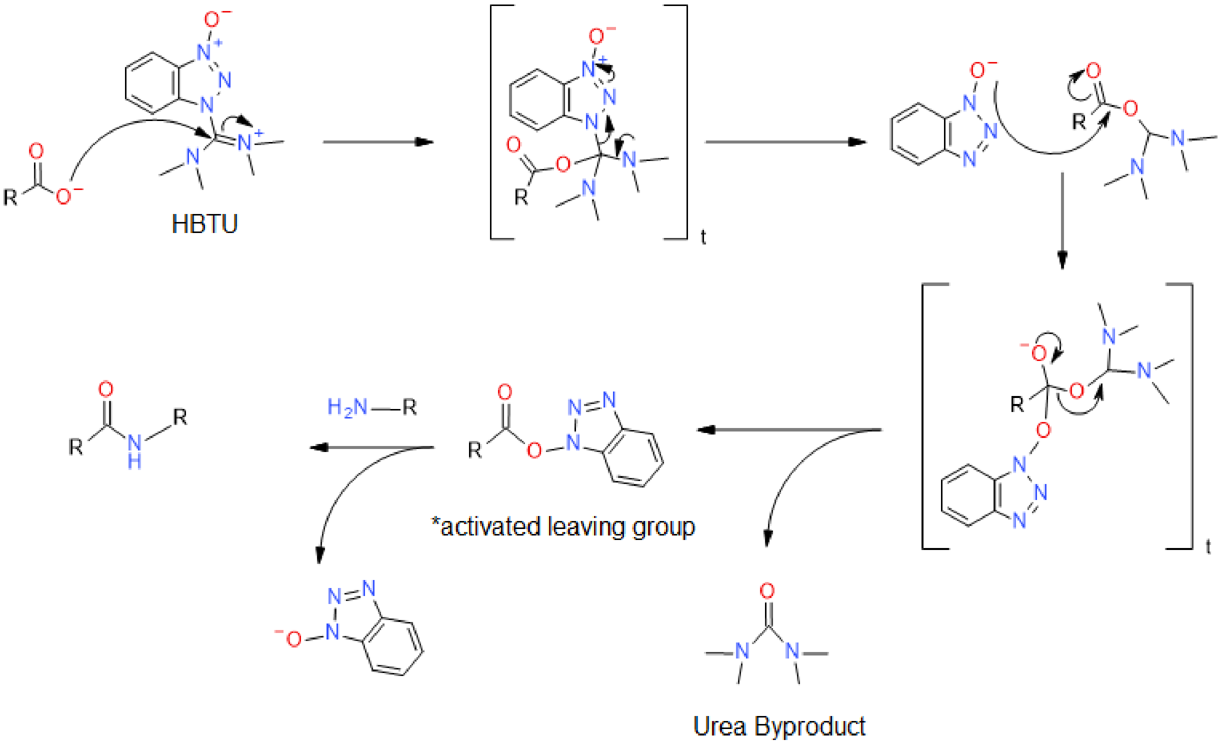

FIGURE 5.2: SCHEME ILLUSTRATING THE MECHANISM OF AMIDE BOND FORMATION WITH HBTU WITH THE FORMATION OF A UREA BYPRODUCT, USED UNDER CC BY-SA 4.0 (WIKIPEDIA, BLANGMACK20)

Coupling a fluorescent probe such as rhodamine to the nanoparticle surface was discussed but was deemed not necessary for the project at this time, however it might be of value in future both for potential multi-modal imaging, and to support *in vitro* and *ex vivo* validation of the probe through facilitating detection in cell assays or in histology. An alternative to EDC chemistry could be thiol-based click chemistry, and an excellent discussion of potential strategies for further functionalisation of the nanoparticle surface can be found by McCarthy et. al.[3].

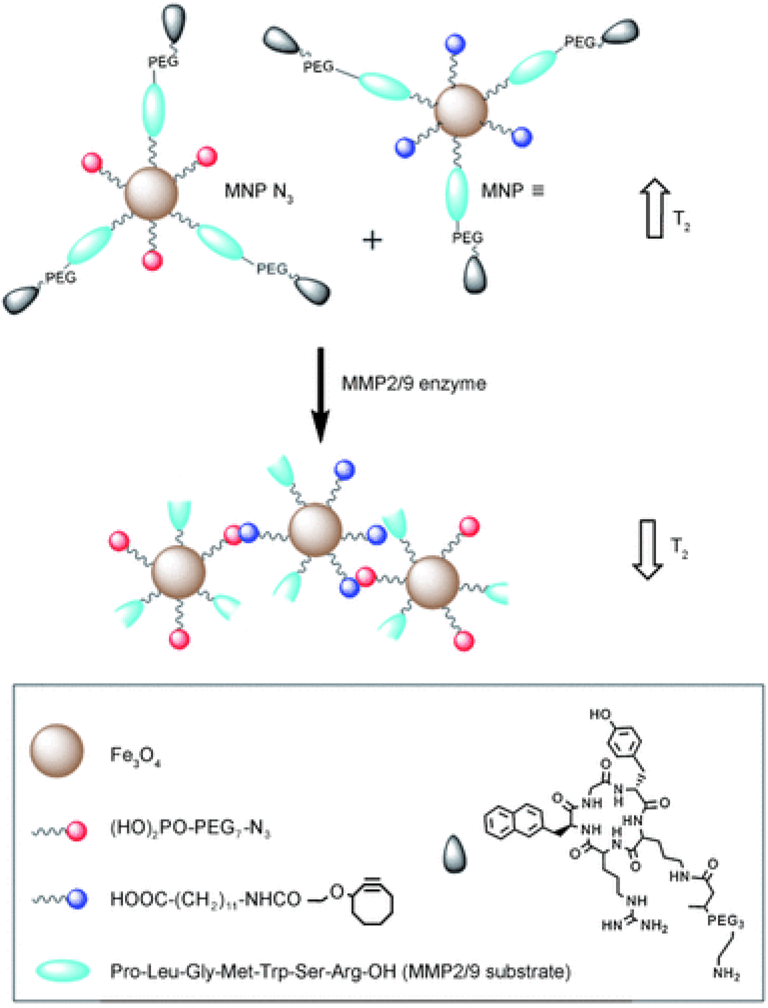

FIGURE 5.3: FIGURE TAKEN FROM GALLO ET. AL.[4] ILLUSTRATING A SMART MMP-SENSING SPION-BASED CONTRAST AGENT, USED UNDER CREATIVE COMMONS LICENCE.

To improve the specificity for vulnerable plaque, a potential refinement to the probe would be the introduction of an MMP-sensitive coating. Matrix metalloproteinases (MMPs) are enzymes which are upregulated in vulnerable plaques, which modify the extra-cellular matrix. Some are responsible for matrix repair, and some are responsible for matrix degradation which increases the risk of plaque rupture. The development of a SPION-based probe where aggregation spontaneously occurs in the presence of upregulated MMPs associated with vulnerable plaque in tandem with the targeting to CX3CL1 might provide valuable secondary confirmation of plaque phenotype and facilitate detection by MRI due to the high change in relaxivity associated with the aggregated probe. The aggregation can be achieved either through bio-orthogonal click chemistry, such as tetrazine-TCO chemistry (figure 5.3), or through the exposure of hydrophobic regions on the nanoparticle surface which then result in spontaneous aggregation[4,5]. Both have been documented in the literature and could be an excellent opportunity to further develop the work presented here.

5.2.2 BIOLOGY

As with the chemistry side of this project, there is no shortage of potential work on the biology which might serve to further support and validate the initial studies contained in this work.

Improved *in vitro* validation with assays of nanoparticle uptake in macrophages, and toxicity assays in more representative cell lines such as primary murine macrophages or even VSMCs would be of great interest in terms of moving the probe towards any potential clinical use. RAW cells are certainly a very common standard cell line in this context, however differentially polarised primary murine macrophages would give more clinically relevant information. It would also be valuable to gauge macrophage uptake, as although the primary purpose of the probe is not to infiltrate the plaque regions through phagocytosis, but rather to evade clearance by the immune system as long as possible, it would give clearer insight into probe behaviour and thus allow further refinement. Although the intention was to synthesise a targeted probe, the results of preclinical imaging and histological studies suggest that the targeting plays less of a role in plaque uptake than macrophages.

The binding study here was designed to confirm that the targeting moiety retained its ability to target CX3CL1 after coupling to the surface of the nanoparticle. Although it was well-designed and successful in that respect, it would benefit from the inclusion of further controls such as wells coated solely with BSA, wells coated with a scrambled chemokine, and wells coated with denatured fractalkine to further confirm the specificity of the antibody for the target molecule *in vivo*.

Due to limited time and resources in the course of this project it was not possible to consider all of the controls we might have desired in the course of the preclinical imaging study, and thus an urgent priority would be a second, larger animal study with multiple control groups and comparable or higher n numbers. In order to test whether the signal observed in the MRI is from the targeting aspect of the probe or simply from non-specific uptake, likely by macrophages, it would be necessary to compare targeted and non-targeted nanoparticles in both diseased and control mice. There is also a question over the representative nature of the model used, and moving into a more traditional atherosclerosis model would be a secondary consideration in a move towards clinical translation of the probe to ensure that it is generalisable and specific to vulnerable plaque as designed. There should also be a consideration of control animals which undergo sham surgeries to allow for any biological consequences which arise from the trauma of the surgery itself rather than from the nature of the model and the disease.

Further preclinical studies would also allow for improved biodistribution and investigation of the clearance of the probe from the bloodstream and the body, given that MR suggests the probe remains in circulation 24 hours post-injection, which is very unusual for a SPION-based contrast agent. The addition of a time course study to identify the optimal time point post-injection for maximal contrast:blood would also be useful. There are several potential approaches which could be useful for this, however some preliminary research was undertaken in the course of this project into using PET for *in vivo* biodistribution, which would also allow for quantification *ex vivo*. The nanoparticles were successfully labelled with zirconium-89, which has a half-life of three days, and were found to be stable in human and murine serum after labelling. It would be possible to get a measure of blood clearance by blood sampling at a range of timepoints – if clearance from the bloodstream is found to be rapid it is quite likely that the probe is becoming trapped in capillaries in the lungs, however if clearance is slower then it is likely to be through the liver. Either way, this could be confirmed through PET imaging, and an additional, smaller animal study, although there might again be value in comparing the biodistribution of targeted and non-targeted SPIONs through this approach, in both diseased and control animals.

After further murine studies, an important step forward towards potential clinical translation of the probe would be moving into a porcine model of atherosclerosis, which is larger and more representative of the disease in humans. It might also facilitate studies with CT and OCT, particularly of the second generation contrast agents with the gold layer, which would be very valuable for comparison to the current gold standard of atherosclerosis imaging and plaque phenotyping. Unfortunately OCT studies are not feasible in murine models of the disease.

5.4 REFERENCES

1 J. Park, K. An, Y. Hwang, J.-G. Park, H.-J. Noh, J.-Y. Kim, J.-H. Park, N.-M. Hwang and T. Hyeon, *Nat. Mater.*, 2004, **3**, 891–895.

2 L. Sandiford, A. Phinikaridou, A. Protti, L. K. Meszaros, X. Cui, Y. Yan, G. Frodsham, P. A. Williamson, N. Gaddum, R. M. Botnar, P. J. Blower, M. A. Green and R. T. M. De Rosales, *ACS Nano*, 2013, **7**, 500–512.

3 S. A. McCarthy, G. L. Davies and Y. K. Gun'ko, *Nat. Protoc.*, 2012, **7**, 1677–1693.

4 J. Gallo, N. Kamaly, I. Lavdas, E. Stevens, Q. De Nguyen, M. Wylezinska-Arridge, E. O. Aboagye and N. J. Long, *Angew. Chemie - Int. Ed.*, 2014, **53**, 9550–9554.

5 S. Matsumura, I. Aoki, T. Saga and K. Shiba, *Mol. Pharm.*, 2011, **8**, 1970–1974.